Imaging for salivary gland sparing radiotherapy

FSC
Mixed Sources
Product group from well-managed
forests, controlled sources and
recycled wood or fibre
Cert no. CU-COC-811465
www.fsc.org
© 1996 Forest Stewardship Council

Imaging for salivary gland sparing radiotherapy

"Beeldvorming voor speekselklier-sparende radiotherapie"

(met een samenvatting in het Nederlands)

Proefschrift

ter verkrijging van de graad van doctor aan de
Universiteit Utrecht
op gezag van de rector magnificus, prof.dr. J.C. Stoof,
ingevolge het besluit van het college voor promoties
in het openbaar te verdedigen
op dinsdag 25 januari 2011 des middags te 2.30 uur

door
Antonetta Christina Houweling
geboren op 27 mei 1983 te Rotterdam

Promotor: Prof. dr. ir. J.J.W. Lagendijk

Co-promotoren: Dr. C.P.J. Raaijmakers
Dr. C.H.J. Terhaard

Speeksel is echt iets wonderlijks, zelfs wonderlijker dan tranen. Bij het spugen is het van de haat, bij het eten is het watertanden van de lust en bij een kus is het van de liefde.

- Meir Shalev -

Contents

Chapter 1

Introduction

1.1 General introduction

Head-and-neck (HN) malignancies are relatively rare. With approximately 2700 newly diagnosed patients each year, they account for 3% of all new diagnosed tumours in the Netherlands. The incidence of HN malignancies is about two-fold higher in men than in women, with the highest incidence at the age of 45-59 in both groups [1].

Together with surgery, radiotherapy is the main treatment for HN malignancies. The HN area is a complex anatomy with target volumes proximate to organs at risk such as the spinal cord and the salivary glands. Besides the primary tumour, lymph node areas are often treated as target volumes, which results in an extended high dose area. As a consequence, the dose to the organs at risk increases and complications can occur more often.

External beam irradiation has evolved from conventional approaches to three-dimensional (3D) conformal techniques. Intensity-modulated radiotherapy (IMRT) is an advanced form of the 3D conformal technique and allows a more concave dose distribution around the target volumes. Hence, the dose to the organs at risk can be reduced more easily [2–4].

Highly radiation-sensitive organs in the HN area are the salivary glands and a major side effect of radiotherapy in the HN area is a reduced saliva production. The reduced salivary flow induces difficulties in swallowing, eating, speaking, and often induces dental caries [5, 6].

This thesis addresses the aspects of the radiotherapy treatment of HN cancer patients and the radiation-induced complications of the largest salivary glands, the parotid and submandibular glands. The research focussed mainly on oropharyngeal cancer patients, which experience the most severe salivary gland complications. Magnetic resonance imaging (MRI) strategies to visualize both the tumour and the radiation effects in the salivary glands are explored. Improvements in the radiotherapy treatment are obtained by adapting the dose distribution to reduce the dose to the salivary glands and by improving the immobilization of the patients during treatment. Furthermore,

the chance of developing a complication given a certain dose to the parotid gland was investigated to further improve clinical decision making.

1.2 Saliva and saliva production

The human salivary glands produce up to 1.5 litre of saliva each day. Saliva has important functions in daily life such as moistening the mouth and protecting it from infections, facilitating speech, and lubrication of food. Saliva is aiding the taste sensation and it is the first step in the digestion of food [7].
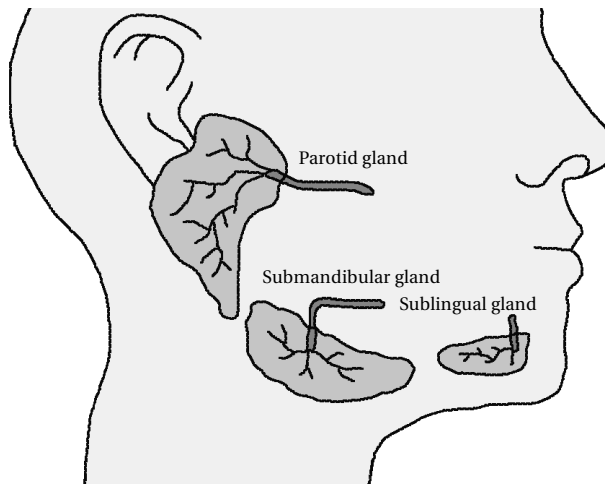
Figure 1.1: Schematic overview of the location of the major salivary glands and the excretory duct of Stenson (parotid gland), the duct of Wharton (submandibular gland), and the duct of Bartholin (sublingual gland).

Over 90% of the total salivary volume is produced by the major salivary glands, the parotid, submandibular, and sublingual glands (Figure 1.1), which are all paired and located bilaterally. The minor salivary glands are distributed throughout the oral cavity and pharynx and account for the remaining 10% of saliva. During stimulation, the parotid glands produce about 60-65% of the salivary volume and the submandibular glands approximately 20-30%. In the resting state, these contributions to the total salivary volume are opposite and the submandibular glands are producing the largest amount of saliva. The saliva produced by all salivary glands consists for more than 99% of water. Additionally, it contains several inorganic ions, lipids, and proteins [5, 7].

The salivary glands typically consist of acinar cells, collecting ducts, myoepithelial cells, fat, and connective tissue. The saliva originates from the acinar cells, flows through the

minor ducts, and is secreted by the larger excretory duct of the gland. The saliva producing acinar cells come in two variants, mucous and serous acinar cells. The parotid glands consist purely of serous acini and their secretion contains mainly water. The submandibular glands consist of both mucous and serous acinar cells, which results in more viscous saliva. The sublingual and minor salivary glands consist predominantly of mucous acini, and hence produce thick secretions [5, 7].

1.3 Xerostomia

The subjective feeling of a dry mouth, xerostomia, is a fairly common clinical complaint. The reduced salivary production can cause inflammations and ulcerations of the oral mucosa, infections of the pharynx, and an increase in dental caries. Various causes of xerostomia have been described such as the side effect of drugs, anxiety, dehydration, vitamin or hormonal deficiencies, Sjögren's syndrome, and irradiation [7]. Unfortunately, adequate artificial saliva substitutes to treat or enlighten chronic xerostomia have not been developed yet and the most effective intervention for xerostomia is its prevention [6].

Figure 1.2: Collection of saliva with a Lashey cup placed over the excretory duct of the parotid gland.

Measuring the grade of xerostomia is not a straight-forward task. Both the subjective feeling of a dry mouth and the objective measured reduction in salivary flow are important. The subjective examination of xerostomia is performed with questionnaires about the quality of life of a patient. Questions about the feeling of a dry mouth and problems encountered during daily life are involved in such questionnaires [8, 9].

The total amount of saliva produced by all salivary glands together can be collected by chewing on a paraffin strip or spitting in a cup [10]. To objectively measure the saliva produced by the parotid glands separately, a cup is placed over the excretory duct (Figure 1.2). The salivary flow is than stimulated by applying a few drops of citric acid on the tongue and saliva is collected for a few minutes. Measuring the saliva production is sensitive to several factors such as the time of the measurement during the day or the time between the measurement and the last gustatory stimulus. In healthy subjects, variations up to 30% are observed [11].

1.3.1 Radiation-induced xerostomia

The underlying mechanism causing radiation-induced xerostomia is still not fully understood [12, 13]. This is partly caused by the non-classical radio-sensitivity of the salivary glands. The functional cells in the salivary cells are highly differentiated and under normal conditions they do not divide. Such cells are thought to be very radiation resistant, which makes the radiation-sensitivity of the salivary glands mysterious [12, 14].

Several hypothesis on the radiation-induced xerostomia mechanisms have been proposed such as stem cell damage [15], damage of the ductal structures [16], and alterations in the blood supply [17]. Most research on the histopathologic mechanism of radiation-induced xerostomia is performed in rats [18] and rhesus monkeys [19]. Cooper *et al.* showed degeneration of serous cells, while the mucous cells showed no changes [5]. Early damage to the plasma membrane, causing distortions in the signal transductions involved in water excretion, was reported in rats by Konings *et al.* [12]. At the long term, classical mitotic cell death of progenitor cells and damage to stem cells was observed, resulting in a lack of replacing the hampered cells. Mitotic cell death is also causing damage to the extracellular environment, which prevents proper cell functioning [12]. However, discrepancies in histopathological observations between rat and rhesus monkey, mainly in the apoptosis reaction, have been described and might be caused by different radiation mechanisms in these animals [12]. Therefore, translating the results of animal studies to human salivary glands is difficult.

The acute and long-term reduction in salivary flow has been reported extensively, as well as the patient-reported xerostomia. Alterations in the composition of human saliva were reported to exist early after radiotherapy [20–22], indicating the salivary glands to be acutely radiation-sensitive with respect to functionality. Mainly differences in protein composition and acidity were reported, but these alterations showed a recovery at the long term [20].

How exactly the damage to the cells and alterations in saliva composition contribute to the complaints of the patients remains unclear. Most research on radiation damage to the salivary glands focussed on the parotid gland. The parotid gland is the largest gland and has the main contribution to total saliva volume under stimulation. However, patient-reported xerostomia does not clearly correlate with the dose to or salivary

output of the parotid glands [9]. These results support the hypothesis that the other salivary glands such as the submandibular glands contribute to the patient-reported xerostomia and research on these glands is required.

1.3.2 Prediction of salivary gland complications

Up to a few months after radiotherapy, the parotid gland function declines even further [23]. The rate of total salivary flow reduction depends largely on the received dose and the irradiated volume of the gland and may become a permanent problem. In general, a parotid gland receiving over 60 Gy on the whole volume will loose its function without a chance of recovery. However, recovery of the parotid flow can occur, most likely in partially irradiated glands receiving a modest dose up to 50 Gy [9].

The chance that a certain treatment plan causes a complication in normal tissue can be investigated using normal tissue complication probability (NTCP) models. Several studies have been performed on modeling the dose-response relationship of the salivary glands using NTCP models [23–28]. The applied dose to the salivary gland, represented by a dose-volume histogram (DVH), is used as the dose input. The reduction in salivary flow rate in each gland separately is often used as a measure of complication and the relation with the applied dose to the gland can be investigated. The salivary output of a gland is often measured as described in section 1.3. The complaints of the patient can also be used as a measure of complication. However, Roesink *et al.* [29] showed a weaker correlation between the mean parotid dose and patient-reported xerostomia than between the mean dose and salivary flow measurements.
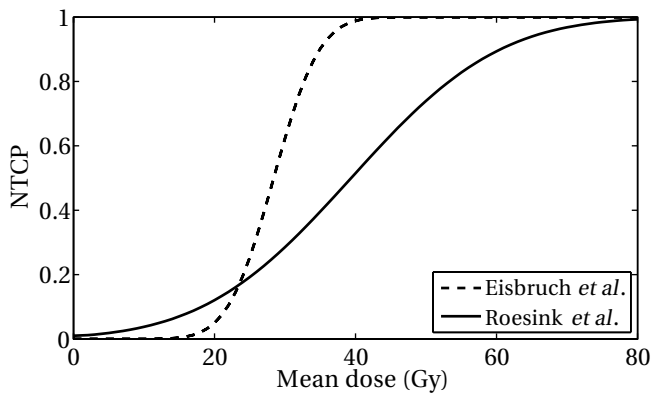

Figure 1.3: The NTCP curves published by Eisbruch *et al.* [24] and Roesink *et al.* [23]

A frequently used NTCP model is the Lyman-Kutcher-Burman model [30, 31]. As for most NTCP models, this model assumes a sigmoid dose-response relationship for a

uniform irradiation of the organ. The model parameters are the steepness of the curve, the dose leading to 50% complications (TD_{50}), and a volume effect parameter. This volume effect parameter is large for parallel organs, resulting in the maximum dose to be of most influence. For serial organs, this parameter is low and the model is acting as a mean dose model if the parameter is fixed to 1.

In the last years, different NTCP curves for the parotid gland have been published. The most interesting discrepancy can be found between the NTCP curves published by Eisbruch *et al.* [24] and by Roesink *et al.* [23] (Figure 1.3). Both studies use the Lyman-Kutcher-Burman model with the volume effect parameter set to 1, a mean dose model. The salivary output was measured during stimulation using cups as described in section 1.3 in both studies. The size of the data sets was comparable, about 90 parotid glands in each study. The reported curve by Eisbruch *et al.* shows a clear threshold at a TD_{50} of 28 Gy. The curve published by Roesink *et al.* has a less steep slope and a TD_{50} of 39 Gy. This means that a mean dose of 39 Gy leads to a complication chance of 50% in the Roesink curve, but to a complication chance of 100% in the Eisbruch curve. Recently, Dijkema *et al.* [32] combined and updated the data of both studies and confirmed the curve published by Roesink *et al.*

From this anecdote we can conclude that an important prerequisite for adequate modeling of the dose-response relationship, or any biological modeling for that matter, is a large enough data set. A larger data set with a good representation of the clinical variation will result in a model that predicts the clinical complications adequately.

1.4   Radiotherapy for head-and-neck cancer patients

As mentioned in section 1.1, external beam irradiation has evolved from conventional approaches with large radiation fields to 3D conformal techniques. In contrary to these radiotherapy techniques, IMRT uses non-uniform beam intensities. The intensity-modulated beams are, at our institute, delivered with a multi-leaf collimator (MLC). An MLC consists of thin blades, which can be individually positioned, and thereby create irregular beam shapes [3, 4]. With IMRT, sharp dose gradients and very homogeneous dose distributions within the target volume can be obtained. Especially in the HN area, where target volumes and organs at risk are located very proximate, IMRT has many advantages. Due to the sharp dose gradients, the dose to the primary tumour can be increased, while at the same time the dose to the salivary glands can be lowered (Figure 1.4) [33].

Another powerful tool to decrease the dose to the salivary glands is reducing the treatment margins. These margins are applied to the clinical target volume (CTV) to correct for uncertainties in delineation and daily patient positioning resulting in the planning target volume (PTV). A decrease of the margin of 1 mm will result in a 1.3 Gy reduction in the mean dose to the parotid gland in oropharyngeal cancer patients [34]. Because
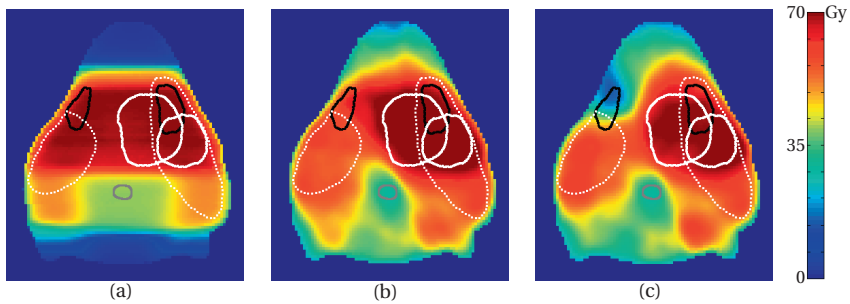
Figure 1.4: The dose distributions of a 3D conformal radiotherapy plan (a), parotid gland sparing IMRT (b), and submandibular gland sparing IMRT (c) in one patient. The white solid lines represent the tumour and a positive lymph node, the white dotted lines are the elective lymph node areas, the grey line is the myelum, and the black lines represent the submandibular glands. The parotid glands are not present in this slice.

the margins do provide tumour coverage despite set-up uncertainties and organ motion, improvements in immobilization and set-up of the patient are required when the margins are reduced.

Figure 1.5: Patient set-up with immobilization mask during treatment.

HN cancer patients are immobilized during daily treatment by a five-point thermoplastic mask (Figure 1.5). This mask prevents large movements of the HN area during treatment. However, some movement is remaining and there is room for improving the immobilization.

7

Cone-beam computed tomography (CBCT) is an in-room imaging technique, which can be used to detect patient set-up errors and even intrafractional errors in 3D. The translational errors can be corrected for using table shifts, and due to recent improvements in equipment, even small rotations can be corrected [35]. CBCT, used during daily treatment in combination with patient immobilization, justifies the decrease of the margins and thereby results in a better salivary gland sparing.

1.5   Imaging of head-and-neck cancer patients

Computed tomography (CT) is the standard imaging technique for HN cancer patients. Next to the use for delineation of target volumes, CT is also used in the dose calculations. Nowadays, positron emission tomography (PET) has become widely available. With PET, information about the metabolism of the tumour can be visualized and it is frequently used in HN cancer patients. However, both modalities lack a clear soft-tissue contrast. Magnetic resonance imaging (MRI), on the other hand, provides a good soft-tissue contrast and is therefore highly suitable for delineation of the tumour [36, 37]. The contrast obtained with MRI is highly depending on the MR technique or sequence used. Therefore, multiple sequences are normally performed in a clinical MR exam.

| (a) | (b) | (c) | (d) |
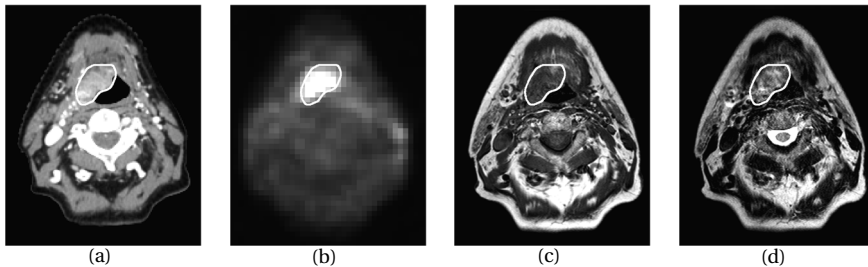
Figure 1.6: A CT (a), PET (b), T_1-weighted MRI (c), and T_2-weighted MRI (d) of one HN cancer patient. The white line is the clinically delineated tumour.

Upcoming techniques in MRI for HN cancer are diffusion weighted imaging (DWI) and dynamic contrast-enhanced (DCE) MRI [38]. Both techniques reveal more information about the physiology of the tissue, so-called functional imaging, and have great potential to guide dose painting. With DWI, the diffusion of water is the basis of the contrast. The diffusion inside a tumour is thought to be restricted due to the increased cell density [36]. In DCE imaging, the perfusion of the tissue is visualized by dynamically imaging the uptake of a contrast agent. Parameters such as blood flow and cell metabolism, which can be altered in HN tumours [36], can be visualized, obtaining additional information about the characteristics of the tumour.

1.5.1 MRI of the salivary glands

Besides imaging of the tumour, imaging of the salivary glands is an issue in HN cancer patients. The good soft-tissue contrast obtained with MRI is making this modality eligible for imaging of the salivary glands. However, different contrasts can be formed by using different sequences or techniques. To define suitable sequences to image the salivary glands, an understanding of the underlying tissue and functionality to be visualized is required. Furthermore, imaging of the radiation-induced changes in the salivary glands might reveal more insight in radiation-induced xerostomia in human. One of the topics of the work presented in this thesis was the set-up of an MRI protocol to image these changes. A short description of the sequences and the rational for these choices are given in this section.

MRI is based on the interaction of protons with an external magnetic field, where the proton in hydrogen is mostly involved in MR imaging. The MRI signal of living tissue is mainly based on the hydrogen spins in water and fat, and the effect of hydrogen spins in other molecules is typically small. The difference in the amount of water and fat is mainly the basis of contrast in MRI. This makes MRI highly suitable for imaging of tissues which contain large amounts of water and fat [39].

Fortunately, the main components of the parotid gland are water and fat [40]. In normal T_1- and T_2-weighted MRI, the signal intensities are based on both water and fat molecules. In general, fat has a bright signal and water is dark in T_1-weighted MRI, while in T_2-weighted MRI this is the other way around. To fully separate the signal coming from water and fat, special techniques should be applied. A multipoint Dixon technique can be used to separate these signals, resulting in a 'water' and 'fat' image [41, 42]. The changes in tissue composition, in water and fat to be more specific, due to irradiation of the salivary glands can be investigated with these sequences.

Damage to the ductal structures of the salivary glands is one of the proposed causes for radiation-induced xerostomia [16, 43, 44]. The ductal structures can be nicely visualized with MR sialography. This is a high-resolution strongly T_2-weighted MRI with additional suppression of the fat signal. Thereby, unbound water molecules such as of the saliva in the ducts have a high signal intensity, while the surrounding tissues have a low signal intensity. Changes in the visibility of the ducts can be detected using this technique [16, 45].

The salivary glands are highly perfused organs [46]. With DCE-MRI or perfusion MRI, the perfusion of tissues can be determined. Therefore, the uptake of an MRI contrast agent is rapidly imaged in time. This uptake can be analysed in a qualitative way or in a quantitative way by applying a model to describe the uptake of the contrast agent. Using a quantitative model, measurements at different time points can be compared and the technique can be used to detect radiation-induced changes in the perfusion of the salivary glands [17].

With these sequences a large range of hypotheses on radiation-induced xerostomia mechanisms have been covered. Other interesting MR techniques for salivary gland imaging are diffusion weighted MRI (DWI) [47] and blood oxygenation level dependent (BOLD) MRI [48]. Due to a limited scanning time, these techniques have not been added to the clinical protocol.

1.6 Outline of this thesis

In this thesis, aspects of all stages in the radiotherapy treatment of HN cancer patients and the adverse affect of the treatment on the salivary output are addressed. The largest salivary glands, the parotid and submandibular glands are the topics of research. The thesis follows the same path as a patient during treatment: from imaging, through radiotherapy planning and the daily treatment, to unfortunately in some cases, radiation-induced xerostomia.

The feasibility of MRI to visualize the perfusion of the tumour was the topic of chapter 2. Dynamic contrast-enhanced (DCE) MRI for tumour imaging is relatively new in the HN field and several challenges have to be encountered. In this chapter, the effect of registration of the tumour area on the quantitative modeling of the DCE-MRI data using a patient-specific arterial input function is addressed. A comparison is made between healthy tissue and the tumour and the added value of perfusion MRI for HN radiotherapy is discussed.

Chapter 3 addresses the use of MRI to improve the delineation of the submandibular gland. From 2009 on, all oropharyngeal cancer patients are treated with submandibular gland sparing IMRT. To be able to adequately spare this small gland, correct delineation is required. Delineation of the submandibular gland with conventional imaging, CT and T_1- and T_2-weighted MRI, was compared to delineation using additional MR sialography images.

Once a patient has undergone all imaging and the target volumes and organs at risk have been delineated, the radiotherapy treatment plan is made. An advanced IMRT technique to spare both the parotid glands and the contralateral submandibular gland is presented in chapter 4. Adaptations in delineation of the salivary glands have been investigated, as well as a reduction in the applied margins. The reduction of the mean dose to the submandibular gland is determined under the clinical dose coverage of the target volumes and under slight underdosage of the contralateral elective lymph node area.

During daily treatment, immobilization of HN cancer patients is of great importance for tumour coverage and salivary gland sparing. Chapter 5 addresses the improvements of a new patient-specific head support in patient immobilization during treatment. The random and systematic displacements from day-to-day as well as during

one treatment fraction were determined for both the standard and the patient-specific head support.

Chapter 6 handles modeling of the chance to develop parotid gland complications given a certain dose distribution. Therefore, six widely used models to describe this relation were compared. To be able to distinguish between the models, data of patients from the University Medical Center Utrecht and the University of Michigan Hospital was combined in the largest published data set until now. The influence of using the physical dose or the biological effect dose was determined. Models were fitted using a maximum likelihood method and ranked using the Akaike's information criterion.

Chapter 7 summarizes the most important results presented in this thesis and gives a general discussion on the radiotherapy treatment of HN cancer patients and radiation-induced xerostomia.

Chapter 2

Dynamic contrast-enhanced MRI at 3.0 T in oropharyngeal cancer patients

Abstract

Purpose: We investigated the feasibility of quantitative dynamic contrast-enhanced (DCE) MRI to visualise perfusion characteristics of the tumour and of healthy tissue in oropharyngeal cancer patients. The susceptibility of DCE-MRI in the tumour due to breathing and swallowing motion was investigated.

Materials and Methods: Eighteen oropharyngeal cancer patients received a DCE-MRI scan, which was incorporated in the standard MR protocol. The patients were scanned in their immobilization mask. All dynamic MR images were registered to the first dynamic image. The MR signal was converted to the concentration of contrast agent and a patient-specific arterial input function was used in the tracer kinetic model fitting. The variations in perfusion parameters due to the registration were analysed and the median perfusion values in the healthy tissue and the gross tumour volume (GTV) were compared.

Results: In these patients, registration resulted in an average translation vector of 0.67 mm. The differences in the median perfusion parameters, due to the registration, were small. A significant increase was observed in the median K^{trans}-, k_{ep}-, and v_p-values in the GTV, compared to the healthy tissue.

Conclusion: Quantitative DCE-MRI was feasible in oropharyngeal cancer patients. The DCE-MRI parameter maps showed heterogeneity and contained additional information about the perfusion characteristics of the tumour.

2.1   Introduction

Dynamic contrast-enhanced (DCE) imaging is widely used to assess the perfusion characteristics of tissues. In cancer imaging, the technique is mainly used for diagnostic and follow-up purposes [36, 49] and investigated for characterisation of tumours [50, 51]. The dynamic images can be analysed in either a qualitative or a quantitative manner. In order to characterize the tumour, a quantitative analysis, such as tracer kinetic analysis, is required. Using a quantitative approach, the values of the perfusion parameters can be compared between patients or be used in treatment-response monitoring [52].

DCE-CT is a widely available imaging technique for head-and-neck (HN) cancer patients at radiotherapy departments [36, 50]. DCE-MRI on the other hand, is rarely used for tumour imaging in the HN region. Recently, both Newbold *et al.* [53] and Jansen *et al.* [51] showed a correlation between MRI perfusion parameters and hypoxia in the tumour and metastatic nodes in HN cancer patients, respectively. Furthermore, Bisdas *et al.* [50] showed a good correlation between perfusion measured with CT and MRI in HN tumours, and correlations between DCE-MRI parameters and PET measures [54]. Kim *et al.* [49] described the value of DCE-MRI in the prediction of response to chemoradiation therapy.

The relation between the measured signal intensity and the concentration of contrast agent is linear in DCE-CT, while in DCE-MRI this relation is non-linear. Additional information such as the pre-contrast longitudinal relaxation time (T_1) per voxel has to be determined in advance. Furthermore, flip angle inhomogeneities complicate the calculation of the concentration of contrast agent [55]. Also, the arterial input function (AIF) faces saturation issues of the signal intensity due to high concentrations of contrast agent in the first-pass peak [56]. Additionally, the inflow of spins with a different magnetization, due to the pulsatile streaming blood, complicates the measurement of the AIF. Due to these difficulties in defining the AIF, a group-averaged AIF is often used in DCE-MRI [53].

Although performing quantitative DCE-MRI is somewhat more complicated, DCE-MRI has advantages over DCE-CT. The most important advantage is that DCE-MRI implies no radiation burden to the patient. This makes the technique well-suited for follow-up imaging and diagnostic purposes. The contrast agent used for DCE-MRI, a gadolinium-based contrast agent, induces less severe allergic reactions compared to the iodine-based contrast agent used for DCE-CT [57].

The gross tumour volume (GTV) in HN cancer patients is often located adjacent to the oral cavity and therefore susceptible to movement due to swallowing and respiration. Movements can be largely reduced by scanning patients in their RT immobilization mask; however, this will not reduce the swallowing or breathing movements.

It is the purpose of this work to investigate whether these challenges can be solved and if quantitative DCE-MRI is feasible in oropharyngeal cancer patients. Furthermore, the

differences in perfusion parameters between the healthy tissue and the GTV will be determined.

2.2 Materials and Methods

2.2.1 Patients

A total of 18 consecutive oropharyngeal cancer patients, referred to our department for primary radiotherapy (RT) treatment, were included in this study. According to the TNM staging system [58], 3 patients had T1 tumour stage, 11 patients had T2 tumour stage, 3 patients were in T3 stage, and 1 patient had a T4 staged tumour. Delineation of the GTV was performed by an experienced radiation oncologist on the conventional CT and T_1- and T_2-weighted MRI scans [37].

This study was part of a study on sparing the salivary glands in oropharyngeal cancer patients and all patients were scheduled for contralateral submandibular gland sparing IMRT [59]. The ethical committee of our hospital approved this study and informed consent was obtained from all patients.

2.2.2 Imaging protocol

All patients received a DCE-MRI scan, which was incorporated in the standard radiotherapy MRI protocol on a 3.0 T MRI scanner (Achieva, Philips Medical Systems, Best, the Netherlands). The conventional T_1- and T_2-weighted MRI scans were acquired before the DCE-MRI. The static gadolinium-enhanced MRI was performed after the DCE-MRI without addition of extra contrast agent. Patients were scanned in their five-point RT immobilization mask to reduce movements and to facilitate registration to other imaging modalities. Two laterally located 140 mm x 170 mm elliptical surface coils (Flex M, Philips Medical Systems, Best, the Netherlands) were used as the receive coils [37].

The DCE-MRI images were acquired using a three-dimensional (3D) spoiled gradient echo sequence (SPGR) with a repetition time (TR) of 4.0 ms, an echo time (TE) of 1.04 ms, and a flip angle (α) of 13°. The sequence parameters TR, TE, and α were optimized to reduce the uncertainty in calculation of the concentration of contrast agent according to Schabel *et al.* [55]. A total of 45 scans, with an extent of 25 cm x 25 cm x 12 cm were acquired every 2.0 seconds, resulting in a total scan duration of 90 seconds. The spatial resolution was 2.2 mm x 2.2 mm x 5 mm. After 2 acquisitions, the contrast agent (Gd-BT-DO3A, Gadovist, Schering AG, Berlin, Germany) was administered (0.1 mmol/kg body weight) with an injection rate of 2 mL per second using a power injector (Spectris Solaris EP, MEDRAD Inc., Warrendale, USA).

2.2.3 Image processing

T_1 calculation

To correctly convert the signal intensity of each voxel in the DCE-MRI to the concentration of the contrast agent, the longitudinal relaxation time (T_1) per voxel was measured for each patient individually before the DCE-MRI scan using the variable flip angle method ($\alpha = 6°$, 16°, and 36°, $TR/TE = 50/1.04$ ms) [39, 60].

Non-linear calculation of the concentration of contrast agent

The signal intensity in an SPGR sequence as a function of the equilibrium magnetization (M_0), flip angle (α), TR, TE, R_1 ($= 1/T_1$) and R_2^* ($= 1/T_2^*$) can be given by:

$$S(\alpha) = M_0 \cdot e^{-TE \cdot R_2^*} \cdot \sin(\alpha) \cdot \frac{1 - e^{-TR \cdot R_1}}{1 - e^{-TR \cdot R_1} \cdot \cos(\alpha)} \tag{2.1}$$

Due to the uptake of contrast agent, the T_1- and T_2-value of tissue shortens. In the fast exchange limit, which is commonly used for analysis of DCE-MRI data, the relaxation rates R_1 and R_2 scale linearly with the concentration of contrast agent (C) and the contrast relaxivities (r_1 and r_2) [39].

$$R_1 = R_{1,0} + r_1 \cdot C \tag{2.2}$$

$$R_2 = R_{2,0} + r_2 \cdot C \tag{2.3}$$

A commonly used simplification in this analysis is the assumption that T_2^* relaxation can be neglected [55]. Substituting Eq. (2.2) into (2.1) will give the non-linear relation of the concentration of the contrast agent at time t (C_t) with the signal at time t (S_t), the signal before contrast agent uptake (S_0), r_1, α, TR, and $E_{1,0}$ ($E_{1,0} = e^{-TR \cdot R_{1,0}}$) [55].

$$C_t = \frac{1}{r_1} \cdot \left[\frac{-1}{TR} \cdot \ln \left[\frac{\left(\frac{S_t - S_0}{S_0}\right) \cdot (E_{1,0} - 1) + E_{1,0} \cdot (1 - \cos(\alpha))}{1 + \cos(\alpha) \cdot \left(\left(\frac{S_t - S_0}{S_0}\right) \cdot (E_{1,0} - 1) - 1\right)} \right] - R_{1,0} \right] \tag{2.4}$$

Eq. 2.4 shows the dependency of the concentration of contrast agent (C_t) to the signal enhancement ($S_t - S_0$), the flip angle α, and $E_{1,0}$. This equation clearly shows the non-linear relation between the concentration of contrast agent and the signal enhancement. Deviations in the flip angle or $T_{1,0}$ will influence the uncertainty of C_t in a non-linear fashion [55]. The value of r_1 for Gadovist at 3.0 T used in this research was 4.5 mM/s [61].

Registration of dynamic images

To determine the influence of GTV motion due to swallowing and respiration during the image acquisition, the DCE-MR images were registered to the first dynamic MR image of each patient. The registration software package Elastix [62] was used to perform a rigid image registration using normalized mutual information. The registration area was defined as the clinical delineated GTV plus a margin of 20 mm in the transversal plane. Each registration resulted in a transformation matrix, consisting of a rotation over the left–right (LR), anterior–posterior (AP), and cranial–caudal (CC) axes, followed by translations in the LR, AP, and CC directions, from which the translation vector could be determined.

2.2.4 Tracer kinetic model fitting

A patient-specific AIF was determined in the internal carotid artery from the concentration images. This AIF was used in the quantitative analysis of both the registered and non-registered DCE data using the generalized kinetic model with a blood plasma component, as described by Tofts *et al.* [63].

$$C_{tissue}(t) = v_p \cdot C_{AIF}(t - \Delta) + K^{trans} \cdot \int_0^{t-\Delta} C_{AIF}(\tau) \cdot e^{\frac{-K^{trans}}{v_e}(t-\tau-\Delta)} d\tau \qquad (2.5)$$

For each voxel, the volume transfer coefficient K^{trans} (min^{-1}), the flux rate constant k_{ep} (min^{-1}; $k_{ep} = K^{trans}/v_e$), the vascular plasma space v_p ($0 \le v_p \le 1$) and the extravascular extra-cellular space v_e ($0 \le v_e \le 1$) per unit volume of tissue were calculated from the concentration of contrast agent in the voxel (C_{tissue}) and in the artery (C_{AIF}). The delay (Δ) between the contrast bolus arrival in the carotid artery and the tissue was determined by fitting the data with a range of delay values and choosing the delay with the best fit. An in-house developed C++ program using the CFSQP package [64] was used to perform the non-linear fit [65].

2.2.5 Patient data analysis

Voxels with a poor fit to the tracer kinetic model, based on a sum of squares value above 0.1 mM per time point, were excluded from the analysis. To evaluate the influence of the registration on tracer kinetic model fitting, the differences between the parameter maps obtained with the Tofts model were analysed by calculating the absolute difference per voxel and by performing a Bland-Altman analysis.

To evaluate the additional information obtained by DCE-MRI inside the GTV, an equivalent part of healthy tissue was delineated at the contralateral side by mirroring the GTV. The difference between the median perfusion values in the healthy tissue and in the GTV in this patient group was tested for significance using a Wilcoxon signed-rank test (SPSS 16.0, SPSS Inc., Chicago, USA).

2.3 Results

2.3.1 Arterial input function

A patient-specific AIF could be determined in all patients and large variations among the patients were observed (Figure 2.1(a)). The height of the peak of the AIF was on average 5.3 mM and varied in this patient group between 2.1 and 10.8 mM. Variations in the bolus arrival time were reduced by fitting the delay (Δ) between the contrast agent bolus arrival in the artery and the tissue as a parameter of the tracer kinetic model. The recirculation peak was visible in almost all AIFs and the temporal resolution was sufficient. Furthermore, the noise on the AIF was very small (Figure 2.1).

The consistency of the AIF within one patient was very good (Figure 2.1(b)). The AIFs measured in the left and right internal carotid artery were similar. Furthermore, inflow artefacts, due to fresh spins in the flowing blood, were not observed in the internal carotid artery. The AIF in a cranial and a more caudal slice (approximately 10 mm apart from each other) corresponded very well (Figure 2.1(b)).

(a)   (b)
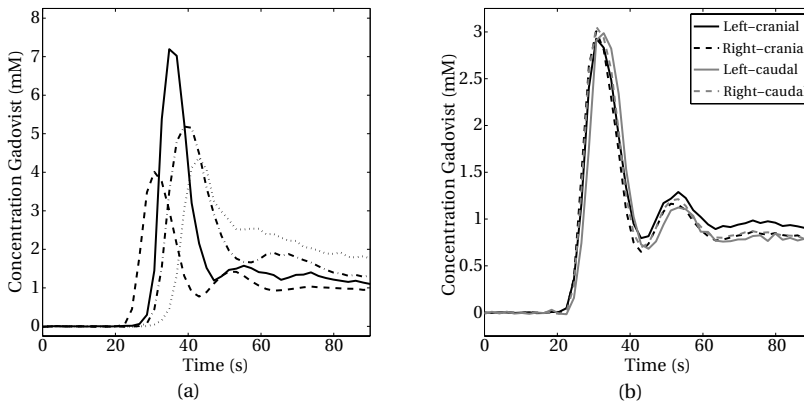
Figure 2.1: Arterial input functions of four patients showing the variation between patients (a). The AIF at different locations within one patient showing the consistency of the AIF (b).

2.3.2 Registration

The mean translation and rotation, averaged over all patients in all three directions, were 0.04 ± 0.48 mm and $0.05 \pm 0.76°$, respectively. The average translation vector was 0.67 ± 0.48 mm, which was within the voxel size of the MR images (Table 2.1).

Table 2.1: The translations, rotations and translation vector of the registrations in the patient group (n = 18).

	Translations (mm)			Rotations (°)			Vector (mm)
	LR	AP	CC	LR	AP	CC	
Mean	0.04	0.11	-0.04	0.17	0.11	-0.11	0.67
Min	-1.29	-1.39	-3.00	-2.91	-2.32	-1.21	0.03
Max	1.19	2.03	1.07	3.38	2.77	1.55	3.43

Abbreviations: M = mean value; LR = left–right; AP = anterior–posterior; CC = cranial–caudal.

2.3.3 Tracer kinetic model fitting

Contrast enhancement curves with low noise levels were obtained in both healthy tissue and the GTV (Figure 2.2).
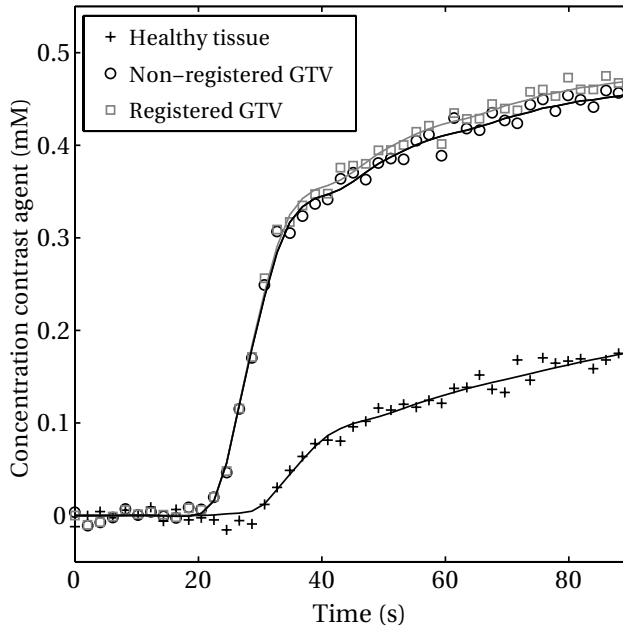
Figure 2.2: Contrast enhancement curves in a healthy tissue voxel, a non-registered GTV voxel and a registered GTV voxel and the accompanying fitted model curves (lines).

Tracer kinetic model fitting on DCE-MRI data in the GTV area was achievable in all patients and perfusion parameter maps could be acquired (Figure 2.3). On average,

about 10% of the voxels within the GTV were excluded from the analysis due to a poor fit to the tracer kinetic model.
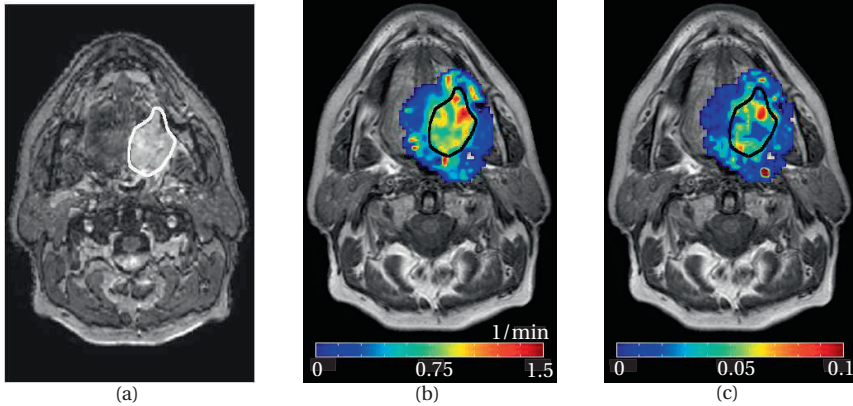
Figure 2.3: One example of a static contrast-enhanced T_1-weighted MRI (a). The K^{trans} (b) and v_p (c) parameter maps in the GTV plus a 2 cm margin are plotted as a colour overlay on an anatomical MRI of a patient. The GTV was delineated (line) on conventional CT and MR imaging.

The perfusion parameter maps showed an increased inhomogeneity inside the GTV compared to the static gadolinium-enhanced MRI (Figure 2.3). In this example, the v_p-map clearly showed an area of low v_p inside the GTV, where the signal in the static gadolinium-enhanced MRI is homogeneous. However, this area is not correlating with an area of high or low K^{trans} values. In general, the v_p values in the GTV were quite high, indicating a high vascular volume in these tumours and resulting in increased signal intensities.

Table 2.2: The average and standard deviation of the median perfusion parameters K^{trans}, k_{ep}, v_e, and v_p in the healthy tissue, non-registered GTV, and registered GTV in the patient group (n = 18).

	K^{trans} (min^{-1})	k_{ep} (min^{-1})	v_e	v_p
	M±SD	M±SD	M±SD	M±SD
Healthy Tissue	0.23±0.12	0.97±0.43	0.28±0.07	0.01±0.01
Non-Registered GTV	0.34±0.19†	1.20±0.51*	0.31±0.07	0.02±0.01*
Registered GTV	0.34±0.19†	1.23±0.51†	0.28±0.06	0.02±0.01*

Abbreviations: M = mean value; SD = standard deviation.

Significant differences between the healthy tissue and GTV are indicated by * ($p < 0.05$) and † (< 0.01).

The absolute difference of the perfusion parameters in the registered and non-registered GTV was calculated per voxel. The median value of the absolute difference per patient, averaged over all patients, resulted in a value of $0.02\,\mathrm{min}^{-1}$ in the K^{trans}-maps, $0.08\,\mathrm{min}^{-1}$ in the k_{ep}-maps, a v_e-ratio of 0.02, and a v_p-ratio of 0.002. The differences between the median perfusion parameters in the registered and non-registered GTV were small compared to their average value (Figure 2.4).
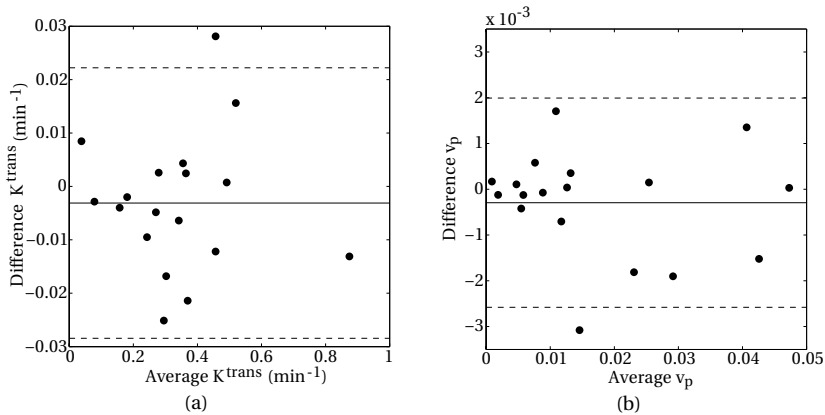
Figure 2.4: Bland-Altman plots of K^{trans} (a) and v_p (b), showing the difference between the median value in the registered and non-registered GTV against their average value. The straight line shows the average difference, the dashed lines show the 95% confidence intervals.

The median values for the perfusion parameters in the GTV were significantly increased compared to the contralateral healthy reference tissue in both the registered and non-registered GTV in the K^{trans}-, k_{ep}-, and v_p-maps (Table 2.2). Furthermore, a large variation within the GTV was observed in the perfusion maps (Figure 2.3).

2.4 Discussion

Tracer kinetic model fitting with the generalized kinetic model was feasible on DCE-MRI data in patients with oropharyngeal cancer. On average, about 10% of the voxels inside the GTV and the healthy tissue were excluded from the analysis due to a poor fit to the tracer kinetic model. A corresponding amount of voxels were excluded in the registered and non-registered GTV.

To reduce motion artefacts during imaging, patients were scanned in their RT immobilization mask and, hence, movement of the body contour was restricted. The remaining movement within the body contour, mainly near air cavities, was most likely due to

respiration and swallowing during imaging. The necessity to reduce these movements by registration of the GTV was investigated. Compared to the voxel size, registration of the GTV to the first dynamic MR image resulted in small translations and rotations. The absolute differences in the parameter maps between the registered and non-registered GTV ranged from 6% in the K^{trans}-maps to 14% in the v_p-maps. These differences were all small in comparison with the average perfusion parameters (Figure 2.4). Overall, the differences were randomly distributed around the GTV, quite small and below the differences observed between the healthy tissue and the GTV.

Because the differences caused by the registration were minor, we could conclude that registration of the GTV in oropharyngeal cancer patients seems not necessary when patient were scanned in their RT mask. Nevertheless, the registration method was fully automated and could be performed rather easily. When patients are not scanned in the immobilization mask, the registration method can probably be used to correct for these displacements and enable quantitative DCE-MRI without scanning in the RT mask. In other HN cancer patients, for example laryngeal cancer patient, the tumour might experience larger movement due to swallowing and breathing. Therefore, registration might be mandatory in these patients.

In all patients, the AIF could be determined in the internal carotid artery, where also the recirculation peak was visible. The variations between the patients indicated the necessity of a patient-specific AIF instead of a group-averaged AIF. The variations in the bolus arrival time were most likely caused by intra-individual variation in blood circulation time. However, these variations were reduced by fitting the delay between the contrast agent bolus arrival in the artery and the tissue as a separate parameter of the tracer kinetic model. The variations in height of the peak were mainly caused by variations in the applied amount of contrast agent, 0.1 mmol/kg body weight and the differences in cardiac output. However, the peak height can also be influenced by specific MR artefacts such as inflow artefacts, and deviations in $T_{1,0}$ determination [66]. Inflow artefacts were no issue in these AIFs (Figure 2.1(b)), due to the sufficiently large cranial-caudal extent of the image slab used in the protocol (12 cm) and the location at which the AIF was determined (cranial side of the slab). Therefore, the magnetisation of the spins in this large slab reached equilibrium and only a negligible number of non-equilibrium spins in the flowing blood end up at the location of the AIF during scanning of one image.

The TR, TE, and flip angle in the DCE imaging protocol were optimized according to Schabel *et al.* [55] to reduce the relative uncertainty in the non-linear calculation of the concentration of contrast agent. The signal-to-noise ratio (SNR) was high in the DCE-MRI scans due to the use of small lateral surface coils adjacent to the region of interest, scanning at a high field strength, and the high perfusion of the tissue. A disadvantage of scanning at 3.0 T is the increased B_1 field inhomogeneity as compared to 1.5 T [67]. As a result, larger flip angle inhomogeneities are present, which could influence the calculation of the $T_{1,0}$ per voxel and thereby the concentration of contrast agent [55]. One

could in principle correct for these inhomogeneities by measuring the B_1 field. However, the B_1 field was not measured in these patients and no patient-specific correction could be applied. A general correction might be possible, but the deviations obtained by such a method have to be evaluated first.

The added value of the perfusion maps of the quantitative DCE-MRI technique lies not in delineation of the tumour, but DCE-MRI reveals additional information about the perfusion characteristics and the heterogeneity within the GTV. Due to these heterogeneous perfusion maps, the technique has high potential to guide dose painting. DCE-MRI has been shown to be eligible for predicting treatment response [49, 68], and for detection of recurrences and mandibula invasion [69]. Because the technique can be used quantitatively, it is suitable for follow-up imaging. However, to correctly interpret the perfusion characteristics of tissue, correlations with pathology should be made.

2.5   Conclusion

This research opens up the possibilities to use quantitative DCE-MRI in oropharyngeal cancer patients. The results indicate that quantitative DCE-MRI at 3.0 T was feasible and image registration was not necessary using the RT mask for immobilization. The perfusion parameter maps obtained additional information about the GTV heterogeneity compared to the static contrast-enhanced MRI. Elevated perfusion was observed in the GTV, compared to healthy tissue. Quantitative DCE-MRI is a promising tool in GTV imaging, characterisation, and dose painting.

Chapter 3

Magnetic resonance imaging at 3.0 T for submandibular gland sparing radiotherapy

Abstract

Purpose: Besides sparing the parotid gland, sparing the submandibular gland is considered to be important in preventing xerostomia in head-and-neck cancer patients. Delineation of the submandibular gland at CT, and even on T_1- and T_2-weighted MR images, is difficult, due to low contrast with the surrounding tissues. MR sialography might be used for delineation.

Materials and Methods: Sixteen oropharyngeal cancer patients received a CT and MRI exam as part of the standard treatment imaging protocol. Patients were scanned in their five-point RT immobilization mask. The MRI exam included T_1- and T_2-weighted MRI scans and an MR sialography scan. Thirty submandibular glands were delineated on only CT, on the combined CT and T_1- and T_2-weighted MRI scans and on all MR images. A Wilcoxon signed-rank test was performed to test if the delineated volumes were significantly different.

Results: The delineated volume of the submandibular gland was 7.3 mL in the CT-delineation, 7.1 mL in the CT/MRI-delineation and 8.1 mL in the MRI-delineation. The MRI-delineation was significantly larger than the other delineations ($p < 0.001$). The differences were mainly located in the cranial direction.

Conclusion: The delineation of the submandibular gland was improved in the cranial direction by using T_1- and T_2-weighted MRI and MR sialography, compared to the other delineations.

3.1   Introduction

A common and severe side effect of radiotherapy (RT) in head-and-neck (HN) cancer patients is radiation-induced salivary dysfunction, xerostomia. In the last few years, intensity-modulated RT (IMRT) has been used increasingly in HN cancer patients to reduce the dose to the parotid glands [70–72]. The reduction of dose to the parotid glands leads to a preservation of parotid flow after RT. Unfortunately, the preserved parotid flow does not directly result in reduced patient-reported xerostomia [9, 73]. The most likely explanation for this discrepancy is that sparing the parotid glands alone is not sufficient and that radiation damage to the submandibular glands plays an important role in the complaints of the patients [9, 73–75].

Sparing the submandibular gland is more challenging than sparing the parotid gland, but recently promising planning and clinical studies have been reported [59, 76, 77]. Saarilahti *et al.* showed that contralateral submandibular gland sparing radiotherapy was safe in terms of loco-regional recurrence and it resulted in a better maintained salivary flow. The main problem in reducing the dose to the submandibular gland is the proximity of the primary tumour target volume, positive lymph nodes, and elective target volumes. Additionally, the submandibular gland has a rather small volume, which makes it more difficult to spare. Partial sparing of the submandibular gland can be achieved at the contralateral side [59, 76] or after surgically transferring the gland out of the radiation field [77].

Prerequisite for reducing the dose to the submandibular gland is an accurate delineation of this small gland. Computed tomography (CT) is currently the standard imaging technique for delineation of the primary tumour and organs at risk, such as the submandibular gland. However, delineation of this gland on CT is difficult, especially in the cranial direction, due to poor contrast with the medial pterygoid muscle [78].

With MRI, superior soft-tissue contrast can be obtained, which facilitates the delineation of soft-tissue organs. Furthermore, MRI becomes more important and a standard technique in delineation of the target volume in HN cancer patients [37, 79–81]. The obtained contrast depends on the type of sequence and, consequently, several types of sequences are generally performed during a clinical MRI exam. As for the CT scan, the T_1- and T_2-weighted MRI scans, which are clinically used for GTV delineation in our institute, normally lack a clear contrast between the submandibular gland and the surrounding tissues in the cranial direction. Because the submandibular gland produces saliva, it contains a large amount of water. Therefore, a type of sequence that visualizes water is most promising for improving the contrast between the submandibular gland and the surrounding tissues.

In MR sialography, the signal is obtained from free water in the tissues. Thus, saliva becomes hyper-intense, showing the ductal structures of the salivary glands; surrounding tissues, such as muscles, have a hypo-intense signal. Furthermore, the salivary glands itself have a higher signal intensity than the surrounding tissues, showing also the out-

line of the glands. MR sialography is currently used to diagnose several diseases as Sjögren's syndrome or sialolithiasis [82, 83] and to visualize radiation-induced xerostomia [16, 43].

In this study, we investigated the benefit of using MRI, and MR sialography in particular, for the delineation of the submandibular gland.

3.2   Materials and Methods

3.2.1 Patients

A total of 16 oropharyngeal cancer patients, referred to our department for radiotherapy treatment, with no previously reported disorders of the salivary glands, were included in this study. Two patients received a unilateral neck dissection in which one submandibular gland was removed, resulting in 30 submandibular glands available for analysis. All patients received a planning-CT scan and an MRI exam as part of the standard treatment imaging protocol for delineation of the primary tumour and organs at risk. In both the CT and MRI exam, patients were scanned in their five-point RT immobilization mask to reduce movement artefacts. MR sialography was added to the MRI protocol, which lengthened the MRI exam by 3:36 minutes.

This research was part of a broader study on sparing the submandibular gland in oropharyngeal cancer patients and all patients were scheduled for contralateral submandibular gland sparing IMRT [59]. Therefore, if possible, patients had one spared submandibular gland, which was planned with a mean dose constraint of less than 40 Gy [59, 75]. The ethical committee of our hospital approved this study and informed consent was obtained from all included patients.

3.2.2 Imaging

CT imaging

The planning-CT scans were acquired on either the Aura CT system (6 patients) or the Brilliance CT Big Bore system (10 patients) (Philips Medical Systems, Best, The Netherlands) using an intravenous contrast agent (Ultravist, Schering AG, Berlin, Germany). The CT scans were acquired with 120-140 kVp / 120-150 mA, a slice thickness of 2 mm, an in-plane voxel size of 1 mm x 1 mm and a matrix of 512 x 512. The image quality of all CT scans obtained from both systems was comparable, at least in the submandibular gland region.

MR imaging

The MR images were acquired on a 3.0 T MRI scanner (Achieva, Philips Medical Systems, Best, The Netherlands), using laterally located 140 mm x 170 mm elliptical sur-

face coils (Flex M) as the receive coils. Patients received the clinical T_1- and T_2-weighted MRI scans and the MR sialography scan in one session.

The transverse T_1-weighted MRI was a spin-echo (SE), multi-slice (MS) sequence (repetition time/echo time/number of signals averaged [TR/TE/NSA] = 697 ms/15 ms/2) with a field-of-view (FOV) of 250 mm x 190 mm, an in-plane voxel size of 0.5 mm x 0.5 mm, 26 slices of 4 mm thickness and a slice gap of 0.4 mm. The scan time was 5:44 minutes.

The transverse T_2-weighted MRI was a MS, multi-shot, turbo spin-echo (TSE) sequence (TR/TE/NSA = 4200 ms/130 ms/2) with a TSE factor of 15, a FOV of 250 mm x 190 mm, an in-plane voxel size of 0.5 mm x 0.5 mm, 28 slices of 4 mm thickness and a slice gap of 0.4 mm. The scan time was 4:45 minutes.

In both scans, sensitivity encoding (SENSE) with a factor of 2 in the right-left direction was used to reduce the acquisition time and spatial receive inhomogeneities were corrected using constant level appearance (CLEAR).

MR sialography was performed using two separate sagittal packages, containing the parotid and submandibular gland at each lateral side. A MS, multi-shot, TSE sequence (TR/TE/NSA = 6000 ms/190 ms/1) with fat suppression using spectral pre-saturation with inversion recovery (SPIR), a TSE factor of 20, a FOV of 100 mm x 100 mm, an in-plane voxel size of 0.39 mm x 0.39 mm, 14 slices of 4 mm thickness and a slice gap of 0.4 mm was used. The scan time was 1:48 minutes per package; spatial receive inhomogeneities were corrected using CLEAR.

Image registration

The CT and MR images were registered using a three-dimensional rigid registration method based on normalized mutual information [62]. The quality of the registration was verified qualitatively by visual inspection of the body contour and the outline of the salivary glands.

3.2.3 Delineation of the submandibular gland

In total, three different delineations of the submandibular glands were obtained. First, the submandibular glands were delineated for treatment planning purposes on a combination of CT and T_1- and T_2-weighted MRI scans by the radiation oncologist (the CT/MRI-delineations). Next, the submandibular glands were delineated by an independent radiation oncologist to obtain the other delineations for this study. These delineations were performed on the CT scan only (the CT-delineations) and on a combination of the T_1- and T_2-weighted MRI scans and the MR sialography images (the MRI-delineations). All radiation oncologists were experienced in delineating the HN area.

3.2.4 Data analysis

The delineated volume of the submandibular gland, based on the CT-, CT/MRI-, and MRI-delineations were calculated. Furthermore, the lower and upper borders of the submandibular gland were defined, from which the length of the cranial-caudal axis of the gland was determined for all delineations.

To evaluate the influence of the delineated volume on the clinically planned dose to the submandibular gland, the mean dose to the gland was determined for all delineations. Additionally, the volume (mL) of the submandibular gland that received more than 40 Gy (V_{40}) was calculated. This threshold of 40 Gy was reported by Murdoch-Kinch *et al.* as the dose resulting in 50% submandibular gland complications [75] and was the dose-planning criterion in the contralateral submandibular gland sparing IMRT [59].

The volume, cranial-caudal extent, mean dose, and V_{40} were tested for a statistical difference between the delineations using a Wilcoxon signed-rank test. The tests were performed using SPSS, version 16.0 (SPSS Inc., Chicago, USA).

3.3 Results

The MR sialography images showed the ductal structures of the submandibular glands as a hyper-intense branch. The body of the gland was visual as a medium-intense area in a hypo-intense background. The outline of the submandibular gland, including the cranial border, could be visualized using MR sialography (Figure 3.1).

| (a) | (b) |
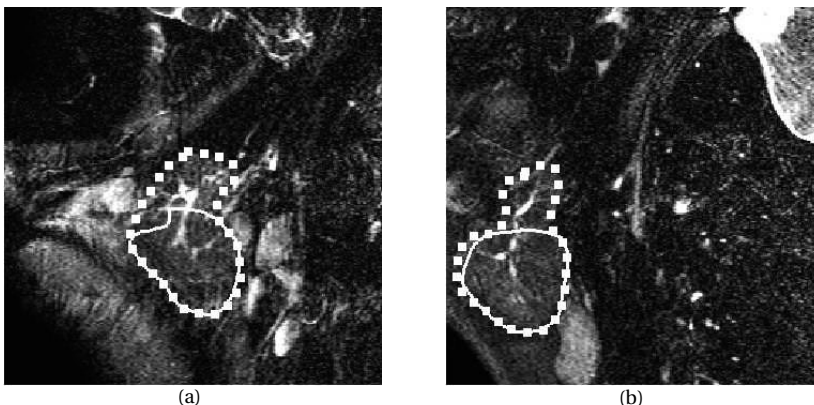
Figure 3.1: Sagittal MR sialography images of two patients with the clinical CT/MRI-delineation (solid line) and the MRI-delineation (dotted line).

An improved soft-tissue contrast was obtained with the T_1- and T_2-weighted MRI and MRI appeared to be better than CT for delineation of the submandibular gland. However, in the CT and T_1- and T_2-weighted MRI scans, the contrast between the submandibular gland and the surrounding tissues in the cranial part of the gland was lower than in the caudal part, and the MRI scans were not superior to the CT scan (Figure 3.2).

(a) (b) (c)
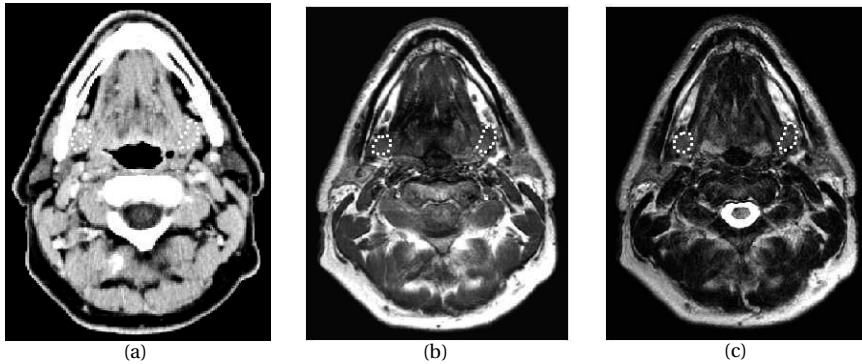
Figure 3.2: The transverse CT (a), T_1-weighted MRI (b), and T_2-weighted MRI (c) scans of one patient with the submandibular glands delineated in a cranial part.

The difference in slice orientation, sagittal for the MR sialography images and transverse for the other images, was not the cause of the improved contrast. It was observed that a sagittal orientation of the other images did not show a clear contrast as obtained with MR sialography.

The delineated volume of the submandibular gland was 7.3 ± 2.4 mL (mean $\pm$ 1 SD) on average in the CT-delineations. The delineated volume in the CT/MRI-delineations was 7.1 ± 2.2 mL on average and was not significantly different from the CT-delineations ($p = 0.5$). The delineated volume of the MRI-delineations, based on T_1- and T_2-weighted MRI and MR sialography, was 8.1 ± 2.3 mL on average and significantly larger than the CT- and the CT/MRI-delineations ($p = 0.001$ and $p < 0.001$, respectively) (Figure 3.3).

The larger delineated volume in the MRI-delineations was primarily caused by an improved contrast in the cranial direction. The length of the cranial-caudal axis, averaged over all glands, was 29.8 ± 6.9 mm in the CT-delineations and 28.8 ± 6.1 mm on average in the CT/MRI-delineations ($p = 0.4$). This length was 38.4 ± 6.8 mm on average in the MRI-delineations, which was a significant increase as compared to the CT- and the CT/MRI-delineations ($p < 0.001$) (Figure 3.4). The increased cranial-caudal extent of the submandibular gland could be explained by an improved contrast at the cranial border of the gland in the MR sialography images.
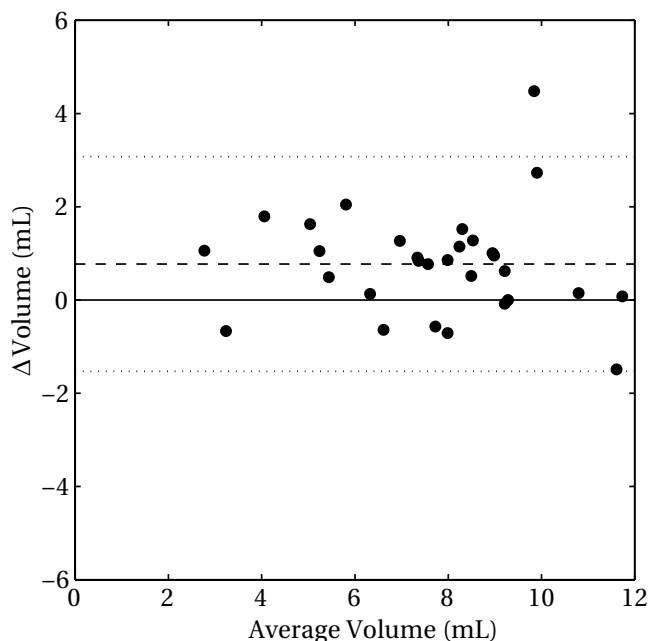
Figure 3.3: Bland-Altman plot showing the difference between the volumes of the CT- and the MRI- delineations versus the average volume in these delineations. The dashed line is the average difference in the volumes; the dotted lines indicate the 95% confidence interval of these differences.

The mean dose to the submandibular gland did not increase significantly among the different delineations for all glands ($p > 0.2$). Furthermore, a separate analysis on the spared and non-spared glands was performed. The mean dose to the spared submandibular glands increased from 31.1 ± 14.7 Gy in the clinical CT/MRI-delineation to 32.3 ± 14.0 Gy in the MRI-delineation, whereas no increase was seen in the non-spared glands (65.3 ± 5.8 Gy and 65.4 ± 5.3 Gy, respectively) (Table 3.1). The V_{40} was 5.3 ± 3.3 mL in the CT-delineations and 5.2 ± 3.2 mL in the CT/MRI-delineations ($p = 0.9$). The V_{40} increased to 6.0 ± 3.6 mL in the MRI-delineations as compared to the CT- and CT/MRI-delineations ($p = 0.002$ and $p < 0.001$, respectively) (Table 3.1). However, the differences in dose among the spared submandibular gland varied largely between patients, ranging from a slight decrease to an increase of 60% in the mean dose (Figure 3.5).
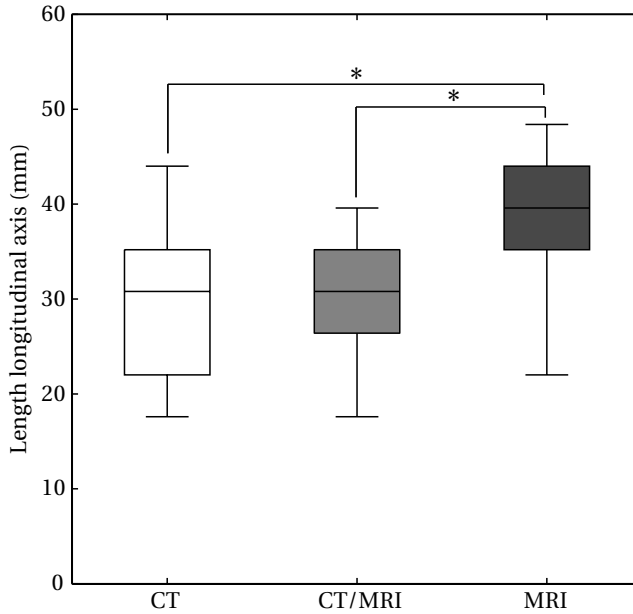
Figure 3.4: Box-plots of the length of the cranial-caudal axis in the CT-, CT/MRI- and MRI-delineations showing the 25th-75th percentile box with the median and the minimum and maximum value as the whiskers. A significant difference in the groups is indicated with * ($p < 0.001$).

Table 3.1: Mean dose and V_{40} for the spared and unspared submandibular glands in the CT-, CT/MRI- and MRI-delineations.

	Dose (Gy)			V_{40} (mL)		
	CT	CT/MRI	MRI	CT	CT/MRI	MRI
	M±SD	M±SD	M±SD	M±SD	M±SD	M±SD
Spared	31.7±14.9	31.1±14.7	32.3±14.0	2.7±2.4	2.7±2.7	3.1±2.7
Unspared	65.5± 5.5	65.3± 5.8	65.4± 5.3	7.1±2.6	6.9±2.4	8.0±2.6
All	52.0±19.6	51.6±19.8	52.2±19.1	5.3±3.3	5.2±3.2	6.0±3.6

Abbreviations: M = mean value; SD = standard deviation.
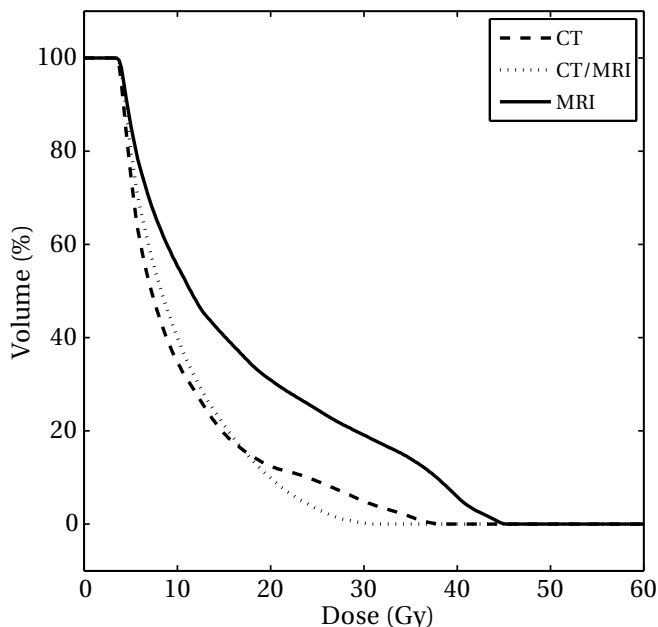
Figure 3.5: Dose-volume histograms (DVHs) of a submandibular gland showing the differences between the CT-, CT/MRI-, and MRI-delineations.

3.4 Discussion

The delineated volume and cranial-caudal extent of the submandibular gland did not vary significantly by adding T_1- and T_2-weighted MRI to the CT image. However, addition of the MR sialography images to the MRI-delineations increased the volume and cranial-caudal extent significantly. The MR sialography images showed the ductal structures and the complete outline of the submandibular glands, including the cranial border, which was difficult to distinguish on CT and T_1- and T_2-weighted MRI.

MR sialography is basically a heavily T_2-weighted MRI scan with fat suppression. Due to the large TE used in the sequence and the high T_2-value of water, tissues containing a large amount of water can be visualized with MR sialography. Therefore, structures such as the salivary ducts and lymph nodes, had a hyper-intense signal on the MR sialography image. The body of the gland appeared as a medium-intense area, due to the water in the acinar cells of the gland. On the other hand, structures with a small amount of water, such as muscles, showed a hypo-intense signal with a low signal-to-noise (SNR) level. The low SNR level in the surrounding tissues made the images look a bit granular.

Besides the differences in imaging parameters, the main difference between MR sialo-graphy and the CT and T_1- and T_2-weighted MRI scans was the orientation of the imaging slices, sagittal for the MR sialography and transverse in the other scans. In a rather sagittally directed organ, like the submandibular gland, the sagittal orientation of the imaging slices in MR sialography could explain the improved visualization of the complete organ. However, sagittal images of the other imaging techniques did not show the clear contrast between the cranial border of the submandibular gland and the surrounding tissues. Furthermore, the average increase of the cranial-caudal length of the submandibular gland in the MRI-delineations was at least two times the slice thickness of the other scans. The diameter of the submandibular gland at that height was much larger than the voxel size (11 mm on average) and it could in principle be detected on the transverse slices. Therefore, the different contrast in MR sialography accounts most for the increased delineated volume and contrast in the cranial part.

No significant differences in delineated volume and cranial-caudal axis were found between the CT- and CT/MRI-delineations, indicating a negligible inter-observer variation. The differences between the CT- and MRI-delineations, performed by the same radiation oncologist and thus lacking an inter-observer variation, showed an increase in delineated volume and thereby a clear added value of the MR sialography images. Furthermore, the Bland-Altman plot (Figure 3.3) showed a constant difference between the delineations, which indicates a more systematic difference. As for an inter-observer variation, the differences would most likely increase with increasing volume.

The differences in the mean dose and V_{40} in the different delineations of the submandibular gland seem rather small in this patient group. First of all, the cranial part of the submandibular gland was not included in the clinical delineation and, therefore, not included in the dose optimization. Because the caudal part of the submandibular gland is located furthest from the elective lymph node area, the dose to this part is mostly reduced in contralateral submandibular gland sparing IMRT [59]. However, including the cranial part of the gland in the dose optimization will reduce the maximum dose to the gland and consequently also the mean dose will be reduced. Secondly, the variation in anatomical orientation of the submandibular gland and target volumes between patients will influence the effect of the larger delineation on the mean dose. The mean dose increased about 60% (from 10 Gy to 17 Gy) in one patient in this study, due to the specific anatomical location of the submandibular gland and the target volumes. Therefore, in specific cases, the delineation will be largely improved using MR sialography and the effect on the dose to these gland will be large (Figure 3.5).

Recent studies on the comparison of ipsilateral and bilateral treatment of the neck showed that the salivary gland function was better in the ipsilateral treated patients, while the loco-regional control was comparable [84, 85]. These results indicate that submandibular gland sparing radiotherapy is achievable at the contralateral side in naso- and oropharyngeal cancer patients with no positive lymph nodes at the contralateral side. In this study, only oropharyngeal cancer patients were included and the

influence on the dose to the submandibular gland in patients with another type of HN cancer might be larger. In laryngeal cancer patients and also in patients with a small hypopharyngeal tumour, the primary tumour target volume is located more caudally to the submandibular gland and bilateral submandibular gland sparing can be easily achieved. Therefore, although in the group of patients the overall effect of a larger delineated volume on the dose parameters was small, a clinical relevant effect was obtained in individual patients and could be obtained in other HN tumour groups.

3.5   Conclusions

When reducing the dose to the submandibular gland is attempted in the radiotherapy treatment, accurate visualization and delineation is a prerequisite. This study showed that T_1- and T_2-weighted MRI in combination with MR sialography was superior to CT and T_1- and T_2- weighted MRI in visualizing the whole submandibular gland, especially in the cranial direction of the gland. However, one should take these results into account on CT when MRI is not available.

Chapter 4

Sparing the contralateral submandibular gland in oropharyngeal cancer patients: A planning study

Abstract

Purpose: The submandibular glands are proposed to be important in preventing xerostomia in head-and-neck cancer patients. We investigated the feasibility of sparing the contralateral submandibular gland (cSMG) by reducing the dose to the contralateral planning target volume (PTV) and by reducing the clinical target volume (CTV)-to-PTV margin.

Materials and methods: Ten oropharyngeal cancer patients with a contralateral elective PTV were included in this planning study, using intensity-modulated radiotherapy (IMRT). The effect on the mean dose to the cSMG of reducing the dose coverage to the contralateral elective PTV from 95 to 90% of the prescribed dose (54 Gy in 1.8 Gy daily fractions) was determined. The influence of reducing the margin for position uncertainty from 5 to 2 mm was investigated.

Results: The mean dose to the cSMG was reduced from 54 Gy to approximately 40 Gy if the dose coverage to the contralateral PTV was reduced to 90% of the prescribed dose. The estimated normal tissue complication probability (NTCP) was reduced below 50%. Reducing the margin from 5 to 2 mm resulted in a decrease in the mean dose to the cSMG of approximately 6 Gy.

Conclusions: Reducing the mean dose to the cSMG below 40 Gy is possible with a reasonable dose coverage of the contralateral elective PTV.

4.1 Introduction

Xerostomia is a severe side effect of radiotherapy in head-and-neck cancer patients. It induces difficulty in swallowing, eating and speaking and gives an early onset of dental caries [5, 86]. A large effort has been put in reducing the dose to the parotid glands [70, 72]. The reduction of the dose to the parotid glands leads to a preservation of the salivary flow after radiotherapy. Unfortunately, patients still complain of a dry mouth [9, 73]. Radiation damage to the submandibular glands has been proposed to explain the remaining subjective feeling of a dry mouth [74, 76, 87, 88].

Sparing the submandibular glands is, however, much more challenging than sparing the parotid glands. The submandibular gland is often located adjacent to the elective clinical target volumes (CTVs). Due to uncertainties in target delineation and patient position during treatment, a margin around the CTV is used to obtain the planning target volume (PTV). This causes an overlap between the submandibular gland and the PTVs, which makes sparing these glands without compromising the dose to the elective PTV complicated. However, the overlap between PTVs and the submandibular gland at the contralateral side is smaller than that at the ipsilateral side, particularly for tumours not crossing the mid line. Furthermore, the probability of microscopic disease is lower at the contralateral side [89]. This suggests a possibility to reduce the dose to the contralateral submandibular gland (cSMG) with acceptable reduction of the tumour control probability (TCP) at the contralateral elective PTV [90].

Whilst there have been a few papers looking at the clinical aspects of sparing the submandibular glands [75–77], there has been little published on the dosimetric details of such sparing. The goal of this planning study was to determine the possibility to reduce the mean dose to the cSMG and to investigate what compromises have to be made to achieve a substantial sparing. Therefore, several plans were made for ten oropharyngeal cancer patients. The reduction in the mean dose to the cSMG was determined in case of normal coverage of the PTVs and in case of a slight and local underdosage to the contralateral electively treated PTV.

4.2 Materials and Methods

4.2.1 Patients

Ten oropharyngeal cancer patients, treated with primary radiotherapy at our department between August 2003 and November 2006, were included in the planning study. Staging was performed according to the TNM staging system [58]. Indications for elective treatment were a N2b nodal stage, a tumour crossing the mid line or a base of tongue carcinoma. The patients had stages T1-T3N0-N2bM0 and in all cases the contralateral lymph nodes were electively treated (Table 4.2). The distribution of TNM stages in these ten patients was comparable to that of the patients treated at our department for oropharyngeal cancer [91].

4.2.2 Imaging and delineation

Each patient underwent a computed tomography (CT) scan (CT aura, Philips Medical Systems, Best, The Netherlands) with intravenous contrast. The slice thickness was 3 mm, the patients were positioned with an immobilization mask. Delineation of the CTVs and the organs at risk (OARs) was performed by a radiation oncologist as described previously [71].

The contralateral elective CTV consists of the level II lymph node area as described by Grégoire *et al.* [92]. The level II lymph node area can be subdivided in a level IIa and IIb area, the level IIa area is located adjacent to the submandibular gland. Sparing the cSMG can influence the dose to the contralateral electively treated CTV, especially in the level IIa lymph node area. Therefore, the dose to the complete contralateral elective CTV and the level IIa lymph node area alone should be monitored strictly, which required the delineation of this contralateral level IIa lymph node area. The lowest dose to 1 cc of the PTV volume was used to monitor the dose coverage to the elective CTV.

4.2.3 Margins

Margins are applied to the CTVs in order to obtain the PTVs. Clinically, a margin of 5 mm is used. This margin might be decreased by applying new position verification tools such as daily cone-beam CT or fiducial markers [93]. As previously described by van Asselen *et al.* [94], a decrease in margin will lead to a substantial reduction in dose to the parotid glands of approximately 1.3 Gy/mm. Margins of 5 mm and 2 mm were used, to investigate to what extent the increased workload associated with an improved position verification will result in a benefit for the submandibular glands.

4.2.4 Treatment planning

The planning CT scan was transported to the inverse treatment planning module of the planning system (PLATO-ITP, Nucletron, Veenendaal, The Netherlands). An intensity-modulated radiation therapy (IMRT) technique with nine equally distributed 6 MV photon beams starting at 0° was used. The plans were calculated using a dose grid of 1.9 mm. The prescribed dose was 69 Gy in 2.3 Gy daily fractions to the gross tumour volume (PTV-GTV) and 66 Gy in 2.2 Gy daily fractions to the PTV-CTV. The prescribed dose to the electively irradiated PTVs was 54 Gy in 1.8 Gy daily fractions, according to the clinical protocol [71].

In order to achieve salivary gland sparing and an appropriate target coverage, the parotid glands and the cSMG were divided in two parts. This was done using VolumeTool, a delineation tool developed at our department [95]. The border of the two parts was located at 15 mm from all PTVs in all three dimensions (Figure 4.1), which is the distance where the dose gradient can theoretically decrease from 54 Gy to 0 Gy. This resulted in a part adjacent to or overlapping with the PTVs and a part at a distance of 15 mm from

the target volumes. Thereby, the distant part could be spared independently without influencing the dose to the PTVs. Although this distant part has a small volume, it influences the dose optimization process, due to the fact that the cost function in the PLATO planning system does not take the volume size of an OAR into account.

For each patient, four different IMRT plans were made, of which the characteristics were summarized in Table 4.1. The parotid glands were spared in all plans to the minimal possible mean dose at which the target coverage of 99% of the volume of all the PTVs was at least 95% of the prescribed dose. The first plan (plan A) included only the sparing of the parotid glands, both submandibular glands were ignored. In the second plan (plan B), the dose to 99% of the volume of the PTVs was at least 95% of the prescribed dose, which is the clinically accepted target coverage. In the third plan (plan C), a concession was made in sparing the cSMG and the coverage of 99% of the volume of the contralateral elective PTV. This coverage had to be at least 90% of the prescribed dose, instead of 95% clinically used. The fourth plan (plan D) was made to determine which compromises had to be made in the dose coverage of all the PTVs in order to get the mean dose of the cSMG below 40 Gy. At this dose, the normal tissue complication probability (NTCP) of the parotid gland is 50% [23]. Plan D was not performed if the mean dose to the cSMG in plan B or C was already below 40 Gy.

Table 4.1: The characteristics of the different IMRT plans performed in this planning study

Plan	Constraints
A	All PTVs: > 95% of the prescribed dose
	No cSMG sparing
B	All PTVs: > 95% of the prescribed dose
C	Contralateral elective PTV: > 90% of the prescribed dose
	Other PTVs: > 95% of the prescribed dose
D	Mean dose of the cSMG < 40 Gy

4.2.5 NTCP

The effect of a reduction of the mean dose to the cSMG can be expressed as a change in the normal tissue complication probability (NTCP). Some research has been performed on sparing the submandibular glands [75–77], Murdoch-Kinch *et al.* [75] found a threshold dose of 39 Gy, above which the submandibular flow rate was negligible. This corresponds to the dose to the parotid gland with an NTCP of 50% as described by Roesink *et al.* [23], where a complication was defined as the cumulated stimulated parotid flow rate of less than 25% of the pre-RT flow rate. This NTCP curve was used for the submandibular gland in this planning study.

4.3 Results

4.3.1 Dose distributions

In general, dose distributions were obtained that met our criteria with regard to OAR sparing and dose homogeneity (Figure 4.1). The volume that received more than 107% of the prescribed dose was always a small volume located inside the GTV and the dose to the target volumes was within the constraints described in Table 4.1 (Table 4.2). The dose to the brain and spinal cord was always within the clinical constraints.

When the cSMG was spared more rigorously, the dose gradient between the contralateral electively treated PTV and the cSMG became steeper. This resulted in a movement of, for example, the 40 Gy and 51 Gy isodose lines (Figure 4.1).

Table 4.2: Dose parameters for submandibular gland sparing for all patients

TNM-stage	Plan C				Plan D			
	PTV_{prim}		PTV_{elec}	cSMG	PTV_{prim}		PTV_{elec}	cSMG
	D_{min}	$V_{<95\%}$	D_{min}	D_{mean}	D_{min}	$V_{<95\%}$	D_{min}	D_{mean}
	(Gy)	(%)	(Gy)	(Gy)	(Gy)	(%)	(Gy)	(Gy)
T2 N0	62.5	1.3	49.9	37.74	62.5	1.3	49.9	37.74
T2 N1	64.1	0.2	45.6	34.08	64.1	0.2	45.6	34.08
T2 N2b	64.3	1.0	47.7	53.38	54.6*	2.6*	40.1*	38.82*
T1 N2b	62.3	0.9	48.4	50.63	55.8*	2.5*	44.0*	34.47*
T1 N2b	62.9	0.7	47.3	44.84	64.1	0.4	41.8	36.44
T2 N0	62.9	0.5	48.1	35.29	62.9	0.5	48.1	35.29
T3 N0	60.4*	1.9*	48.8*	43.15*	59.5*	1.6*	48.1*	40.06*
T2 N2b	62.9	0.6	47.9	41.10	62.1	1.0	45.2	37.84
T3 N0	60.3†	1.5	50.0	51.50	55.3*	4.3*	49.4*	46.88*
T1 N0	62.1	1.5	48.9	45.03	62.6	0.8	43.6	37.22

Abbreviations: PTV_{prim} = primary PTV; PTV_{elec} = contralateral elective PTV; D_{min} = minimal dose (Gy) to 1 cc of the volume; $V_{<95\%}$ = volume (%) that received < 95% of the prescribed dose; D_{mean} = mean dose (Gy).

* The plans excluded based on PTV-CTV underdosage as a result of cSMG sparing.

† The coverage of the PTV-CTV in this plan is the same as in plan A.

4.3.2 Mean dose and NTCP

The average of the mean dose to the cSMG of the ten patients of plan A, when no sparing of the cSMG was performed, was approximately 57 Gy for both the margins (Figure 4.2(a)), what resulted in an average NTCP value of approximately 85% (Figure 4.2(b)). The average of the minimal dose to the contralateral elective PTV was sufficient for both the margins, approximately 50 Gy (Figure 4.2(a), Table 4.3).

The effort in sparing the cSMG without concessions to the dose coverage of the target volumes (plan B) resulted in an average of the mean dose to the cSMG of 54 Gy for the 5
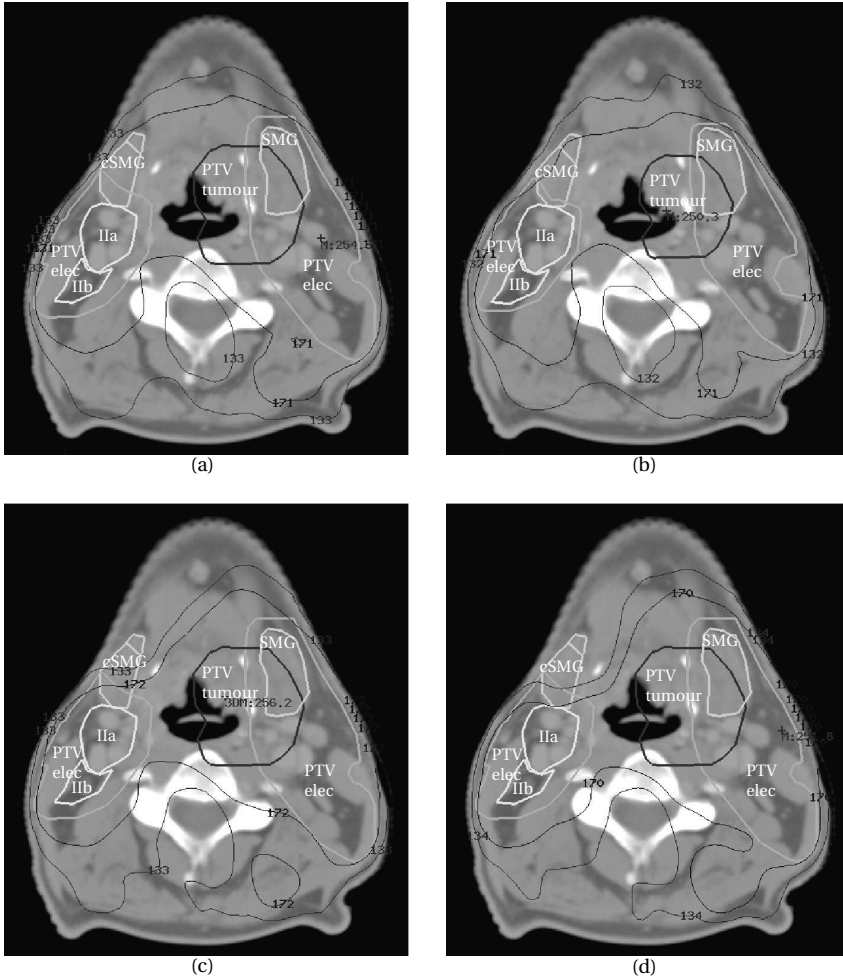
Figure 4.1: Typical dose distributions for the different IMRT plans aiming at sparing the cSMG in one oropharyngeal patient. The margin to obtain the PTV was 5 mm in (a, c and d), in (b) it was 2 mm. In (a and b) (plan A), only the parotid glands were spared. The cSMG was spared with a dose to the contralateral electively treated PTV of at least 95% (c), (plan B) and this dose was reduced to 90% in (d) (plan C). The thick lines are the delineated volumes: the PTV of the tumour (PTV tumour), the elective treated PTVs (PTV elec), the level IIa and IIb of the contralateral elective CTV (IIa and IIb), and the SMG. The cSMG is divided in a part adjacent or overlapping with the PTVs and a part at a distance of 15 mm from the target volumes. The thin lines are the isodose lines. The 171 cGy isodose line is 95% of the prescribed dose to the elective treated volumes; the 133 cGy line is the 40 Gy isodose line.

mm margin plans. The average of the mean dose values for the 2 mm margin plans was 49 Gy. The corresponding NTCP values were 80% and 70%, respectively. The average of the minimal dose to the contralateral elective PTV did not decrease (Figure 4.2, Table 4.3).

The reduction in the dose coverage of the contralateral elective PTV from 95% to 90% of the prescribed dose (plan C) resulted in an average of the mean dose to the cSMG of approximately 40 Gy for both the margin plans. The average of the minimal dose to the contralateral elective PTV decreased to 48 Gy in both the margin plans (Figure 4.2). One plan was excluded in the average values for both margins, due to an underdosage of the primary PTV (Table 4.3).

The average of the mean dose values to the cSMG for plan D was 36 Gy for both the margins. The average of the minimal dose to the contralateral elective PTV decreased to 46 Gy in the 5 mm plans, but remained constant in the 2 mm margin plans. Four plans were excluded in the 5 mm margin plans and two were excluded in the 2 mm margin plans, due to an underdosage of the primary PTV. The limit of 40 Gy for the mean dose to the cSMG resulted in an average dose to 99% of the volume of the contralateral electively treated PTV between 85% and 90% of the prescribed dose for both margins, while the other PTVs were correctly covered (Figure 4.2, Table 4.3).
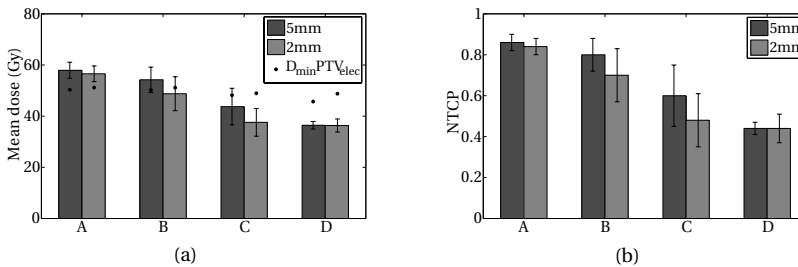
Figure 4.2: The average of the mean doses (a) and NTCP values (b) of the IMRT plans aiming at cSMG sparing in oropharyngeal cancer patients. On the horizontal axis, the plan labels are denoted. In plan A only the parotid glands were spared. The cSMG was spared with a dose coverage to the contralateral elective PTV of 95% in plan B and of 90% in plan C. In plan D, the aim was to reduce the mean dose to the cSMG below 40 Gy. One plan was excluded in the average of plan C for both the margins. In the average of plan D, respectively, four and two plans were excluded for the 5 mm and 2 mm margin plans. The results of the plans with a margin to obtain the PTVs of 5 mm are visualized in the dark grey bars, the results of the margin of 2 mm in the light grey bars. The error bars denote the standard deviation of the plans. The dots represent the average of the minimal dose of the contralateral elective PTV (a).

Table 4.3: Average dose parameters for submandibular gland sparing using various planning strategies

5 mm plan	PTV$_{prim}$			PTV$_{elec}$			cSMG
	D$_{min}$ (Gy)	D$_{mean}$ (Gy)	V$_{<95\%}$ (%)	D$_{min}$ (Gy)	D$_{mean}$ (Gy)	V$_{<95\%}$ (%)	D$_{mean}$ (Gy)
A	63.2	70.5	0.6	50.3	56.4	1.8	57.9
B	63.1	70.5	0.7	50.2	56.5	1.7	54.2
C	62.7	70.5	0.9	48.2	56.2	3.5	43.7
D	63.0	70.4	0.7	45.7	55.8	5.2	36.4
2 mm plan							
A	64.8	71.2	0.2	51.2	56.5	1.2	56.6
B	64.4	70.1	1.4	51.2	56.4	1.2	48.8
C	63.5	71.0	1.3	49.0	56.4	3.6	37.6
D	63.6	70.1	1.4	48.8	56.3	3.5	36.3

Abbreviations: PTV$_{prim}$ = primary PTV; PTV$_{elec}$ = contralateral elective PTV; D$_{min}$ = minimal dose (Gy) to 1 cc of the volume; D$_{mean}$ = mean dose (Gy); V$_{<95\%}$ = volume that received < 95% of the prescribed dose.

The maximum dose to the PTVs remained constant for the various plans.

4.4 Discussion

The mean dose to the cSMG in oropharyngeal cancer patients could be reduced from 54 Gy to approximately 40 Gy with an acceptable reduction in the dose coverage of the contralateral elective PTV.

Plans A and B (Table 4.1) were both consistent with the current clinical constraints for PTV dose coverage. The effort of sparing the cSMG within these constraints (plan B) led to an average dose reduction of a few Gy with regard to plans without cSMG sparing (plan A). The reduction in dose coverage to the contralateral elective PTV from 95 to 90% (plan C) of the prescribed dose (54 Gy) resulted in an average of the mean dose to the cSMG of approximately 40 Gy.

In the average value of the mean dose to the cSMG of plan C, 1 plan was excluded for both the margin plans. In the average of plan D, four plans were excluded for the 5 mm margin plans and two for the 2 mm margin plans. In these plans, the dose to the primary PTV was seriously reduced as a result of the cSMG sparing, which could occur because the PLATO planning system does not use hard constraints. A correlation between the TNM stage of the patient and the exclusion of the plan could not be found. The anatomical orientation of the PTVs and the cSMG is thought to be of more influence. Since most plans were excluded in the average of plan D, it can be concluded that it is not possible in all patients to reduce the dose to the cSMG to below 40 Gy while adequately covering the primary PTV. Furthermore, a mean dose to the cSMG of

approximately 50 Gy in plan C is an indication of underdosage to the primary PTV in plan D.

The division of the salivary glands in two parts in order to maximally spare the salivary glands was required because the planning system cannot reduce the mean dose to an OAR. The division of the salivary glands was chosen at a distance of 15 mm, at which the dose gradient theoretically can decrease from 54 Gy to 0 Gy. This resulted in a part of the salivary gland that was adjacent to or overlapping with the target volumes which was difficult to spare. The remaining part could therefore be spared rather easy in order to reduce the mean dose to the whole gland.

Currently, the margin to obtain the PTVs at our department amount to 5 mm. In this planning study, a margin of 2 mm was chosen between this clinical applied margin of 5 mm and a theoretical margin of 0 mm. Several studies have reported adequate margins in head-and-neck cancer patients [96–98], which range from 1.5 to 5 mm. These margins are applied without cone-beam CT position verification. The use of cone-beam CT or fiducial markers [93] will probably make it feasible to use a margin of 2-3 mm, which is well within the range of these published margins. Reducing the margin from 5 to 2 mm resulted in an extra reduction in mean dose to the cSMG of a few Gy. This reduction in mean dose to the cSMG is in agreement with the reduction in mean dose to the parotid gland of 1.3 Gy per mm margin reduction as described by van Asselen *et al.* [94].

Some clinical studies have been performed on sparing the submandibular gland [75–77]. According to Burlage *et al.* [74], the submandibular glands and parotid glands have similar acute radio-sensitivity. In another study, the threshold dose above which the submandibular flow rate was negligible was found to be 39 Gy [75]. This corresponds nicely to the mean dose at which the NTCP value is 50% for the parotid gland is 39 Gy at one year after RT [23].

The underdosage of the target volumes was restricted to the contralateral elective PTV and only occurred in the CTV-PTV margin volume adjacent to the cSMG. The reduction in dose coverage to the contralateral elective PTV from 95 to 90% of the prescribed dose (54 Gy) corresponds to reducing the minimal dose to 99% of the volume of this PTV by 2.7 Gy. Eisbruch *et al.* [99] denoted the level IIa lymph node area, including the jugulodigastric lymph nodes as the highest risk area for sub-clinical lymph node metastasis. Therefore, the dose coverage of the level IIa lymph node area located in the contralateral elective PTV must be adequate. The dose to the contralateral elective PTV in these plans was always within the clinical accepted range. This indicated that it is possible to reduce the mean dose to the cSMG without significant underdosage of the contralateral elective CTV and hence, the contralateral level IIa lymph nodes including the jugulodigastric lymph nodes.

Jensen *et al.* [89] showed that ipsilateral treatment of selected oropharyngeal cancer patients resulted in the same loco-regional control and overall survival when com-

pared to bilateral treatment. This retrospective study was not randomized, however, and the number of patients with unilateral treatment, where bilateral treatment would have been the standard treatment, was small. According to Saarilahti *et al.* [76], sparing the cSMG resulted in a better maintenance of the unstimulated total salivary flow rate, compared to patients with only parotid gland sparing. The cSMG sparing was not associated with loco-regional cancer recurrence within the spared volume. Both the studies, however, contain few patients and need to be validated in a randomized study with larger patient groups. A theoretical study by de Kruijf *et al.* [90] indicates that locally underdosing the elective PTVs in head-and-neck cancer patients was associated with a decrease in sub-clinical disease TCP of typically a few percent.

Results from this theoretical planning study will lead to a clinical study to spare the cSMG. A dose coverage of 90% of the prescribed dose to the contralateral electively treated PTV could be an acceptable compromise to reduce the dose to the cSMG. Due to the 90% dose coverage of the contralateral elective PTV, there is a chance that the recurrence rate will rise. The number and location of recurrences will therefore be monitored strictly.

A reduction in the CTV-PTV margin for reducing the mean dose to the salivary glands is only useful in the area adjacent to the salivary glands. Therefore, non-uniform margins will be used in order to reduce the overlap area between the salivary glands and the PTVs. This will lead to a reduction in the mean dose to the salivary glands as compared to the current clinical margins. The functionality of the submandibular glands will be determined using flow measurements [71], which will also make it possible to determine a dose-response curve.

4.5   Conclusion

Reducing the mean dose to the cSMG in patients with oropharyngeal cancer from 54 Gy to values below 40 Gy is theoretically possible and is associated with a slight and local reduction in the dose to the contralateral elective PTV to 90% of the prescribed dose.

Chapter 5

Improved immobilization using an individual head support in head-and-neck cancer patients

Abstract

The benefits of a patient-specific head support, developed to improve immobilization during radiotherapy, were determined in head-and-neck cancer patients. Cone-beam CTs were registered to the planning CT in five regions. Compared to the standard head support, the individual head support decreased the systematic and random error of the inter- and intrafraction displacements and reduced deformations.

5.1 Introduction

In the last few years, intensity-modulated radiotherapy (IMRT) has been used increasingly for head-and-neck (HN) cancer patient treatments. With IMRT, more conformal dose distributions can be realized, which is beneficial for sparing the salivary glands [59]. With these conformal dose distributions and steep dose-gradients near critical organs, immobilization of the HN region becomes more important. Recent availability of in-room imaging techniques, such as cone-beam CT (CBCT), make it possible to detect patient set-up errors and intrafractional errors in 3D [100, 101]. With CBCT, both the translational and rotational set-up errors can be visualized, which improves the position verification of the patients [102]. However, several studies have shown the presence of displacements between bony structures in the HN region [103, 104]. Improvement of the immobilization of patients is required to reduce these deformations [105]. In cooperation with Civco medical solutions, our department developed an improved individual head support.

In this study, immobilization with the individual head support was compared to immobilization with a standard head support. The inter- and intrafraction displacements in five HN regions and deformations between these regions were analysed for both head supports.

5.2 Materials and Methods

Twenty-two HN cancer patients were selected for this study, irrespective of tumour stage and location. Patients were immobilized with an individual five-point thermoplastic mask. For 10 patients, a standard head support was used (Figure 5.1(a)); 12 patients had an individual head support (Figure 5.1(b)), which was customized for each patient (Civco Medical Solutions, Kalona, Iowa, USA) and was compatible with the standard mask system.

The standard head support was made of low-density foam and came in two standard shapes for HN treatment (Figure 5.1(a)).

The individual head support was made of impression foam with a thermoplastic cover on top (Figure 5.1(b)). The head of the patient was firmly pressed into the specially shaped impression foam by placing pressure on the forehead and shoulders, assuring the desirable neck curvature. The thermoplastic cover placed on top bound to the foam and fixated the shape of the support. After creating the individual head support, the five-point thermoplastic mask was made. Creating the individual head support took a few minutes. The costs of the individual head support, which can only be used for one patient, are approximately 80 Euro.

Each patient received a computed tomography (CT) scan (CT aura, Philips Medical Systems, Best, The Netherlands) for planning of the IMRT treatment. The CT was reconstructed with a slice thickness of 2 mm and an in-plane pixel size of 0.5 mm.
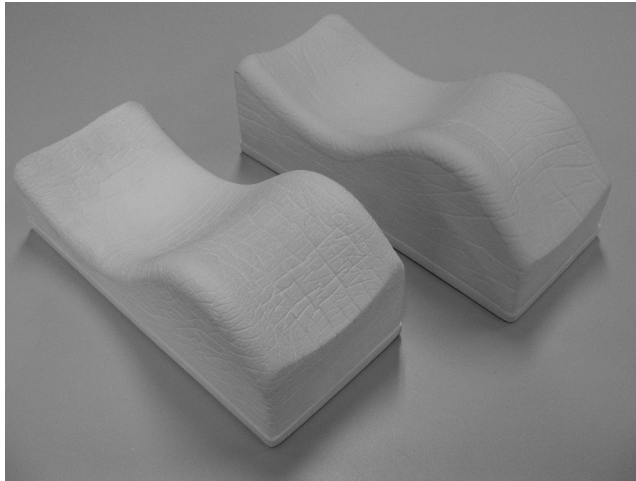
(a)
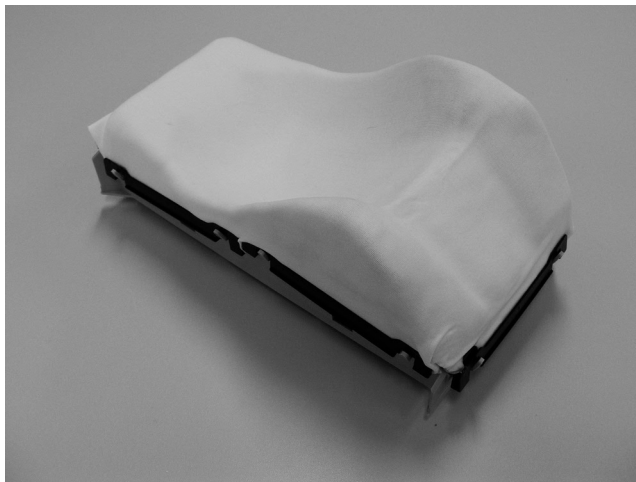
(b)

Figure 5.1: The standard head supports (a) and an individual head support (b).

In the first week of treatment, daily CBCT scans were acquired (XVI, Elekta, Stockholm, Sweden), immediately before and after each fraction. Subsequently, CBCT scans were made once a week, before and after each fraction. The CBCT scans were reconstructed with an isotropic voxel size of 1 mm. The CBCT scans made before each fraction were used to determine the reproducibility of the patient positioning, i.e. the interfraction displacement. The differences between the CBCT scans made before and after each treatment fraction indicated the stability of the patient during treatment, i.e. the intrafraction displacement.

For each patient, five rectangular shaped alignment boxes were defined to determine the inter- and intrafraction displacements [104]: HN area (A), skull (B), mandible (C), vertebrae C1–C3 (D), and C4–C6 (E) (Figure 5.2). These boxes were created on the CT, taking the cranial and caudal extent of the CBCT scans into account, and thus assuring a good quality of all CBCT scans in the complete box.
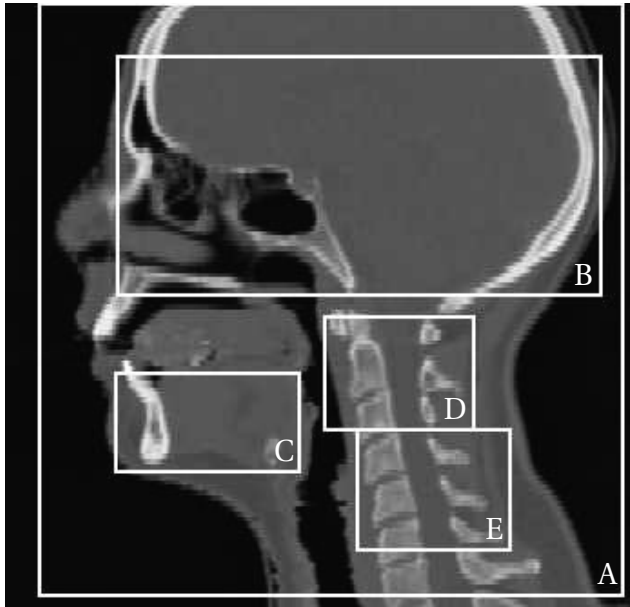
Figure 5.2: The alignment boxes of the HN area (A), skull (B), mandible (C), vertebrae C1–C3 (D) and vertebrae C4–C6 (E).

Due to the limited availability of the XVI software for research purposes at our department, the registrations were performed using another registration program, Elastix [62]. This program facilitated full, automatic registration of large sets of images.

Before registration, the CT and CBCT scans were windowed to visualize only the bony structures. The isocentre of the CBCT was aligned with the isocentre of the CT before

the start of the registration, comparable to the procedure in the XVI software. The rigid registration method was based on a normalized correlation coefficient algorithm, with the centre of rotation in the centre of the alignment box. Each registration resulted in a transformation matrix, consisting of a rotation over the left–right (LR), anterior–posterior (AP), and cranial–caudal (CC) axes, followed by a translation in the LR, AP, and CC directions.

To determine the consistency of the registrations, two comparisons were made on all available CBCT scans. First, the results of Elastix were compared with the results of the XVI software. Therefore, the transformation matrices of the clinical registrations in XVI were compared with the registrations using the clinical clipbox in Elastix. For each translation and rotation, the average and standard deviation of the differences between Elastix and XVI were calculated.

To determine the accuracy of the Elastix software, registrations of the alignment box of the skull and an extra alignment box around the maxilla were compared. The registration accuracy was determined by calculating the differences between the transformation matrices. Since these bony structures are anatomically fixed to each other, the differences in the rotations and translations were a measure of the robustness of the registration.

During treatment, a patient set-up correction protocol was used to correct for large differences in patient positioning. However, this correction protocol might mask the differences between the two head supports. Since the purpose of this study was to compare the two head supports and not investigate the quality of this correction protocol, the clinical table corrections were subtracted from the translations of the registration. Therefore, the positioning errors are reported without the set-up corrections.

The interfraction displacements were separated in a systematic (Σ) and random (σ) uncorrected error [106] for the two head supports, separately. For each patient, the average (M_p) and the standard deviation (SD_p) of the displacements over all fractions were calculated. The systematic error followed from the standard deviation of the M_p of all patients with the same head support; the random error was calculated as the root-mean-square over all SD_p. The translations and rotations in all directions were treated independently. The intrafraction displacements were analysed using the random error only.

A deformation was defined as the difference in translation and rotation between two alignment boxes. The deformations were also expressed as systematic and random errors. Consequently, the difference in displacement instead of the displacement itself was analysed, for the inter- and intrafraction errors separately.

The results in this study were analysed in two ways. First, the overall difference between the two head supports was analysed. Therefore, the interfraction displacement errors of all translations and rotations in all regions of interest (Supplementary Table A.1) of both head supports, were tested pairwise and non-parametrically using the Wilcoxon

signed-rank test. The interfraction systematic and random error and the intrafraction error were analysed separately. Next to the displacements, this analysis was also performed on the deformations in both head supports.

Secondly, the differences in the systematic and random error for each translation or rotation were tested for significance. Therefore, the underlying patient data of both head supports, resulting in, e.g., the random translation error in the AP direction for the mandible, were used to test for significance. A Mann-Whitney U test was performed on all SD_p to test if the random errors were significantly different; a Levene test was performed on all M_p to test whether the standard deviation of the distributions (the systematic error) was equal.

All tests were performed using SPSS, version 16.0 (SPSS Inc., Chicago, USA).

5.3 Results

The average translation difference (M) in the XVI-Elastix comparison on all 401 CBCT scans, averaged over all three directions, was 0.16 ± 0.45 mm (1 SD), and the average rotation difference was 0.00 ± 0.39°. For the comparison between the skull and the maxilla, the average translation difference was 0.13 ± 0.34 mm, and the average rotation difference was 0.01 ± 0.19°. These differences were acceptable and the Elastix software was used for further analysis of the data.

The overall difference between the two head supports was analysed by comparing all translations and rotations of the two head supports pairwise. The systematic error and the random error of the interfraction displacements decreased significantly with a p-value of 0.003 and < 0.001, respectively, when using the individual instead of the standard head support. The decrease in intrafraction displacement, analysed by the random error only, was significant with a p-value of < 0.001.

The systematic error of the interfraction displacements reduced on average by 20% ± 30% (1 SD). Statistically significant reductions were found for rotations in vertebrae C1–C3 (Supplementary Table A.1).

The random error reduced in almost all directions by approximately 25% ± 25%. Statistically significant differences between the head supports were reached mainly for translations in the LR direction and rotations over the AP- and CC-axis (Supplementary Table A.1).

The intrafraction displacements were reduced on average by 40% ± 20% using the individual head support. The reductions were mainly significant for translations along the LR-axis and rotations over the AP-axis (Supplementary Table A.2).

Deformations between the different regions were in general smaller for the individual head support than for the standard head support. The largest reductions were observed in the neck region. For the deformation between the C1–C3 region and the skull,

the systematic error of the translation along the AP-axis reduced from 2.7 mm with the standard head support to 1.1 mm using the individual head support (Supplementary Table A.3 and A.4).

A significant decrease ($p = 0.04$) in the overall systematic error was seen in the interfraction deformations for the individual head support. The intrafraction deformations, analysed by the random error, were significantly smaller for the individual head support ($p < 0.001$).

5.4 Discussion

The use of a patient-specific head support for HN cancer patients resulted in a reduction of positioning errors, as compared with the standard head support. Both the interand intrafraction errors of the translations and rotations were significantly reduced using the individual head support. Thus, both the reproducibility and stability of the patient positioning were improved. Furthermore, the individual head support showed smaller deformations and a smaller variation in deformations than the standard head support.

When the interfraction systematic errors of the translations and rotations were inspected for each alignment box separately, only the reduction of the rotation errors in vertebrae C1–C3 was statistically significant. The largest differences in the random errors were observed in rotations over the AP- and CC-axes and translations along the LR-axis, in both the inter- and intrafraction displacements. These translations and rotations corresponded to displacements in the coronal plane.

The reduction in deformation errors, when using the individual instead of the standard head support, was largest in the deformations between the neck area and the skull or HN area.

The individual head support is more enclosing the lateral sides of the neck and the head, restricting mainly the movement in the coronal plane. Therefore, reductions were not found in all directions. The absence of significant differences in the lower neck was probably caused by the fact that the individual head support does not support the lower neck. Extension of the head support in the caudal direction might further improve immobilization of this region.

Since the uncorrected patient positions were reported in this study, a correction protocol would decrease the interfraction systematic error in translations. Therefore, differences in the interfraction systematic error of the translations between the head supports would also be reduced. The random error would, however, remain the same or even increase for a population without time trends [107]. Consequently, if we compared our results of the standard head support to the values reported by van Kranen *et*

al. [103], the systematic errors reported in this study were larger and the random errors were smaller.

The patient groups were rather small (10 and 12 patients) and contained outliers. The non-parametrical character of the applied statistical tests resulted in very robust tests for significance, rather insensitive to outliers. Translating the reduction in the systematic and random error to a reduction of the margins was not possible in this small patient group. Further studies, including more patients, are required to determine the reduction in treatment margins.

5.5   Conclusion

HN cancer patients experience relatively large displacements and deformations during treatment. Improvement in immobilization using an individual head support reduced the systematic and random error of these displacements and deformations and the reproducibility and stability of the patient positioning was improved. The individual head support is now used in our clinic for all high-precision HN- and brain cancer treatments when CBCT is used.

Appendix 5.A   Supplementary Tables

Table A.1: The systematic (Σ) and the random (σ) error of the interfraction translations and rotations of head-and-neck cancer patients

		Translations (mm)			Rotations (°)		
		LR	AP	CC	LR	AP	CC
		SHS-IHS	SHS-IHS	SHS-IHS	SHS-IHS	SHS-IHS	SHS-IHS
Σ	HN area	1.53-1.24	3.09-1.88	1.29-1.74	1.22-0.77	1.42-0.72	1.16-0.51
	Skull	1.66-1.16	2.92-2.18	1.27-2.01	1.11-1.22	1.50-0.85	1.19-0.55
	Mandible	1.70-1.30	3.37-2.00	1.60-1.71	1.89-0.97	1.51-0.77	1.22-0.82
	C1–C3	2.01-1.44	2.80-2.58	1.45-1.92	1.58-1.49	<u>1.35-0.53</u>	<u>2.63-1.34</u>
	C4–C6	2.43-1.25	3.84-3.09	1.39-2.60	1.38-1.62	0.97-1.10	1.48-1.11
σ	HN area	<u>1.08-0.63</u>	1.80-0.86	1.35-0.90	0.78-0.51	<u>0.76-0.51</u>	<u>0.79-0.49</u>
	Skull	<u>1.07-0.63</u>	1.95-1.03	1.44-0.95	0.88-0.62	<u>0.75-0.49</u>	<u>0.79-0.49</u>
	Mandible	<u>1.12-0.69</u>	1.58-0.95	1.38-0.83	0.77-0.71	<u>0.83-0.53</u>	<u>0.85-0.53</u>
	C1–C3	1.19-0.97	1.74-1.20	1.59-1.77	1.30-1.40	0.77-0.71	1.22-1.14
	C4–C6	1.15-0.91	1.85-1.58	1.10-1.24	0.67-1.05	0.68-0.57	1.03-0.95

Abbreviations: LR = left–right; AP = anterior–posterior; CC = cranial–caudal; SHS = standard head support; IHS = individual head support.

The underlined values had a significant difference.

Table A.2: The random (σ) error of the intrafraction translations and rotations of head-and-neck cancer patients

		Translations (mm)			Rotations (°)		
		LR	AP	CC	LR	AP	CC
		SHS-IHS	SHS-IHS	SHS-IHS	SHS-IHS	SHS-IS	SHS-IHS
σ	HN area	<u>0.88-0.34</u>	1.11-0.40	0.76-0.47	0.44-0.25	<u>0.42-0.23</u>	0.41-0.28
	Skull	<u>0.84-0.38</u>	1.27-0.51	0.84-0.51	0.54-0.32	<u>0.40-0.27</u>	0.40-0.30
	Mandible	<u>0.95-0.35</u>	<u>1.15-0.52</u>	0.86-0.54	<u>0.69-0.40</u>	<u>0.56-0.30</u>	0.49-0.36
	C1–C3	<u>0.98-0.59</u>	0.92-0.73	0.75-0.64	0.64-0.66	0.42-0.35	<u>1.05-0.99</u>
	C4–C6	0.91-0.72	1.02-0.87	0.84-0.61	0.42-0.44	0.45-0.43	0.91-0.71

Abbreviations: LR = left–right; AP = anterior–posterior; CC = cranial–caudal; SHS = standard head support; IHS = individual head support.

The underlined values had a significant difference.

Table A.3: The systematic (Σ) and the random (σ) error of the interfraction deformations of head-and-neck cancer patients

		Translations (mm)			Rotations (°)		
		LR SHS-IHS	AP SHS-IHS	CC SHS-IHS	LR SHS-IHS	AP SHS-IHS	CC SHS-IHS
Σ	HN area vs Skull	0.21-0.37	0.58-0.73	0.47-0.51	0.36-0.58	0.13-0.22	0.06-0.08
	HN area vs Mandible	0.24-0.43	0.72-0.94	0.64-0.44	1.10-0.72	0.19-0.33	0.10 - 0.60
	HN area vs C1–C3	1.99-0.86	2.55-1.16	0.62-1.31	1.72-1.67	0.84-0.59	2.36-1.25
	HN area vs C4–C6	1.52-1.04	2.41-1.59	1.24-1.35	1.71-2.08	1.58-1.10	1.72-0.93
	Skull vs Mandible	0.31-0.39	1.17-1.43	0.96-0.85	1.37-1.11	0.25-0.42	0.12-0.66
	Skull vs C1–C3	2.14-1.00	2.70-1.14	0.64-1.67	1.84-2.10	0.95-0.75	2.39-1.27
	Skull vs C4–C6	1.60-1.20	2.65-1.71	1.17-1.59	1.56-2.35	1.70-1.30	1.77-0.94
	Mandible vs C1–C3	1.93-1.04	2.54-1.81	1.05-1.32	1.80-1.84	0.87-0.74	2.34-1.41
	Mandible vs C4–C6	1.39-1.18	2.42-1.84	1.23-1.31	2.45-2.01	1.69-1.25	1.72-1.07
	C1–C3 vs C4–C6	1.10-0.73	1.48-1.51	1.43-1.22	2.41-1.95	1.05-0.90	1.70-0.87
σ	HN area vs Skull	0.22-0.20	0.43-0.46	0.27-0.36	0.27-0.34	0.13-0.15	0.06-0.07
	HN area vs Mandible	0.30-0.22	0.77-0.52	0.40-0.39	0.72-0.55	0.23-0.22	0.26-0.25
	HN area vs C1–C3	0.76-0.71	1.99-1.07	0.93-1.19	1.50-1.32	0.48-0.45	1.14-1.07
	HN area vs C4–C6	0.69-0.78	1.50-1.53	0.72-0.89	0.90-1.11	0.73-0.68	1.08-0.96
	Skull vs Mandible	0.33-0.33	0.99-0.74	0.54-0.64	0.90-0.76	0.23-0.27	0.28-0.27
	Skull vs C1–C3	0.80-0.71	2.05-1.20	1.03-1.36	1.59-1.54	0.55-0.51	1.15-1.08
	Skull vs C4–C6	0.71-0.81	1.58-1.76	0.88-1.15	1.04-1.31	0.80-0.74	1.09-0.98
	Mandible vs C1–C3	0.85-0.80	2.06-1.26	1.06-1.27	1.63-1.49	0.59-0.53	1.15-1.07
	Mandible vs C4–C6	0.73-0.80	1.86-1.73	0.75-0.86	1.05-1.21	0.83-0.74	1.09-0.96
	C1–C3 vs C4–C6	0.57-0.80	0.67-1.05	0.56-0.86	1.06-1.13	0.49-0.72	0.62-0.79

Abbreviations: LR = left–right; AP = anterior–posterior; CC = cranial-caudal; SHS = standard head support; IHS = individual head support.

Table A.4: The random (σ) error of the intrafraction deformations of head-and-neck cancer patients

		Translations (mm)			Rotations (°)		
		LR SHS-IHS	AP SHS-IHS	CC SHS-IHS	LR SHS-IHS	AP SHS-IHS	CC SHS-IHS
σ	HN area vs Skull	0.18-0.14	0.51-0.30	0.22-0.26	0.26-0.25	0.10-0.10	0.05-0.06
	HN area vs Mandible	0.31-0.17	0.68-0.40	0.41-0.28	0.66-0.36	0.32-0.23	0.27-0.27
	HN area vs C1–C3	0.70-0.50	1.14-0.64	0.47-0.51	0.77-0.68	0.32-0.29	1.04-0.86
	HN area vs C4–C6	0.65-0.57	0.69-0.77	0.50-0.46	0.54-0.50	0.60-0.50	0.88-0.59
	Skull vs Mandible	0.33-0.26	1.04-0.56	0.49-0.44	0.83-0.53	0.32-0.26	0.30-0.31
	Skull vs C1–C3	0.69-0.50	1.25-0.66	0.53-0.59	0.89-0.80	0.36-0.32	1.06-0.87
	Skull vs C4–C6	0.63-0.57	0.85-0.81	0.52-0.56	0.61-0.58	0.63-0.54	0.89-0.59
	Mandible vs C1–C3	0.77-0.56	1.30-0.82	0.68-0.57	0.92-0.76	0.50-0.37	1.07-0.91
	Mandible vs C4–C6	0.69-0.65	0.98-1.01	0.70-0.49	0.82-0.56	0.71-0.55	0.90-0.64
	C1–C3 vs C4–C6	0.42-0.53	0.59-0.49	0.45-0.47	0.62-0.59	0.49-0.57	0.66-0.66

Abbreviations: LR = left–right; AP = anterior–posterior; CC = cranial–caudal; SHS = standard head support; IHS = individual head support.

Chapter 6

A comparison of dose-response models for the parotid gland in a large group of head-and-neck cancer patients

Abstract

Purpose: The dose-response relationship of the parotid gland has been described most frequently using the Lyman-Kutcher-Burman model. However, various other normal tissue complication probability (NTCP) models exist. We evaluated in a large group of patients the value of six NTCP models that describe the parotid gland dose response 1 year after radiotherapy.

Materials and Methods: A total of 347 patients with head-and-neck tumours were included in this prospective parotid gland dose-response study. The patients were treated with either conventional radiotherapy or intensity-modulated radiotherapy. Dose-volume histograms for the parotid glands were derived from three-dimensional dose calculations using computed tomography scans. Stimulated salivary flow rates were measured before and 1 year after radiotherapy. A threshold of 25% of the pre-treatment flow rate was used to define a complication. The evaluated models included the Lyman-Kutcher-Burman model, the mean dose model, the relative seriality model, the critical volume model, the parallel functional subunit model, and the dose-threshold model. The goodness of fit (GOF) was determined by the deviance and a Monte Carlo hypothesis test. Ranking of the models was based on Akaike's information criterion (AIC).

Results: None of the models was rejected based on the evaluation of the GOF. The mean dose model was ranked as the best model based on the AIC. The TD_{50} in these models was approximately 39 Gy.

Conclusions: The mean dose model was preferred for describing the dose-response relationship of the parotid gland.

Chapter 6

6.1 Introduction

Radiation-induced salivary dysfunction is a serious adverse effect of radiotherapy (RT) in head-and-neck cancer patients. The reduction in salivary flow causes problems in eating, speaking, and swallowing [5], and results in a decreased quality of life [9]. In the last few years, intensity-modulated RT (IMRT) has been used increasingly in head-and-neck cancer patients. With IMRT, more concave dose distributions can be realized, which is beneficial for sparing the parotid glands.

Several studies have been performed to describe the normal tissue complication probability (NTCP) of the parotid gland after RT [10, 23–28]. The Lyman-Kutcher-Burman (LKB) model is applied most frequently, especially with the mean dose to the parotid gland as the predictive parameter [23, 24]. However, the dose response of the parotid gland has not been described satisfactorily using the LKB model, because unexpected complications are frequently seen. Various other NTCP models exist that describe the relationship between the dose distribution and the response. Some attempts have been made to validate these models, but these studies contain generally too few clinical data [23–28]. We combined the parotid gland data of the University Medical Center Utrecht and the University of Michigan Hospital to generate the largest published dataset of objectively measured parotid gland complications (384 parotid glands). It contains a wide range of dose distributions to the parotid glands, which might make it possible to validate these models.

Modeling the dose response of the parotid gland 1 year after RT in this patient group is performed using phenomenologic models (the LKB model [23, 24, 30, 31, 108, 109], the mean dose model [23, 24, 30, 31, 108, 109], and the relative seriality or Källman s-model [110, 111]), functional subunit (FSU) based models (the critical volume model [112–114], and the parallel FSU model [115, 116]), and a dose-threshold model (the V_{Dth} model [114]). The goal of this study is to find out which of these models best describes the dose response of the parotid gland 1 year after RT.

6.2 Materials and Methods

6.2.1 Patients and radiotherapy treatment

All analysed patients were previously included in published datasets described by Dijkema *et al.* [28] and Li *et al.* [27]. In summary, 221 patients treated with either conventional RT (CRT), mainly opposed lateral beams or inverse planned IMRT, were included in the University Medical Center Utrecht. The 126 patients included in the University of Michigan Hospital were treated using forward planned, inverse planned, and beamlet IMRT. Patients with at least one parotid gland with successful salivary flow collection before and at 1 year after treatment were analysed. After 1 year, 227 parotid glands from the University Medical Center Utrecht (130 patients) and 157 parotid glands from

the University of Michigan Hospital (92 patients) were available for analysis. The excluded patients (91 in University Medical Center Utrecht, 34 in University of Michigan Hospital) had no complete salivary flow measurement before RT and at 1 year after RT because of missed appointments and unsuccessful salivary flow collection of both parotid glands. The discarded parotid glands of the analysed patients (33 in University Medical Center Utrecht, 27 in University of Michigan Hospital) had no successful salivary flow collection before RT and at 1 year after RT.

6.2.2 Parotid gland delineation and dose-volume histogram calculation

For each patient, the left and right parotid glands were delineated on a contrast-enhanced computed tomography (CT) scan by a radiation oncologist. Three-dimensional dose distributions were calculated and separate dose-volume histograms (DVHs) were generated for the left and right parotid glands. This enabled the analysis of each gland separately.

6.2.3 Complication measurement

Saliva collection

In both institutes, stimulated parotid saliva production was measured similarly before and 1 year after RT for both parotid glands simultaneously using Lashley cups [23, 24]. Stimulation of salivary flow was achieved by applying a few drops of a 2-5% citric acid solution to the mobile part of the tongue during saliva collection. Samples were collected for 2 minutes after a 2 minute waiting time in the University of Michigan Hospital and for 10 minutes in the University Medical Center Utrecht. Flow rates, expressed in millilitre per minute (mL/min), were calculated assuming the specific density of parotid saliva to be 1 g/mL. No oral stimulus was permitted for at least 60 minutes before saliva collection. To test if the differences in saliva collection methods resulted in differences in the flow ratio, a linear regression analysis was performed on the flow ratio versus the mean dose of the parotid gland of both institutes separately using the statistical software package *R* [117]. To compare the linear regression of both datasets, an F-test was performed using the sum of squares of the regression analysis [118].

End point determination

For each individual parotid gland, a complication was defined as a reduction in salivary flow to below 25% of the pre-treatment flow. A complication resulted in an end point with value 1.

Salivary flow measurements and therefore complication rates are known to have relatively large uncertainties [11]. However, it is difficult to determine the amount of noise in the data and the impact of this on the results. To assess the effect of these uncertainties on the model ranking, secondary end points were derived from the salivary flow

data and were evaluated similarly as the original end points. Assuming independent saliva production of both parotid glands [11], the secondary end points were determined by dividing the salivary flow at 1 year by the salivary flow of the parotid gland on the other side before RT.

6.2.4 Influence of fraction size

In the biological effective dose (BED), the influence of the fraction size of the dose delivered to the parotid gland is taken into account. Because the dose distribution in either CRT or IMRT varies, it is reasonable to determine whether the physical dose or the BED has to be used to model the dose-response relationship of the parotid gland. For the patients treated in the University Medical Center Utrecht (227 parotid glands), the physical dose DVHs were converted into BED DVHs using the LQ model [119]:

$$BED = D\left(1 + \frac{d}{\alpha/\beta}\right) \tag{6.1}$$

The parameter D is the total dose at each dose bin, d is the total fraction dose at each dose bin, and α/β is the ratio used in the LQ model to quantify the fractionation sensitivity of organs [119]. Different fraction sizes during treatment were taken into account. The α/β ratio of the human parotid gland has not yet been determined accurately; however, values between 3 Gy [120] and 10 Gy [121] have been suggested. Therefore, α/β ratios of 3 Gy and 10 Gy were used for analysis.

The most frequently used model (mean dose model) was fitted to the physical dose DVHs and the BED DVHs of the CRT and the IMRT groups, separately. The goodness of fit for this model using either the BED or the physical dose was compared.

6.2.5 NTCP models

Modeling the dose response of the parotid gland was performed using six NTCP models. These NTCP models were phenomenologic models (the LKB model, the mean dose model, and the relative seriality or Källman s-model), FSU based models (the critical volume model and the parallel FSU model), and a dose-threshold model (the V$_{Dth}$ model). The equations of the models can be found in Appendix 2.A.

The LKB model [23, 24, 30, 31, 108, 109] is the most frequently used NTCP model for parotid gland data. The effective dose (D_{eff}) method for DVH reduction as proposed by Mohan *et al.* [31] was used. Parameter n in this model describes the volume effect of the organ. The LKB model is often used as a mean dose model, by fixing n to 1. This model was treated in this study as a separate model (the mean dose model). In the relative seriality or Källman s-model [110, 111], the organ is divided in a number of subunits. The seriality parameter s describes the organization of the subunits. A single

subunit corresponds to a serial organ, whereas a parallel organ is constructed of multiple subunits. The parameter s in this model is inversely proportional to n in the LKB model.

In the critical volume model [112–114], an organ is divided into FSUs. These FSUs are identical structures that function independently. A complication occurs if a critical number of FSUs is destroyed. The parallel FSU model [115, 116] can be considered as a simple version of the critical volume model.

In the V_{Dth} model [114], the predictive dose-response parameter is the relative volume that received a higher dose than a given threshold dose.

6.2.6 Model fitting and statistical analysis

The maximum likelihood method [122] was used to fit the NTCP models to the data:

$$L = \prod_{i=1}^{N} L_i = \prod_{i=1}^{N} p_i^{ep_i} \left(1 - p_i\right)^{[1-ep_i]} \tag{6.2}$$

This method determines the values of the model parameters for which the likelihood (L) is maximum. This means that the maximum value of L defines the maximal agreement between the observed end points (ep_i) and the calculated NTCP values (p_i) [25]. The parameter N is the number of data points. Mathematically, it is easier to maximize the natural logarithm of the likelihood (LL):

$$LL = \ln(L) = \sum_{i=1}^{N} \left(ep_i \ln\left(p_i\right) + \left(1 - ep_i\right)\ln\left(1 - p_i\right)\right) \tag{6.3}$$

The confidence intervals (CI) of the model parameters were determined by calculating the individual parameter probability distribution (PD), which was followed by obtaining the 95% LL contour using a central interval requirement. This method equalizes the integrated PDs below and above the CI [25].

The goodness of fit (GOF) was determined using the deviance (Δ_{LL}) [122].

$$\Delta_{LL} = -2\left(LL_c - LL_f\right) \tag{6.4}$$

The parameter LL_c is the natural logarithm of the likelihood of the actual fitted (current) model and LL_f is the natural logarithm of the likelihood of the experimental data (full model).

The Δ_{LL}, however, cannot be used to determine significant differences between models or to test whether a model describes the data properly. Therefore, a Monte Carlo hypothesis test was applied. The probability of finding a worse fit was determined from

1000 artificial datasets [113]. For each DVH in the original dataset, the NTCP value was calculated using the fitted model. Subsequently, a Monte Carlo procedure generated a random number between 0 and 1. If the random number was larger than the NTCP value, no complication was defined, and if the random number was smaller than the NTCP value, a complication was defined. The percentage of fits to the artificial datasets with a higher Δ_{LL} than the fit to the original dataset is interpreted as the GOF, where the criterion for model acceptance was 5%.

The ability of a model to correctly determine the end point of a subject can furthermore be tested using a receiver operating characteristic (ROC) curve. The area under the curve was used to measure the discriminating ability of the model [123, 124].

To rank the accepted models, the number of model parameters was taken into account using the second order Akaike's information criterion (AIC) [125]:

$$AIC = -2LL_c + 2k + \frac{2k(k+1)}{n-k-1} \tag{6.5}$$

The parameter k is the number of parameters and n is the number of parotid glands.

6.3 Results

6.3.1 Saliva collection

The differences in saliva collection method resulted in comparable coefficients with overlapping confidence intervals. No significant difference in the regression analysis between the institutes was found ($p = 0.2$). Therefore, the data of both institutes could be combined and analysed as one group.

6.3.2 Influence of the fraction size

The values of the model parameters TD_{50} and m of the mean dose model for the physical dose DVHs and the BED DVHs of the CRT and IMRT groups were comparable and the confidence intervals were overlapping (Table 6.1, Figure 6.1). The GOF, indicated by the Δ_{LL} and the AIC, did not show a significant difference between the physical dose and the BED modeling (Table 6.1).

The differences between the CRT and IMRT group were not significant [28], and a benefit of using the BED with an α/β ratio of either 3 Gy or 10 Gy instead of the physical dose could not be found. Based on these results, the NTCP modeling in this study was performed using the physical dose DVHs.

Table 6.1: NTCP modeling using the physical dose and the biological effective dose

	TD_{50}	95% CI	m	95% CI	Δ_{LL}	AIC
Dose						
CRT	40.1	36.0 - 45.8	0.47	0.36 - 0.68	225.61*	229.66*
IMRT	38.4	33.3 - 44.3	0.33	0.24 - 0.74		
BED (α/β=3 Gy)						
CRT	62.1	55.5 - 70.8	0.49	0.38 - 0.72	225.34*	229.39*
IMRT	57.6	49.0 - 71.8	0.41	0.30 - 0.86		
BED (α/β=10 Gy)						
CRT	46.9	41.8 - 53.5	0.47	0.36 - 0.70	225.34*	229.39*
IMRT	44.1	38.0 - 55.5	0.37	0.26 - 0.76		

Abbreviations: BED = biological effective dose; CRT = conventional radiotherapy; IMRT = intensity-modulated radiotherapy; TD_{50} = the dose to the whole organ resulting in 50% complication probability; CI = confidence interval; m = slope of the curve; Δ_{LL} = deviance; AIC = Akaike's information criterion.

* The Δ_{LL} and AIC were calculated from the CRT and IMRT patients together.

6.3.3 NTCP models

Based on the GOF assessed by the Monte Carlo method, none of the NTCP models could be rejected (Table 6.2), because they all largely exceeded the 5% threshold.

The model parameters TD_{50} and m appear in four of the six used NTCP models. The fitted value of TD_{50} ranged from 37 Gy (parallel FSU model) to 39.88 Gy (mean dose model). The fitted values of m ranged from 0.35 (parallel FSU model) to 0.48 (V_{Dth} model) (Table 6.2). The values of parameters n in the LKB model, s in the relative seriality model and λ in the critical volume model predicted a parallel architecture of the parotid gland.

The discriminating ability of the models, as assessed by the area under the ROC curve, was comparable (Table 6.3, Figure 6.2).

The AIC showed a highest ranking of the mean dose model (Table 6.3). The secondary end points did not change the ranking of the models.

6.4 Discussion

Six NTCP models were used to describe the dose-response relationship of the parotid gland. The TD_{50} found in these models was approximately 39 Gy, which corresponded to the values reported by Roesink *et al.* [23] and Dijkema *et al.* [28]. We found no evidence of a threshold dose at 26 Gy as described by Eisbruch *et al.* [24], even though the

Table 6.2: Model parameters and goodness of fit values of the models

Model	Parameter	Value	95% CI	Δ_{LL}	Monte Carlo
LKB	n	1.13	0.75 - 14.25	340.63	0.51
	TD_{50}	39.4	33.8 - 41.8		
	m	0.42	0.36 - 0.58		
Mean dose	TD_{50}	39.9	37.3 - 42.8	339.19	0.59
	m	0.40	0.34 - 0.51		
Relative seriality	s	0.08	0.00 - 0.65	342.56	0.71
	TD_{50}	38.8	36.5 - 43.5		
	γ	0.95	0.70 - 1.30		
Critical volume	α	0.03	0.06 - 0.20	357.73	0.66
	N_0	1	2 - 32		
	λ	0.65	0.60 - 0.90		
	N_{FSU}	219	18 - 298		
Parallel FSU	D_{50}	32.5	15.0 - 95.0	336.44	0.55
	k	2.75	0.50 - 4.50		
	TD_{50}	37.0	32.0 - 44.0		
	m	0.35	0.30 - 0.60		
V_{Dth}	D_{th}	30.5	25.0 - 37.0	342.98	0.58
	rdV_{50}	0.68	0.60 - 0.80		
	m	0.48	0.35 - 0.65		

Abbreviations: CI = confidence interval; Δ_{LL} = deviance; LKB = Lyman-Kutcher-Burman; FSU = functional subunit.

Table 6.3: Model ranking based on the AIC

Model	Δ_{LL}	AIC	ROC
Mean dose	339.19	343.22	0.864
Parallel FSU	336.44	344.55	0.867
LKB	340.63	346.70	0.864
Relative seriality	342.56	348.63	0.864
V_{Dth}	342.98	349.04	0.864
Critical volume	357.73	365.83	0.862

Abbreviations: AIC = Akaike's information criterion; Δ_{LL} = deviance; ROC = area under the receiver operating characteristic curve; FSU = functional subunit; LKB = Lyman-Kutcher-Burman.
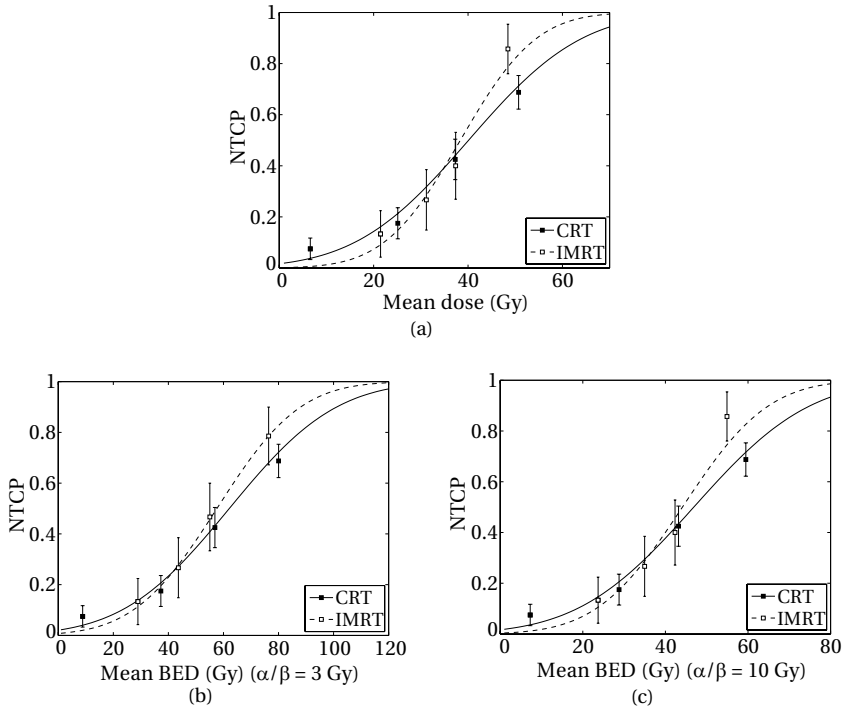
Figure 6.1: The NTCP curves of the mean dose model of the physical dose (a) and the biological effective dose (BED; b and c). The NTCP curves are constructed using the model parameters in Table 6.1; the observed complications are binned in four bins of equal patient number based on the mean dose. The error bar is the standard error of the mean of each complication bin.

same patients were included in this study. The data published by Eisbruch *et al.* contained relatively few data points in the critical 30-40 Gy range. In our study, the total dose range of the NTCP curve was equally covered with data (Figure 6.3), which made the analysis more reliable.

The mean dose model, or the LKB model with parameter *n* fixed to 1, is the most commonly used NTCP model for modeling the parotid gland dose-response relationship [23, 24, 28, 109]. Yet, using this model, unexplained complications were often seen. The hypothesis was that fewer unexplained complications were observed using other NTCP models. However, none of the investigated models described the dose-response relationship of the parotid gland significantly better than the mean dose model.
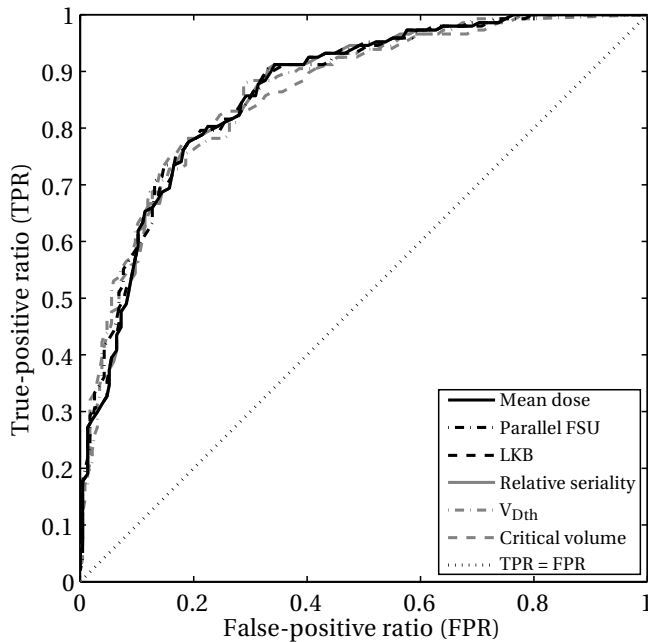
Figure 6.2: The receiver operating characteristic (ROC) curves of the models. The line TPR = FPR is the ROC curve of a theoretical model where the true-positive ratio (TPR) equals the false-positive ratio (FPR). For each model, the area under the curve can be found in Table 6.3.

The amount of clinical data in previous published parotid gland studies [10, 23–28] was generally rather low, which might made it impossible to distinguish between different NTCP models. The large number of patients in this study enabled the comparison of several frequently used NTCP models for the characterization of the dose-response relationship of the parotid gland. The dataset used in this study was the largest set of parotid gland response data known. Furthermore, the complete range of the NTCP curve was covered with clinical data (Figure 6.3) and a large variation of DVH shapes was used.

The large number of parotid glands also enabled an accurate comparison of the physical dose and the BED. The influence of the fraction size per DVH bin on the complications was taken into account using the BED. Because the α/β ratio for the human parotid gland has not been determined, the applied values are based on published suggestions or values for rat parotid glands. The applied values of 3 Gy and 10 Gy were the boundaries of these published α/β ratio values. A low α/β ratio results in a high sensi-

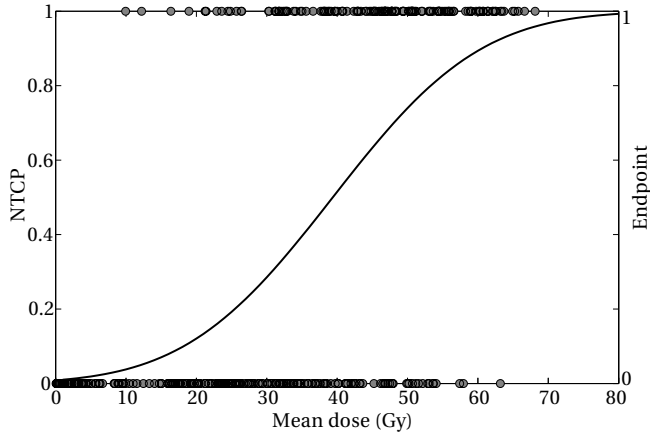**Figure 6.3:** The normal tissue complication probability as predicted by the mean dose model, constructed using the parameters in Table 6.2. The clinical end points are plotted as dots.

tivity to fraction dose, and therefore to a large influence of the BED in NTCP modeling. Furthermore, the difference in fraction size between the CRT and IMRT patients is expected to be the largest. However, the NTCP curves of these patients were comparable, even with a low α/β ratio, which was the first indication that the influence of fraction dose was negligible. The AIC values of the mean dose model using the physical dose and the BED were comparable and the 95% CI were overlapping. Because no evidence was found that the BED described the dose response better, the physical dose was used in fitting the models.

Observation of the ROC curves of the models did not show a difference among the models. The area under the curve, which can be thought of as the percentage of correctly classified patients, was higher than 0.8 for all models. A high percentage (> 0.7) accounts for a good discriminating ability of the model. The GOF, as measured by the Monte Carlo method, was acceptable for all models. Together with the ROC curves, this indicated that all models are accurate enough to describe this dataset [124]. However, the number of model parameters is not taken into account using the ROC curve or the GOF. Therefore, the AIC was used for ranking the models.

The mean dose model, for which the LKB model with parameter n fixed to 1 was used, was found to be the best fitting model based on the AIC. The fitted value of n in the LKB model was 1.13. This value was comparable to the value found by Schilstra *et al.* ($n = 1.3$) [25] and resulted in a model close to the mean dose model. The second best fitting model based on the AIC was the parallel FSU model. This model had the lowest Δ_{LL} and the largest area under the ROC curve. However, because the parallel FSU

model had four parameters, this model was ranked as the second best model based on the AIC. The parallel FSU model predicted a parallel architecture of the parotid gland, which was also predicted by the LKB model ($n \approx 1$), the seriality model ($s << 1$) and the critical volume model ($\lambda \neq 1$). The CI of parameter n in the LKB model and of parameter s in the relative seriality model was rather large. This CI could be decreased by using $u = e^{-n}$ as a substitute for n and $u = e^{-s}$ as a substitute for s. The Δ_{LL} of the LKB model was also lower using the substitute, because u could be determined more precisely than n. However, this resulted in corresponding values for the model parameters n and s and no differences in ranking of the models. The slope of the sigmoid curve was comparable in all models ($m \approx 0.40$) and the value of TD_{50} was about 39 Gy in all models. These results were in correspondence with the results presented by Blanco *et al.* [26], who found a mean dose model and a parallel model to be the best fitting models for parotid gland data.

The determination of a complication was based on salivary flow measurements using Lashley cups [23]. These measurements are known to have large standard deviations [11]. The large standard deviation made it difficult to distinguish between different models, because the data can be easily over-interpreted. To avoid over-interpretation of the data, the uncertainty in salivary flow was modeled by constructing secondary end points. The salivary flow of the left and right parotid gland before RT was interchanged, because it can be assumed that these were comparable [11]. Modeling of the secondary end points resulted in the same ranking of the models, which indicated an acceptable standard deviation.

The influence of different saliva collection times of the University Medical Center Utrecht (10 minutes) and the University of Michigan Hospital (2 minutes) was reduced by the fact that the flow ratio was used. The flow ratio was expressed in mL/min, which is independent of collection time. During the first 2 minutes of stimulation, no samples were collected at the University of Michigan Hospital, which reduced the influence of the latency. Another difference between the institutes was the cups used. In the University of Michigan Hospital, Carlson-Crittenden cups were used. The difference between these cups and the Lashley cups used in the University Medical Center Utrecht are, in our opinion however, negligible. Furthermore, comparing the linear regression of the data of both institutes showed no significant difference.

The mean dose model used in this study is based on the LKB model. A more simple version of a mean dose model-for example, one as published by Blanco *et al.* [26]- might describe the data comparable. Even a simple logistic regression with the mean dose as a predictive parameter might be satisfactory, which would make the use of a DVH as dose input unnecessary. On the other hand, all investigated models used the DVH as dose input; hence, no information about the location of the high- or low-dose area in the parotid gland was available. Potential regional differences in sensitivity in the parotid gland might explain the unexpected complications better [126]. NTCP models based on the three-dimensional dose distribution, such as cluster models [127], would

possibly describe the dose response of the parotid gland more appropriately. Yet, such models are not widely available. To have an acceptable fit using such models, different three-dimensional dose distributions should be used. However, the variation in direction of the dose gradient is similar in all patients, which reduces the variation in dose distributions. Nevertheless, we do not exclude that in our dataset, a three-dimensional based model would describe the data better.

6.5   Conclusion

Even in this large set of clinical dose response data of the parotid gland, no significant difference between commonly used NTCP models could be found. The models indicated a parallel architecture of the parotid gland and a TD_{50} of 39 Gy. The mean dose model, the most simple model used, was ranked as the best model.

Appendix 6.A   Model equations

The normal tissue complication probability (NTCP) models assume a sigmoid relationship between NTCP and dose. This relationship can be expressed by the cumulative normal distribution:

$$NTCP = \frac{1}{\sqrt{2\pi}} \int_{-\infty}^{t} e^{\left[\frac{-x^2}{2}\right]} dx \tag{A.1}$$

The expression of parameter t is model dependent.

Lyman-Kutcher-Burman model

The Lyman-Kutcher-Burman (LKB) model [23, 30, 31, 108, 109] can be expressed by the following Lyman equation for parameter t (Eq. A.1):

$$t = \frac{D - TD_{50}(v)}{m \cdot TD_{50}(v)} \tag{A.2}$$

In Eq. A.2, D is the dose to the volume fraction v ($v = V/V_{total}$). $TD_{50}(v)$ is the dose resulting in a 50% complication probability for uniform irradiation of volume fraction v. Parameter m describes the slope of the NTCP curve at TD_{50}.

The LKB model assumes a power-law relation between the tolerance dose and the irradiated volume fraction:

$$TD_{50}(v) = TD_{50}(1) \cdot v^{-n} \tag{A.3}$$

Parameter $TD_{50}(1)$ in Eq. A.3 represents the TD_{50} for a uniform irradiated organ. Parameter n describes the volume effect of the organ.

In order to handle non-uniform dose distributions, a histogram reduction algorithm, as described by Kutcher and Burman, must be applied to the DVH [31]:

$$D_{eff} = \left(\sum_{i} v_i D_i^{\frac{1}{n}} \right)^{n} \tag{A.4}$$

Parameter D_{eff} is the uniform dose that leads to the same NTCP as the actual non-uniform dose given. Parameter D in Eq. A.2 is substituted with D_{eff} to handle non-uniform dose distributions [31, 108, 109].

Parameter n (Eq. A.3 and A.4) describes the volume effect of the organ and is usually restricted between 0 and 1. Small values of n ($n \ll 1$) represent the maximum dose to be of most influence on D_{eff}. If n is 1, D_{eff} equals the mean dose of the organ, and even if n reaches infinity, D_{eff} will be close to the mean dose [108].

Mean dose model

The value of parameter n in Eq. A.3 and A.4 in the LKB model is fixed to 1. Thereby, the D_{eff} in Eq. A.4 will equal the mean dose to the parotid gland:

$$D_{mean} = \sum_i v_i D_i \tag{A.5}$$

Relative seriality model

The relative seriality or Källman s-model [110, 111] is expressed by a Poisson distribution instead of the cumulative normal distribution of Eq. A.1:

$$NTCP = \left(1 - \prod_i \left(1 - P(D_i)^s\right)^{v_i}\right)^{\frac{1}{s}} \tag{A.6}$$

$$P(D) = 2^{-e\left[e \cdot \gamma \cdot \left(1 - \frac{D}{TD_{50}}\right)\right]} \tag{A.7}$$

Parameter s in Eq. A.6 represents the 'relative seriality' of an organ. If s is small ($s \ll 1$), the model describes a parallel organ; if $s = 1$, the model describes a serial architecture of the organ. D_i and v_i in Eq. A.6 are the fractional dose and the volume fraction, respectively. Parameter γ in Eq. A.7 corresponds to the dose-response gradient and TD_{50} is the dose resulting in a 50% complication probability.

Critical volume model

Parameter t of Eq. A.1 in the critical volume model [112–114] can be expressed as follows:

$$t = \sqrt{N_{FSU}} \cdot \frac{\mu - \lambda}{\sigma} \tag{A.8}$$

Parameter N_{FSU} in Eq. A.8 is the number of functional subunits (FSUs) in an organ and λ represents the functional reserve. If the fraction of destroyed FSUs is smaller than λ, no complication occurs. Parameters μ and σ can be expressed by the following equations:

$$\mu = \sum_i P_{FSUi} \cdot v_i \tag{A.9}$$

$$\sigma = \sqrt{\sum_i P_{FSUi} \cdot (1 - P_{FSUi})} \tag{A.10}$$

In Eq. A.9, v_i is the volume fraction and P_{FSUi}, the probability of killing one FSU, in both Eq. A.9 and A.10, is given by a single-hit model:

$$P_{FSUi} = \left(1 - e^{[-\alpha \cdot D_i]}\right)^{N_0} \tag{A.11}$$

D_i is the fractional dose, α represents the radio-sensitivity of the cells and N_0 is the number of clonogenic cells per FSU.

Parallel FSU model

The expression for parameter t (in Eq. A.1) in the parallel FSU model [115, 116] can be described as:

$$t = \frac{EUD - TD_{50}}{m \cdot TD_{50}} \tag{A.12}$$

$$EUD = D_{50} \cdot \left(\left(\sum_i \frac{v_i}{1 + \left(\frac{D_{50}}{D_i}\right)^k} \right)^{-1} - 1 \right)^{-\frac{1}{k}} \tag{A.13}$$

D_{50} is the local dose resulting in 50% local complication probability, and k is the local steepness parameter. TD_{50} is the dose to the whole organ resulting in 50% complication probability, and m is the slope of the NTCP curve [114]. Parameters D_i and v_i in Eq. A.13 are the fractional dose and volume of one FSU respectively.

V$_{Dth}$ model

The V$_{Dth}$ model [114] is a special case of the parallel FSU model and describes the relationship between the relative damaged volume and the complication. When $k \to \infty$ in Eq. A.13, parameter t (Eq. A.1) can be expressed as follows:

$$t = \frac{rdV - rdV_{50}}{m \cdot rdV_{50}} \tag{A.14}$$

$$rdV = \sum_i v_i \qquad \text{for all } v_i \text{ for which } D_i > D_{th} \tag{A.15}$$

The parameter rdV in Eq. A.14 is the relative damaged volume, rdV_{50} is the relative damaged volume that leads to a complication probability of 50%, and m is the slope of the NTCP curve, which is a volume-response curve in this model. Parameters D_i and v_i in Eq. A.15 are the fractional dose and volume respectively, and D_{th} is the threshold dose.

Chapter 7

Summary and general discussion

Aspects of all stages in the radiotherapy treatment of head-and-neck (HN) cancer patients were addressed in this thesis. The topics follow the same path as the patient during the treatment: from imaging, tumour delineation, and treatment planning, through daily irradiation, to unfortunately in some cases radiation-induced xerostomia. Xerostomia, the subjective feeling of a dry mouth, is one of the main side effects of radiotherapy in the HN area, caused by radiation damage to the salivary glands [5, 6]. Patients with severe xerostomia experience a large deterioration of their quality of life. Recent studies confirmed the possible reduction of the dose to the parotid gland using IMRT and thereby a decrease in complication rate compared to conventional radiotherapy [71]. However, patient-reported xerostomia was still prevalent at the long term in patients treated with IMRT [9]. This supports the hypothesis that damage to the other salivary glands contributes to patient-reported xerostomia. After the parotid glands, the submandibular glands are the largest salivary glands, both in terms of gland volume and salivary output. Therefore, the research presented in this thesis considers radiation-induced damage to both the parotid and the submandibular glands.

7.1 Imaging of head-and-neck cancer patients

Dynamic contrast-enhanced MRI (DCE-MRI) is an imaging technique which visualizes the perfusion of tissues by dynamically imaging of the uptake of a contrast agent. Several other groups have related the blood perfusion of HN tumours to the radiation-sensitivity of the tumour, and thereby, to the effectiveness of the treatment [49, 68]. A quantitative analysis of DCE-MRI data, by fitting of a tracer kinetic model, is often performed in such studies. The perfusion parameters following from such an analysis can be compared among patients or be used in treatment-response imaging.

DCE-MRI, especially on a 3.0 T system, is rather new in the HN area, and the feasibility of quantitative DCE-MRI in oropharyngeal cancer patients was addressed in chapter 2. All difficulties associated with DCE-MRI at a higher magnetic field strength were solved and consistent patient-specific arterial input functions and perfusion parameter maps were acquired for all patients. In dynamic imaging of the HN area, movements due to

swallowing and breathing are a major issue. However, the results in this chapter have shown that rigid registration of the tumour area was not affecting the perfusion parameters obtained in oropharyngeal tumours. It should be mentioned here that these results might not be applicable to other HN tumour sides. The larynx, for example, experiences larger displacements due to swallowing and registration might be influencing the perfusion parameters here.

The perfusion parameters in the gross tumour volume (GTV) were significantly increased, compared to the perfusion in a part of healthy tissue. This elevated perfusion in the GTV might reveal more insight in the characterisation or radiation-sensitivity of the tumour. However, actual characterisation of the tissue using quantitative DCE-MRI requires separate studies to compare pathology to imaging. This was performed only once for oropharyngeal cancer patient by Konouchi *et al.* [128] on a small group of patients using a qualitative analysis of the DCE-MRI data.

The perfusion parameter maps showed inhomogeneities within the GTV. These inhomogeneities can be used to guide dose painting within the GTV. Especially in the larger tumours, there is room for improvement in terms of the tumour control. In a retrospective analysis of oropharyngeal cancer patients treated at our institute, about 60% of the recurrences were seen in patients with a large tumour (T-stage > T3). Secondly, over 60% of the local recurrences were found in the high dose area, indicating the need to increase the dose to the GTV [129]. Quantitative DCE-MRI is a promising tool to guide dose painting within the GTV and the research described in chapter 2 opens up this possibility.

Due to the complexity of the HN anatomy, imaging of the healthy structures can also improve the radiotherapy treatment of HN cancer patients. To be able to adequately spare the salivary glands, appropriate imaging and delineation is required. Chapter 3 addresses the use of MRI to improve the delineation of the submandibular gland. Patients received a CT scan and an MRI exam including T_1- and T_2-weighted MRI scans and an MR sialography scan. MR sialography is a high-resolution heavily T_2-weighted MR sequence with fat suppression. The MR sialography images show the salivary gland volume with a medium-intense signal and the ductal structures as high-intensity branches. The use of MR sialography described in literature is restricted to visualizing salivary gland disorders as Sjögren's syndrome [82] or radiation-induced changes in the salivary glands [43]. The use of MR sialography for delineation of the salivary glands has not been described before.

To define the added value of MR sialography for submandibular gland delineation, the submandibular glands were delineated on only CT, on the combined CT and T_1- and T_2-weighted MRI scans and on all MR images. The results in chapter 3 showed a significant increase of the delineated submandibular gland volume in the MR-delineations compared to the other delineations. The difference was mainly observed in the cranial direction, resulting in a significant increase in the cranial-caudal extent of the submandibular gland on the MR sialography images. Including this cranial part of the subman-

dibular gland in the dose calculation will reduce the dose to the gland and sparing can be accomplished more adequately.

7.2   Radiotherapy for head-and-neck cancer patients

After a patient has undergone all imaging and the target volumes and organs at risk have been delineated, the radiotherapy treatment plan is made. IMRT enables us to adequately treat the tumour and lymph node areas and at the same time spare the organs at risk. For the parotid glands in oropharyngeal cancer patients this is indeed the case, but things become more complicated when one also tries to spare the submandibular glands.

The treatment margins cause complete overlap of the target volumes and the ipsilateral submandibular gland. The contralateral submandibular gland, on the other hand, is only partially overlapping with the elective lymph node areas. This makes it possible to reduce the dose to this gland by adapting the IMRT treatment planning. Only few groups have published on the feasibility of submandibular gland sparing radiotherapy [76, 77]. Saibishkumar *et al.* [77] even surgically transferred the submandibular gland to spare it more easily.

An advanced IMRT technique to spare both the parotid glands and the contralateral submandibular gland is presented in chapter 4. The mean dose to the submandibular gland reduced drastically with approximately 12 Gy to an average of 40 Gy when slight underdosage of the contralateral elective lymph node area was allowed. Reducing the margin from the clinically used 5 mm to a theoretically possible 2 mm reduced the mean dose to the submandibular gland even further. Based on the very few dose-response studies of the submandibular gland available, a mean dose of 40 Gy will give a chance of about 50% to develop a complication [75].

The main question here is if it is clinically justified to slightly underdose a small part of the contralateral elective lymph node area. Jensen *et al.* [89] showed in selected patients that only ipsilateral treatment of the lymph node area resulted in the same loco-regional control as bilateral treatment of this area. In this light, a slight reduction of the dose to the elective target area to spare the submandibular gland is justified. It should also be noted here that treating the contralateral lymph node area is not the standard treatment in all institutes.

From 2009 on, oropharyngeal cancer patients with a nodal stage up to N2b are treated with contralateral submandibular gland sparing IMRT at our institute. All patients receive questionnaires about their quality of life, salivary flow measurements, and MR imaging of the salivary glands. The salivary function, and more important, the tumour control in these patients will be compared to a group of patients treated with only parotid gland sparing radiotherapy. This will answer the question if submandibular gland

sparing IMRT is safe in terms of tumour control and if it reduces radiation-induced xerostomia.

The clinical justification of reducing the margin is more easy to accomplish. Treatment margins can be reduced by decreasing the uncertainty of patient positioning. This can be accomplished by daily imaging before the treatment fraction with for example conebeam CT (CBCT), which has been described by several other groups [103–105]. A lot of effort has been put into optimizing the registration of the CBCT images by these groups. Improving the immobilization of HN cancer patients by either changing the immobilization mask or the accompanying head support is a more structural way to reduce the uncertainty of the patient position. In chapter 5, an improved patient-specific head support was described, and compared to the standard head support.

To compare the head supports, the random and systematic displacements and deformations from day-to-day as well as during one treatment fraction were determined. Therefore, CBCT images were acquired before and after the fractions, which were registered to the planning CT. The use of the patient-specific head support significantly reduced both the displacements and deformations. Based on these results, the clinical treatment margin was decreased from 5 mm to 3 mm for the GTV. It should be mentioned that the displacements in the lower neck were still considerable with the patient-specific head support, and a reduction of the margin at this location was not justified. Improvements of the head support in the neck direction is possible, for example by extending the head support with a vacuum cushion. Such an additional neck support will probably reduce the deformations between the vertebrae even further and make it possible to also reduce the margin for the elective lymph node volumes in the neck.

With the CBCT method used in chapter 5, the bony anatomy can be visualized daily. However, movements due to swallowing or breathing occur within the soft-tissue and several times during one fraction. The recent development of an accelerator with integrated MRI functionality makes real-time soft-tissue visualization possible [130, 131]. Deformations within the soft-tissue, which are not addressed in chapter 5, can be visualized using such an MRI-accelerator. This would create the opportunity to reduce the margins even further, below 3 mm, which makes salivary gland sparing more easy to accomplish.

7.3   Prediction of salivary gland complications

The dose-response relationship of an organ can be described by a normal tissue complication probability (NTCP) model. Different NTCP curves have been published for the parotid gland over the last years [10, 23–28]. These curves are all based on rather small patient numbers, resulting in major differences between the curves [132]. In chapter 6, the NTCP of the parotid gland one year after radiotherapy was investigated

on the combined and updated data set of the University Medical Center Utrecht and the University of Michigan Hospital. This combined data set is the largest published parotid gland data set (n = 384 glands) upto now, resulting in the final NTCP curve for parotid gland complications one year after radiotherapy.

Several models have been designed to describe the NTCP of organs at risk. Chapter 6 handles the comparison of six widely used models to describe the NTCP of the parotid gland one year after radiotherapy. The salivary flow rate, measured using Lashley cups, was used as a measure of parotid gland complication. Dose-volume histograms were used as the dose input in these models. A large patient group is required to be able to fit the models accurately to the data and to distinguish between the models, which was accomplished by combining the data of the two institutes.

All models described in chapter 6 fitted the parotid gland data set acceptable and showed a good discriminating ability and the mean dose model was ranked as the best fitting model. The mean dose model relates the mean dose to an organ to the complication using two model parameters, the slope of the NTCP curve and the location of the 50% complication probability point. Due to its simplicity, the mean dose model is the most easy to use model, which is already quite often applied in clinic and in literature.

The NTCP curve resulting from the mean dose model described in chapter 6 can be interpreted as the definite curve for parotid gland complications one year after radiotherapy. The curve is corresponding nicely to the NTCP curve published previously by Roesink *et al.* [23]. From chapter 6 it can be concluded that the mean dose to the parotid gland resulting in 50% complications is 40 Gy.

A clear NTCP curve for the submandibular gland is still lacking. The clinical implementation of submandibular gland sparing IMRT will give the opportunity to perform a decent dose-response study of the submandibular gland. One should keep in mind that the data set for developing such a model should be large enough. This will probably require the combination of data sets of several institutes, as was done in chapter 6 for the parotid gland.

7.4   Understanding radiation-induced xerostomia

A promising approach to gain understanding of radiation-induced damage to the salivary glands is imaging. Different aspects of the salivary glands can be nicely visualized using MRI. Imaging of the salivary glands before and after radiotherapy will reveal more insight in the spatial radiation-induced changes in tissue characteristics and functionality. At our department, the MRI protocol described in section 1.5.1 is applied to oropharyngeal cancer patients before the radiotherapy treatment and at 6 weeks and 1 year after the end of the treatment. Due to the rather low number of newly diagnosed oropharyngeal cancer patients each year, the intake of patients in this study proceeds

slowly, with about 10 patients each year. Therefore, only very preliminary results of the early radiation-induced changes in the salivary glands can be discussed here.

At the early stage, oedema is prevalent in irradiated tissues [133]. The average T2 signal intensity in both the parotid and the submandibular glands was increased 6 weeks after radiotherapy, which is an indication of an increased water content such as found in oedema. A correlation was found between the mean dose to the gland and the increase in T2 signal intensity [134]. The MR sialography images also showed an increase in the signal intensity of the gland volume, resulting in a less clear contrast between the gland volume and the ductal structures.

The salivary glands are highly perfused organs and changes in this perfusion are very likely to occur after radiotherapy. From the first analysis, a significant increase in both the vascular plasma space (v_p) and the extra-vascular extra-cellular space (v_e) was observed. These observations are consistent with the results published by Juan *et al.* [17], who contributed these changes to a decreased vessel permeability and an increased extra-vascular extra-cellular space due to acinar cell loss. Their results are based on a qualitative analysis of DCE-MRI data of an irradiated and non-irradiated patient group, whereas our data is a quantitative analysis within the same patients, which will enable us to correlate the changes to the dose.

Correlating the changes visualized on MR to the 3D dose distribution will be difficult, but it opens up the possibility to develop NTCP models based on 3D MR imaging information. Besides correlation of the dose to these radiation-induced changes on MRI, a correlation with the salivary gland functionality is important. In the end, this will leads us to a better understanding and an adequate prediction of patient-reported xerostomia, which is the biggest challenge in the research on radiation-induced xerostomia.

In conclusion, this thesis has addressed aspects of all stages in the radiotherapy treatment of HN cancer patients and the severe side effects on the salivary glands which patients experience after their treatment. Due to the results described in this thesis, the clinical imaging and delineation was improved. All oropharyngeal cancer patients are now treated with submandibular gland sparing IMRT at our department and due to the improved patient immobilization and position verification, the margins were reduced. Finally, the definite dose-response curve for the parotid gland one year after radiotherapy has been determined. And although separately these adaptations in the treatment of HN cancer patients seem small, I believe that combined they make an important difference in preventing patient-reported xerostomia.

References

[1] The Netherlands Cancer Registry. Incidence of cancer in the netherlands 2007. *www.ikcnet.nl/cijfers*. May 19, 2010.

[2] Stein J, Mohan R, Wang X, *et al.* Number and orientations of beams in intersity-modulated radiation treatments. *Med. Phys.* 1997;24:149–159.

[3] Webb S. Contemporary IMRT - Developing physics and clinical implementation. 1st ed, 2005. *Institute of Physics Publishing, London, UK.*

[4] Kahn FM. The physics of radiation therapy. 4th ed, 2009. *Lippincott Williams and Wilkins, Philidelphia, PA, USA.*

[5] Cooper JS, Fu K, Marks J, Silverman S. Late effects of radiation therapy in the head and neck region. *Int. J. Radiat. Oncol. Biol. Phys.* 1995;31:1141–1164.

[6] Vissink A, Burlage FR, Spijkervet FKL, Veerman ECI, van Nieuw Amerongen A. Prevention and treatment of salivary gland hypofunction related to head and neck radiation therapy and chemotherapy. *Support Cancer Ther.* 2004;1:111–118.

[7] Mason DK, Chisholm DM. Salivary glands in health and disease. 1st ed, 1975. *W. B. Saunders Company, London, UK.*

[8] Bjordal K, de Graeff A, Fayers PM, *et al.* A 12 country field study of the EORTC QLQ-C30 (version 3.0) and the head and neck cancer specific module (EORTC QLQ-H&N35) in head and neck patients. EORTC Quality of Life Group. *Eur. J. Cancer* 2000;36:1796–1807.

[9] Braam PM, Roesink JM, Raaijmakers CPJ, Busschers WB, Terhaard CHJ. Quality of life and salivary output in patients with head-and-neck cancer five years after radiotherapy. *Radiat. Oncol.* 2007;2:3.

[10] Chao KSC, Deasy JO, Markman J, *et al.* A prospective study of salivary function sparing in patients with head-and-neck cancers receiving intensity-modulated or three-dimensional radiation therapy: initial results. *Int. J. Radiat. Oncol. Biol. Phys.* 2001;49:907–916.

[11] Burlage FR, Pijpe J, Coppes RP, *et al.* Variability of flow rate when collecting stimulated human parotid saliva. *Eur J Oral Sci* 2005;113:386–390.

[12] Konings A, Coppes R, Vissink A. On the mechanism of salivary gland radiosensitivity. *Int. J. Radiat. Oncol. Biol. Phys.* 2005;62:1187–1194.

[13] Konings A, Faber H, Cotteleer F, Vissink A, Coppes R. Secondary radiation damage as the main cause for unexpected volume effects: A histopathologic study of the parotid gland. *Int. J. Radiat. Oncol. Biol. Phys.* 2006;64:98–105.

[14] Jensen S, Pedersen A, Reibel J, Nauntofte B. Xerostomia and hypofunction of the salivary glands in cancer therapy. *Support Care Cancer* 2003;11:207–225.

[15] Feng J, van der Zwaag M, Stokman mA, van Os R, Coppes RP. Isolation and characterization of human salivary gland cells for stem cell transplantation to reduce radiation-induced hyposalivation. *Radiother. Oncol.* 2009;92:466–471.

[16] Astreinidou E, Roesink JM, Raaijmakers CPJ, *et al.* 3D MR sialography as a tool to investigate radiation-induced xerostomia: feasibility study. *Int. J. Radiat. Oncol. Biol. Phys.* 2007;68:1310–1319.

[17] Juan CJ, Chen CY, Jen YM, *et al.* Perfusion characteristics of late radiation injury of parotid glands: quantitative evaluation with dynamic contrast-enhanced MRI. *Eur. Radiol.* 2009;19:94–102.

References

[18] Coppes RP, Roffel AF, Zeilstra LJ, Vissink A, Konings AW. Early radiation effects on muscarinic receptor-induced secretory responsiveness of the parotid gland in the freely moving rat. *Radiat. Res.* 2000; 153:339–346.

[19] Stephens LC, Schultheiss TE, Price RE, Ang KK, Peters LJ. Radiation apoptosis of serous acinar cells of salivary and lacrimal glands. *Cancer* 1991;67:1539–1543.

[20] Makkonen TA, Nordman E. Estimation of long-term salivary gland damage induced by radiotherapy. *Acta Oncol.* 1987;26:307–312.

[21] Valdez I, Atkinson J, Ship J, Fox P. Major salivary gland function in patients with radiation-induced xerostomia: flow rates and sialochemistry. *Int. J. Radiat. Oncol. Biol. Phys.* 1993;25:41–47.

[22] Hannig M, Dounis E, Henning T, Apitz N, Stösser L. Does irradiation affect the protein composition of saliva? *Clin. Oral Invest.* 2006;10:61–65.

[23] Roesink JM, Moerland MA, Battermann JJ, Hordijk GJ, Terhaard CHJ. Quantitative dose-volume response analysis of changes in parotid gland function after radiotherapy in the head-and-neck region. *Int. J. Radiat. Oncol. Biol. Phys.* 2001;51:938–946.

[24] Eisbruch A, Ten Haken RK, Kim HM, Marsh LH, Ship JA. Dose, volume, and function relationships in parotid salivary glands following conformal and intensity-modulated radiation of head and neck cancer. *Int. J. Radiat. Oncol. Biol. Phys.* 1999;45:577–587.

[25] Schilstra C, Meertens H. Calculation of the uncertainty in complication probability for various dose-response models, applied to the parotid gland. *Int. J. Radiat. Oncol. Biol. Phys.* 2001;50:147–158.

[26] Blanco A, Chao K, El Naqa I, *et al.* Dose-volume modeling of salivary function in patients with head-and-neck cancer receiving radiotherapy. *Int. J. Radiat. Oncol. Biol. Phys.* 2005;62:1055–1069.

[27] Li Y, Taylor JMG, Haken RKT, Eisbruch A. The impact of dose on parotid salivary recovery in head and neck cancer patients treated with radiation therapy. *Int. J. Radiat. Oncol. Biol. Phys.* 2007;67:660–669.

[28] Dijkema T, Terhaard CHJ, Roesink JM, *et al.* Large cohort dose-volume response analysis of parotid gland function after radiotherapy: intensity-modulated versus conventional radiotherapy. *Int. J. Radiat. Oncol. Biol. Phys.* 2008;72:1101–1109.

[29] Roesink JM, Schipper M, Busschers W, Raaijmakers CPJ, Terhaard CH. A comparison of mean parotid gland dose with measures of parotid gland function after radiotherapy for head-and-neck cancer: implications for future trials. *Int. J. Radiat. Oncol. Biol. Phys.* 2005;63:1006–1009.

[30] Lyman JT. Complication probability as assessed from dose-volume histograms. *Radiat Res* 1985; 104:S13–19.

[31] Mohan R, Mageras GS, Baldwin B, *et al.* Clinically relevant optimization of 3-D conformal treatments. *Med. Phys.* 1992;19:933–944.

[32] Dijkema T, Raaijmakers CPJ, Ten Haken RK, *et al.* Parotid gland function after radiotherapy: The combined Michigan and Utrecht experience. *Int. J. Radiat. Oncol. Biol. Phys.* 2010;78:449–453.

[33] Chao KSC, Ozyigit G. Intensity modulated radiation therapy for head & neck cancer. 1st ed, 2003. *Lippincott Williams & Wilkins, Philidelphia, USA.*

[34] Van Asselen B, Raaijmakers CPJ, Hofman P, Lagendijk JJW. An improved breast irradiation technique using three-dimensional geometrical information and intensity modulation. *Radiother. Oncol.* 2001; 58:341–347.

[35] Wilbert J, Guckenberger M, Polat B, *et al.* Semi-robotic 6 degree of freedom positioning for intracranial high precision radiotherapy; first phantom and clinical results. *Radiat. Oncol.* 2010;5:42.

[36] Shah GV, Wesolowski JR, Ansari SA, Mukherji SK. New directions in head and neck imaging. *J. Surg. Oncol.* 2008;97:644–648.

[37] Verduijn GM, Bartels LW, Raaijmakers CP, Terhaard CH, Pameijer FA, van den Berg CA. Magnetic resonance imaging protocol optimization for delineation of gross tumor volume in hypopharyngeal and laryngeal tumors. *Int. J. Radiat. Oncol. Biol. Phys.* 2009;74:630–636.

[38] Emonts P, Bourgeois P, Lemort M, Flamen P. Functional imaging of head and neck cancers. *Curr. Opin. Oncol.* 2009;21:212–217.

[39] Haacke EM, Brown RW, Thompson MR, Venkatesan R. Magnetic resonance imaging - Physical principles and sequence design. 1st ed, 1999. *John Wiley & Sons, Inc.*

[40] Saito M, Umeda M, Fujiwara K, *et al.* Functional analysis of human parotid gland in vivo using the (1)H MRS MT effect. *NMR Biomed.* 2002;15:416–421.

[41] Dixon WT. Simple proton spectroscopic imaging. *Radiology* 1984;153:189–194.

[42] Glover GH. Multipoint Dixon technique for water and fat proton and susceptibility imaging. *J. Magn. Reson. Imaging* 1991;1:521–530.

[43] Wada A, Uchida N, Yokokawa M, Yoshizako T, Kitagaki H. Radiation-induced xerostomia: objective evaluation of salivary gland injury using MR sialography. *Am. J. Neuroradiol.* 2009;30:53–58.

[44] Kan T, Kodani K, Michimoto K, Fujii S, Ogawa T. Radiation-induced damage to microstructure of parotid gland: Evaluation using high-resolution magnetic resonance imaging. *Int. J. Radiat. Oncol. Biol. Phys.* 2010;77:1030–1038.

[45] Astreinidou E, Lagendijk JW, Raaijmakers CPJ, Roesink J, Terhaard CHJ, Bartels WL. 3D MR sialography protocol for post-radiotherapy follow up of the salivary duct system. *J. Magn. Reson. Imaging* 2006; 24:556–562.

[46] van Holten MJ, Roesink JM, Terhaard CHJ, Braam PM. New insights in the vascular supply of the human parotid gland-Consequences for parotid gland-sparing irradiation. *Head Neck* 2009;32:837–843.

[47] Dirix P, de Keyzer F, Vandecaveye V, Stroobants S, Hermans R, Nuyts S. Diffusion-weighted magnetic resonance imaging to evaluate major salivary gland function before and after radiotherapy. *Int. J. Radiat. Oncol. Biol. Phys.* 2008;71:1365–1371.

[48] Simon Zoula SC, Boesch C, De Keyzer F, Thoeny HC. Functional imaging of the parotid glands using blood oxygenation level dependent (BOLD)-MRI at 1.5T and 3T. *J. Magn. Reson. Imaging* 2008;27:43–48.

[49] Kim S, Loevner LA, Quon H, *et al.* Prediction of response to chemoradiation therapy in squamous cell carcinomas of the head and neck using dynamic contrast-enhanced MR imaging. *Am. J. Neuroradiol.* 2010;31:262–268.

[50] Bisdas S, Medov L, Baghi M, *et al.* A comparison of tumour perfusion assessed by deconvolution-based analysis of dynamic contrast-enhanced CT and MR imaging in patients with squamous cell carcinoma of the upper aerodigestive tract. *Eur. Radiol.* 2008;18:843–850.

[51] Jansen JFA, Schöder H, Lee NY, *et al.* Noninvasive assessment of tumor microenvironment using dynamic contrast-enhanced magnetic resonance imaging and (18)F-Fluoromisonidazole positron emission tomography imaging in neck nodal metastases. *Int. J. Radiat. Oncol. Biol. Phys.* 2010;77:1403–1410.

[52] Shukla-Dave A, Lee N, Stambuk H, *et al.* Average arterial input function for quantitative dynamic contrast enhanced magnetic resonance imaging of neck nodal metastases. *BMC Med. Phys.* 2009;9:4.

[53] Newbold K, Castellano I, Charles-Edwards E, *et al.* An exploratory study into the role of dynamic contrast-enhanced magnetic resonance imaging or perfusion computed tomography for detection of intratumoral hypoxia in head-and-neck cancer. *Int. J. Radiat. Oncol. Biol. Phys.* 2009;74:29–37.

[54] Bisdas S, Seitz O, Middendorp M, *et al.* An exploratory pilot study into the association between microcirculatory parameters derived by MRI-based pharmacokinetic analysis and glucose utilization estimated by PET-CT imaging in head and neck cancer. *Eur. Radiol.* 2010;20:2358–2366.

[55] Schabel MC, Parker DL. Uncertainty and bias in contrast concentration measurements using spoiled gradient echo pulse sequences. *Phys. Med. Biol.* 2008;53:2345–2373.

[56] Ishida M, Sakuma H, Murashima S, *et al.* Absolute blood contrast concentration and blood signal saturation on myocardial perfusion MRI: estimation from CT data. *J. Magn. Reson. Imaging* 2009; 29:205–210.

[57] Halvorsen RA. Which study when? Iodinated contrast-enhanced CT versus gadolinium-enhanced MR imaging. *Radiology* 2008;249:9–15.

[58] Sobin LH, Wittekind C. TNM classification of malignant tumours, 6th edition. 2002. *Wiley-Liss, New York, NY, USA.*

[59] Houweling AC, Dijkema T, Roesink JM, Terhaard CHJ, Raaijmakers CPJ. Sparing the contralateral submandibular gland in oropharyngeal cancer patients: A planning study. *Radiother. Oncol.* 2008;89:64–70.

[60] Brookes JA, Redpath TW, Gilbert FJ, Murray AD, Staff RT. Accuracy of T1 measurement in dynamic contrast-enhanced breast MRI using two- and three-dimensional variable flip angle fast low-angle shot. *J. Magn. Reson. Imaging* 1999;9:163–171.

References

[61] Pintaske J, Martirosian P, Graf H, *et al.* Relaxivity of gadopentetate dimeglumine (Magnevist), gadobutrol (Gadovist), and gadobenate dimeglumine (MultiHance) in human blood plasma at 0.2, 1.5, and 3 Tesla. *Invest. Radiol.* 2006;41:213–221.

[62] Klein S, Staring M, Murphy K, Viergever MA, Pluim JPW. Elastix: a toolbox for intensity-based medical image registration. *IEEE Trans. Med. Imaging* 2010;29:196–205.

[63] Tofts PS, Brix G, Buckley DL, *et al.* Estimating kinetic parameters from dynamic contrast-enhanced T1-weighted MRI of a diffusable tracer: standardized quantities and symbols. *J. Magn. Reson. Imaging* 1999;10:223–232.

[64] Lawrence C, Zhou JL, Tits AL. User's guide for CFSQP Version 2.5: A C code for solving constrained nonlinear optimization problems, generating iterates satisfying all inequality constraints. 1994.

[65] Korporaal JG, van den Berg CAT, Groenendaal G, Moman MR, van Vulpen M, van der Heide UA. The use of probability maps to deal with the uncertainties in prostate cancer delineation. *Radiother. Oncol.* 2010;94:168–172.

[66] Akbudak E, Conturo TE. Arterial input functions from MR phase imaging. *Magn. Reson. Med.* 1996; 36:809–815.

[67] Ibrahim TS, Abduljalil AM, Baertlein BA, Lee R, Robitaille PL. Analysis of b_1 field profiles and SAR values for multi-strut transverse electromagnetic RF coils in high field MRI applicaitons. *Phys. Med. Biol.* 2001;46:2545–2555.

[68] Cao Y, Popovtzer A, Li D, *et al.* Early prediction of outcome in advanced head-and-neck cancer based on tumor blood volume alterations during therapy: a prospective study. *Int. J. Radiat. Oncol. Biol. Phys.* 2008;72:1287–1290.

[69] Van Cann EM, Rijpkema M, Heerschap A, van der Bilt A, Koole R, Stoelinga PJW. Quantitative dynamic contrast-enhanced MRI for the assessment of mandibular invasion by squamous cell carcinoma. *Oral Oncol.* 2008;44:1147–1154.

[70] Anand AK, Jain J, Negi PS, *et al.* Can dose reduction to one parotid gland prevent xerostomia?–A feasibility study for locally advanced head and neck cancer patients treated with intensity-modulated radiotherapy. *Clin Oncol* 2006;18:497–504.

[71] Braam PM, Terhaard CH, Roesink JM, Raaijmakers CPJ. Intensity-modulated radiotherapy significantly reduces xerostomia compared with conventional radiotherapy. *Int. J. Radiat. Oncol. Biol. Phys.* 2006;66:975–980.

[72] Eisbruch A, Ship JA, Martel MK, *et al.* Parotid gland sparing in patients undergoing bilateral head and neck irradiation: techniques and early results. *Int. J. Radiat. Oncol. Biol. Phys.* 1996;36:469–480.

[73] Kam MKM, Leung SF, Zee B, *et al.* Prospective randomized study of intensity-modulated radiotherapy on salivary gland function in early-stage nasopharyngeal carcinoma patients. *J. Clin. Oncol.* 2007; 25:4873–4879.

[74] Burlage FR, Coppes RP, Meertens H, Stokman MA, Vissink A. Parotid and submandibular/sublingual salivary flow during high dose radiotherapy. *Radiother. Oncol.* 2001;61:271–274.

[75] Murdoch-Kinch C, Kim HM, Vineberg KA, Ship JA, Eisbruch A. Dose-effect relationships for the submandibular salivary glands and implications for their sparing by intensity modulated radiotherapy. *Int. J. Radiat. Oncol. Biol. Phys.* 2008;72:373–382.

[76] Saarilahti K, Kouri M, Collan J, *et al.* Sparing of the submandibular glands by intensity modulated radiotherapy in the treatment of head and neck cancer. *Radiother. Oncol.* 2006;78:270–275.

[77] Saibishkumar EP, Jha N, Scrimger RA, *et al.* Sparing the parotid glands and surgically transferred submandibular gland with helical tomotherapy in post-operative radiation of head and neck cancer: a planning study. *Radiother. Oncol.* 2007;85:98–104.

[78] van de Water TA, Bijl HP, Westerlaan HE, Langendijk JA. Delineation guidelines for organs at risk involved in radiation-induced salivary dysfunction and xerostomia. *Radiother. Oncol.* 2009;93:545–552.

[79] Rasch C, Keus R, Pameijer FA, *et al.* The potential impact of CT-MRI matching on tumor volume delineation in advanced head and neck cancer. *Int. J. Radiat. Oncol. Biol. Phys.* 1997;39:841–848.

[80] Geets X, Daisne J, Arcangeli S andCoche E, *et al.* Inter-observer variability in the delineation of pharyngo-laryngeal tumor, parotid glands and cervical spinal cord: comparison between CT-scan and MRI. *Radiother. Oncol.* 2005;77:25–31.

[81] Ahmed M, Schmidt M, Sohaib A, *et al.* The value of magnetic resonance imaging in target volume delineation of base of tongue tumours–a study using flexible surface coils. *Radiother. Oncol.* 2010; 94:161–167.

[82] Kalinowski M, Heverhagen J, Rehberg E, Klose K, Wagner H. Comparative study of MR sialography and digital subtraction sialography for benign salivary gland disorders. *AJNR Am J Neuroradiol* 2002; 23:1485–1492.

[83] Jager L, Menauer F, Holzknecht N, Scholz V, Grevers G, Reiser M. Sialolithiasis: MR sialography of the submandibular duct–an alternative to conventional sialography and US? *Radiology* 2000;216:665–671.

[84] Cerezo L, Martín M, López M, Marín A, Gómez A. Ipsilateral irradiation for well lateralized carcinomas of the oral cavity and oropharynx: results on tumor control and xerostomia. *Radiat. Oncol.* 2009;4:33.

[85] Rusthoven KE, Raben D, Schneider C, Witt R, Sammons S, Raben A. Freedom from local and regional failure of contralateral neck with ipsilateral neck radiotherapy for node-positive tonsil cancer: results of a prospective management approach. *Int. J. Radiat. Oncol. Biol. Phys.* 2009;74:1365–1370.

[86] Vissink A, Panders AK, 's Gravenmade EJ, Vermey A. The causes and consequences of hyposalivation. *Ear Nose Throat* 1988;67:166–176.

[87] Eisbruch A. Reducing xerostomia by IMRT: what may, and may not, be achieved. *J. Clin. Oncol.* 2007; 25:4863–4864.

[88] Braaksma MMJ, Wijers OB, van Sörnsen de Koste JR, *et al.* Optimisation of conformal radiation therapy by intensity modulation: cancer of the larynx and salivary gland function. *Radiother. Oncol.* 2003; 66:291–302.

[89] Jensen K, Overgaard M, Grau C. Morbidity after ipsilateral radiotherapy for oropharyngeal cancer. *Radiother. Oncol.* 2007;85:90–97.

[90] de Kruijf WJM, Heijmen BJM, Levendag PC. Quantification of trade-off between parotid gland sparing and planning target volume underdosages in clinically node-negative head-and-neck intensity-modulated radiotherapy. *Int. J. Radiat. Oncol. Biol. Phys.* 2007;68:136–143.

[91] Prins-Braam P, Raaijmakers CPJ, Terhaard CHJ. Location of cervical lymph node metastasis in oropharyngeal or hypopharyngeal carcinoma: implications for cranial field borders. *Int. J. Radiat. Oncol. Biol. Phys.* 2004;58:132–138.

[92] Grégoire V, Coche E, Cosnard G, Hamoir M, Reychler H. Selection and delineation of lymph node target volumes in head and neck conformal radiotherapy.proposal for standarizing terminology and procedure based on the surgical experience. *Radiother. Oncol.* 2000;56:135–150.

[93] Van Asselen B, Dehnad H, Raaijmakers CPJ, Lagendijk JJW, Terhaard CHJ. Implanted gold markers for positioning verification during irradiation of head-and-neck cancers: a feasibility study. *Int. J. Radiat. Oncol. Biol. Phys.* 2003;59:1011–1017.

[94] Van Asselen B, Dehnad H, Raaijmakers CPJ, Roesink JM, Lagendijk JJW, Terhaard CHJ. The dose to the parotid glands with IMRT for oropharyngeal tumors: the effect of reduction of positioning margins. *Radiother. Oncol.* 2002;64:197–204.

[95] Bol GH, Kotte ANTJ, Lagendijk JJW. jVolumetool: an image evaluation, registration, and delineation system for radiotherapy. *Phys. Med.* 2003;XIX:80.

[96] Astreinidou E, Bel A, Raaijmakers CPJ, Terhaard CHJ, Lagendijk JJW. Adequate margins for random setup uncertainties in head-and-neck IMRT. *Int. J. Radiat. Oncol. Biol. Phys.* 2005;61:938–944.

[97] O'Daniel JC, Garden AS, Schwartz DL, *et al.* Parotid gland dose in intensity-modulated radiotherapy for head and neck cancer: is what you plan what you get? *Int. J. Radiat. Oncol. Biol. Phys.* 2007;69:1290–1296.

[98] Suzuki M, Nishimura Y, Nakamatsu K, *et al.* Analysis of interfractional set-up errors and intrafractional organ motions during IMRT for head and neck tumors to define an appropriate planning target volume (PTV)- and planning organs at risk volume (PRV)-margins. *Radiother. Oncol.* 2006;78:283–290.

[99] Eisbruch A, Marsh LH, Dawson LA, *et al.* Recurrences near base of skull after IMRT for head-and-neck cancer: implications for target delineation in high neck and for parotid gland sparing. *Int. J. Radiat. Oncol. Biol. Phys.* 2004;59:28–42.

[100] Boda-Heggemann J, Walter C, Rahn A, *et al.* Repositioning accuracy of two different mask systems-3D revisited: comparison using true 3D/3D matching with cone-beam CT. *Int. J. Radiat. Oncol. Biol. Phys.* 2006;66:1568–1575.

References

[101] Xu F, Wang J, Bai S, *et al.* Detection of intrafractional tumour position error in radiotherapy utilizing cone beam computed tomography. *Radiother. Oncol.* 2008;89:311–319.

[102] Li H, Zhu XR, Zhang L, *et al.* Comparison of 2D radiographic images and 3D cone beam computed tomography for positioning head-and-neck radiotherapy patients. *Int. J. Radiat. Oncol. Biol. Phys.* 2008;71:916–925.

[103] Van Kranen S, Van Beek S, Rasch C, Van Herk M, Sonke JJ. Setup uncertainties of anatomical sub-regions in head-and-neck cancer patients after offline CBCT guidance. *Int. J. Radiat. Oncol. Biol. Phys.* 2009;73:1566–1573.

[104] Polat B, Wilbert J, Baier K, Flentje M, Guckenberger M. Nonrigid patient setup errors in the head-and-neck region. *Strahlenther. Onkol.* 2007;183:506–511.

[105] Zhang L, Garden AS, Lo J, *et al.* Multiple regions-of-interest analysis of setup uncertainties for head-and-neck cancer radiotherapy. *Int. J. Radiat. Oncol. Biol. Phys.* 2006;64:1559–1569.

[106] Van Herk M. Errors and margins in radiotherapy. *Semin. Radiat. Oncol.* 2004;14:52–64.

[107] De Boer HCJ, Heijmen BJM. eNAL: An extension of the NAL setup correction protocol for effective use of weekly follow-up measurements. *Int. J. Radiat. Oncol. Biol. Phys.* 2007;67:1586–1595.

[108] Deasy JO. Comments on the use of the Lyman-Kutcher-Burman model to describe tissue response to nonuniform irradiation. *Int. J. Radiat. Oncol. Biol. Phys.* 2000;47:1458–1460.

[109] Semenenko VA, Li XA. Lyman-Kutcher-Burman NTCP model parameters for radiation pneumonitis and xerostomia based on combined analysis of published clinical data. *Phys. Med. Biol.* 2008;53:737–755.

[110] Källman P, Agren A, Brahme A. Tumour and normal tissue responses to fractionated non-uniform dose delivery. *Int. J. Radiat. Biol.* 1992;62:249–262.

[111] Stavreva NA, Stavrev PV. Some limitations of the application of the NTCP model describing the response of organs with 'relatively serial' structure. *Int. J. Radiat. Biol.* 2002;78:948–50.

[112] Niemierko A, Goitein M. Modeling of normal tissue response to radiation: the critical volume model. *Int. J. Radiat. Oncol. Biol. Phys.* 1993;25:135–145.

[113] van Luijk P, Delvigne TC, Schilstra C, Schippers JM. Estimation of parameters of dose-volume models and their confidence limits. *Phys. Med. Biol.* 2003;48:1863–1884.

[114] Seppenwoolde Y, Lebesque JV, de Jaeger K, *et al.* Comparing different NTCP models that predict the incidence of radiation pneumonitis. *Int. J. Radiat. Oncol. Biol. Phys.* 2003;55:724–735.

[115] Jackson A, Kutcher GJ, Yorke ED. Probability of radiation-induced complications for normal tissues with parallel architecture subject to non-uniform irradiation. *Med. Phys.* 1993;20:613–625.

[116] Jackson A, Haken RKT, Robertson JM, Kessler ML, Kutcher GJ, Lawrence TS. Analysis of clinical complication data for radiation hepatitis using a parallel architecture model. *Int. J. Radiat. Oncol. Biol. Phys.* 1995;31:883–891.

[117] R Development Core Team. R: A Language and Environment for Statistical Computing. 2009. *R Foundation for Statistical Computing, Vienna, Austria.*

[118] Motulsky HJ, Christopoulos A. Fitting models to biological data using linear and nonlinear regression. A practical guide to curve fitting. 2003. *GraphPad Software Inc., San Diego, CA, USA.*

[119] Steel GG. Basic clinical radiobiology. 4th ed, 2002. *Arnold, London, UK.*

[120] Eisbruch A, Ship JA, Kim HM, Ten Haken R. Partial irradiation of the parotid gland. *Semin Radiat Oncol.* 2001;11:234–239.

[121] Franzén L, Gustafsson H, Sundström S, Karlsson M, Littbrand B, Henriksson R. Fractionated irradiation and late changes in rat parotid gland: effects on the number of acinar cells, potassium efflux, and amylase secretion. *Int. J. Radiat. Oncol. Biol. Phys.* 1993;64:93–101.

[122] Collett D. Modelling binary data. 1st ed, 1991. *Chapman & Hall, London, UK.*

[123] Mavroidis P, Lind BK, Theodorou K, *et al.* Statistical methods for clinical verification of dose-response parameters related to esophageal stricture and AVM obliteration from radiotherapy. *Phys. Med. Biol.* 2004;49:3797–3816.

[124] Grobbee DE, Hoes AW. Clinical epidemiology: principles, methods, and applications for clinical research. 2008. *Jones and Bartlett, Boston, MA, USA.*

[125] Burnham KP, Anderson DR. Model selection and multimodel inference. 2002. *Springer, New York, NY, USA.*

[126] Konings A, Cotteleer F, Faber H, van Luijk P, Meertens H, Coppes R. Volume effects and region-dependent radiosensitivity of the parotid gland. *Int. J. Radiat. Oncol. Biol. Phys.* 2005;62:1090–1095.

[127] Thames HD, Zhang M, Tucker SL, Liu HH, Dong L, Mohan R. Cluster models of dose-volume effects. *Int. J. Radiat. Oncol. Biol. Phys.* 2004;59:1491–1504.

[128] Konouchi H, Asaumi J, Yanagi Y, *et al.* Evaluation of tumor proliferation using dynamic contrast enhanced-MRI of oral cavity and oropharyngeal squamous cell carcinoma. *Oral Oncol.* 2003;39:290–295.

[129] Raktoe SAS, Dehnad H, Raaijmakers CPJ, Terhaard CHJ. Recurrence after intensity-modulated radiotherapy of head-and-neck squamous cell carcinoma. 2010. Unpublished manuscript.

[130] Kerkhof EM, Van der Put RW, Raaymakers BW, Van der Heide UA, Jürgenliemk-Schulz IM, Lagendijk JJW. Intrafraction motion in patients with cervical cancer: the benefit of soft tissue registration using MRI. *Radiother. Oncol.* 2009;93:115–121.

[131] Raaymakers BW, Lagendijk JJW, Overweg J, *et al.* Integrating a 1.5 T MRI scanner with a 6 MV accelerator: proof of concept. *Phys. Med. Biol.* 2009;54:N229–237.

[132] Raaijmakers CPJ, Roesink JM, Dijkema T, Houweling AC, Terhaard CHJ. Parotid gland function after radiotherapy. *Lancet Oncol.* 2010;11:412.

[133] Popovtzer A, Cao Y, Feng FY, Eisbruch A. Anatomical changes in the pharyngeal constrictors after chemo-irradiation of head and neck cancer and their dose-effect relationships: MRI-based study. *Radiother. Oncol.* 2009;93:510–515.

[134] Houweling AC, van den Berg CAT, Roesink JM, Terhaard CHJ, Raaijmakers CPJ. Early radiation-induced changes in the salivary glands on MRI. In: *Proceedings ESTRO 2010: Abstracts*. Barcelona, Spain, 2010; S315.

Publications

Published papers

Sparing the contralateral submandibular gland in oropharyngeal cancer patients: A planning study. A.C. Houweling, T. Dijkema, J.M. Roesink, C.H.J. Terhaard, C.P.J. Raaijmakers. *Radiother. Oncol.* 2008; **89**:64–70.

A comparison of dose-response models for the parotid gland in a large group of head-and-neck cancer patients. A.C. Houweling, M.E.P. Philippens, T. Dijkema, J.M. Roesink, C.H.J. Terhaard, C. Schilstra, R.K. Ten Haken, A. Eisbruch, C.P.J. Raaijmakers. *Int. J. Radiat. Oncol. Biol. Phys.* 2009; **76**:1259–1265.

Parotid gland function after radiotherapy: the combined Michigan and Utrecht experience. T. Dijkema, C.P.J. Raaijmakers, R.K. Ten Haken, J.M. Roesink, P.M. Braam, A.C. Houweling, M.A. Moerland, A. Eisbruch, C.H.J. Terhaard. *Int. J. Radiat. Oncol. Biol. Phys.* 2010; **78**:449–453.

Improved immobilization using an individual head support in head-and-neck cancer patients. A.C. Houweling, S. van der Meer, E. van der Wal, C.H.J. Terhaard, C.P.J. Raaijmakers. *Radiother. Oncol.* 2010; **96**:100–103.

Parotid gland function after radiotherapy. C.P.J. Raaijmakers, J. M. Roesink, T. Dijkema, A.C. Houweling, C.H.J. Terhaard. *Lancet Oncol.* 2010; **11**:515–516.

Magnetic resonance imaging at 3.0 T for submandibular gland sparing radiotherapy. A.C. Houweling, C.A.T. van den Berg, J.M. Roesink, C.H.J. Terhaard, C.P.J. Raaijmakers. *Radiother. Oncol.* 2010; **97**:239–243.

Submitted papers

Dynamic contrast-enhanced MRI at 3.0 T in oropharyngeal cancer patients. A.C. Houweling, C.A.T. van den Berg, C.H.J. Terhaard, C.P.J. Raaijmakers. *Radiother. Oncol.* 2010.

Proceedings and abstracts

The evaluation of radiation-induced changes in water content of the parotid gland using MRI. A.C. Houweling, C.A.T. van den Berg, T. Dijkema, J.M. Roesink, C.H.J. Terhaard, C.P.J. Raaijmakers. *ISMRM, 2008, 16th Scientific Meeting, Toronto, Canada.*

Sparing the contralateral submandibular gland in oropharyngeal cancer patients using IMRT: a planning study. A.C. Houweling, T. Dijkema, J.M. Roesink, C.H.J. Terhaard, C.P.J. Raaijmakers. *ESTRO, 2008, 27th Annual Meeting, Göteborg, Sweden.*

The use of MRI in the evaluation of radiation-induced changes in water and fat content of the parotid gland. C.P.J. Raaijmakers, A.C. Houweling, C.A.T. van den Berg, T. Dijkema, J.M. Roesink, C.H.J. Terhaard. *ESTRO, 2008, 27th Annual Meeting, Göteborg, Sweden.*

The mean dose model is preferred for describing parotid gland complications after radiotherapy. A.C. Houweling, M.E.P. Philippens, T. Dijkema, J.M. Roesink, C. Schilstra, C.H.J. Terhaard, C.P.J. Raaijmakers. *PREVENT, 2009, Brussels, Belgium.*

Comparison of post-contrast MR and perfusion MR in oropharyngeal cancer patients for GTV delineation. A.C. Houweling, C.A.T. van den Berg, J.M. Roesink, C.H.J. Terhaard, C.P.J. Raaijmakers. *ESTRO, 2009, 10^{t}h Biennial Meeting, Maastricht, The Netherlands.*

MR sialography at 3T for delineation of the submandibular gland. A.C. Houweling, C.A.T. van den Berg, J.M. Roesink, C.H.J. Terhaard, C.P.J. Raaijmakers. *ESTRO, 2009, 10^{t}h Biennial Meeting, Maastricht, The Netherlands.*

Improved head-and-neckpatient positioningusing an individual head support. S. van der Meer, A.C. Houweling, E. van der Wal, C.H.J. Terhaard, C.P.J. Raaijmakers. *ESTRO, 2009, 10^{t}h Biennial Meeting, Maastricht, The Netherlands.*

Radiotherapy for CNS and H&N cancer: The influence of the head support. C.P.J. Raaijmakers, S. van der Meer, A.C. Houweling, C.H.J. Terhaard, E. van der Wal. *ESTRO, 2009, 10^{t}h Biennial Meeting, Maastricht, The Netherlands.*

Tracer kinetic model fitting of dynamic contrast-enhanced MRI at 3.0 T in oropharyngeal cancer patients. A.C. Houweling, C.A.T. van den Berg, C.H.J. Terhaard, C.P.J. Raaijmakers. *ICCR, 2010, 16th Scientific Meeting, Amsterdam, The Netherlands.*

Early radiation-induced changes in the salivary glands on MRI. A.C. Houweling, C.A.T. van den Berg, J.M. Roesink, C.H.J. Terhaard, C.P.J. Raaijmakers. *ESTRO, 2010, 29^{t}h Annual Meeting, Barcelona, Spain.*

Nederlandse samenvatting

Mond- en keelholte tumoren komen relatief weinig voor, jaarlijks worden er ongeveer 2700 nieuwe gevallen gediagnosticeerd. Dit is ongeveer 3% van alle nieuwe kankerpatiënten in Nederland. Radiotherapie is, naast chirurgie, de standaard behandeling voor patiënten met een mond- of keelholte tumor. Bij een radiotherapiebehandeling wordt gebruik gemaakt van ioniserende straling. Patiënten worden in dagelijkse bestralingsfracties, gedurende enkele opeenvolgende weken bestraald. De ioniserende straling zorgt voor schade aan de weefsels, waarbij er altijd wordt geprobeerd de tumor een zo hoog mogelijke dosis te geven om zo alle kankercellen te doden. Tegelijkertijd wil men de gezonde omliggende weefsels zo min mogelijk beschadigen en moet de dosis daar juist zo laag mogelijk zijn.

Het mond- en keelholtegebied is een erg complexe anatomie met veel gezonde stralingsgevoelige organen. Daarnaast is er veel beweging rond de te behandelen tumor door slikken en ademhaling en zijn er lymfeklieren die behandeld moeten worden. Dit alles maakt radiotherapie in dit gebied een lastige opgave met een grote kans op complicaties. Een van de meest voorkomende complicaties is een droge mond, ook wel xerostomie genoemd. De speekselklieren zijn erg stralingsgevoelig en de locatie van deze klieren ten opzichte van de tumor is op zijn zachts gezegd onhandig.

Ongeveer 90% van het speeksel wordt geproduceerd door de grote speekselklieren, de oorspeekselklier (glandula parotis), de onderkaakspeekselklier (glandula submandibularis) en de ondertongspeekselklier (glandula sublingualis). De oorspeekselklier, of kortweg parotis, bevindt zich zoals de naam al doet vermoeden naast het oor. Bij stimulatie van de speekselproductie, zoals tijdens eten of spreken, produceert deze klier ongeveer 60% van de totale hoeveelheid speeksel. De onderkaakspeekselklier, ook wel submandibularis genoemd, is bij de onderkaak gelegen en heeft zijn grootste bijdrage aan de speekselproductie tijdens rust. Wanneer de speekselklieren beschadigd worden door bestraling en minder of geen speeksel produceren, heeft dit vervelende gevolgen. Patiënten hebben na de behandeling vaak problemen met eten, praten, slikken en de gezondheid van het gebit. Aangezien er tot op heden geen doeltreffende remedie is voor xerostomie, is het voorkomen ervan door de stralingsdosis op de speekselklieren te verlagen de meest doeltreffende behandeling.

Nederlandse samenvatting

Voorafgaand aan de radiotherapiebehandeling wordt de locatie van zowel de tumor als van de risico-organen in beeld gebracht. De standaard beeldvormingtechniek binnen de radiotherapie is CT (computed tomography), waarmee voornamelijk botstructuren afgebeeld kunnen worden. Een andere beeldvormingtechniek, MRI (magnetic resonance imaging), heeft echter vele voordelen boven CT, waarbij de belangrijkste is dat zachte weefsels zoals de speekselklieren kunnen worden afgebeeld. Daarnaast worden functionele beeldvormingtechnieken, gebaseerd op bijvoorbeeld CT of MRI, steeds belangrijker, omdat die ook biologische informatie over de tumor weergeven.

Nadat de tumor en de risico-organen gedefinieerd zijn, wordt er een bestralingsplan gemaakt. Recente ontwikkelingen hebben de radiotherapietechniek aanzienlijk verbeterd. Waar de behandeling vroeger met enkele rechthoekige bundels gegeven werd, zijn bundels met onregelmatige vorm gebaseerd op driedimensionale medische beeldvorming nu de standaard. Een meer geavanceerde vorm van radiotherapie is IMRT (intensity-modulated radiotherapy). Hierbij is zowel de vorm van de stralingsbundel als de intensiteit binnen de bundel aangepast aan het te bestralen gebied. Door gebruik te maken van de IMRT techniek kan een hoge en homogene dosisverdeling in de tumor verkregen worden en door de scherpere dosisgradiënten kunnen gezonde weefsels makkelijker gespaard worden.

Tijdens iedere bestralingsfractie is het belangrijk te weten waar de tumor en de risico-organen zich bevinden ten opzichte van elkaar en van de bestralingsbundels. Om de onzekerheid in tumorpositie op te vangen wordt er een extra marge rond de tumor bestraald. Hierdoor ontvangt het direct omliggende gezonde weefsel echter ook een hogere dosis. Direct voor elke fractie kan op het bestralingstoestel een cone-beam CT gemaakt worden. Deze cone-beam CT wordt over de CT gelegd die voor de behandeling is gemaakt. Hierdoor kan de dagelijkse positie van de patiënt met meer zekerheid vastgesteld worden en kunnen kleinere marges gebruikt worden.

Om patiënten zo stil mogelijk te laten liggen gedurende een fractie krijgen zij een speciaal masker aangemeten. Dit masker, gecombineerd met een speciale hoofdsteun, reduceert de beweging van het hoofd en de nek drastisch en verbetert de reproduceerbaarheid van de positionering van de patiënt. Echter, bewegingen door bijvoorbeeld slikken zijn ondanks het masker nog mogelijk en zorgen voor een onzekerheid in de positie van de tumor.

In dit proefschrift worden aspecten uit alle stadia van een radiotherapiebehandeling in het mond- en keelholtegebied besproken. Hierbij ligt de nadruk op de complicaties die het gevolg zijn van schade aan de grote speekselklieren. De onderwerpen in dit proefschrift worden besproken in dezelfde volgorde als patiënten de behandeling ondergaan: van medische beeldvorming, via dagelijkse behandeling tot helaas in een redelijk aantal gevallen een verminderde speekselproductie.

In hoofdstuk 2 wordt een nieuwe techniek besproken om de doorbloeding van weefsels af te beelden, DCE-MRI (dynamic contrast-enhanced MRI). De doorbloeding van

een tumor is gerelateerd aan de gevoeligheid voor straling en de effectiviteit van de behandeling. Om dit te meten wordt een contrastmiddel ingespoten, waarna de verdeling hiervan in het lichaam met herhaalde MRI beelden wordt afgebeeld. De verdeling van het contrastmiddel kan vervolgens op een kwantitatieve manier geanalyseerd worden, waarbij doorbloedingparameters bepaald worden. Deze doorbloedingparameters kunnen vergeleken worden tussen patiënten en ook het effect van de behandeling in de tijd kan worden onderzocht. Deze techniek is relatief nieuw in het mond- en keelholtegebied en de uitvoerbaarheid bij patiënten met een keelholtetumor is aangetoond in hoofdstuk 2.

Bewegingen door bijvoorbeeld slikken geven problemen bij het maken van een MRI in het mond- en keelholtegebied, wat zeker bij herhaalde MRI beelden een grote rol speelt. Deze bewegingen kunnen echter door middel van het fuseren van de MRI beelden verminderd worden. De noodzaak van deze methode voor de analyse van DCE-MRI data van patiënten met een keelholtetumor is onderzocht in hoofdstuk 2, maar het bleek de doorbloedingparameters in de tumor niet wezenlijk te veranderen. De doorbloeding van de tumor was significant hoger dan de doorbloeding van gezond weefsel. Daarnaast zijn er binnen de tumor duidelijk verschillen in doorbloeding te vinden, wat gebruikt zou kunnen worden in het plannen van de bestraling. Al met al is DCE-MRI een interessante beeldvormingtechniek om meer inzicht te krijgen in de doorbloeding van de tumor en deze techniek kan gebruikt gaan worden om de radiotherapiedosis in de tumor te sturen.

Naast het bepalen van de positie van de tumor, is het afbeelden van de risico-organen erg belangrijk voor het plannen van de radiotherapiebehandeling. De speekselklieren zijn erg stralingsgevoelig en geven veel complicaties na behandeling van de tumor. Om deze speekselklier goed te kunnen sparen, moet deze eerst goed afgebeeld worden, zoals met MRI mogelijk is. In hoofdstuk 3 wordt MR sialografie geïntroduceerd, een nieuwe MRI techniek waarbij voornamelijk water, zoals in speeksel aanwezig is, wordt afgebeeld. Op deze beelden is het volume van de speekselklier te zien met een gemiddelde intensiteit, zien we de afvoerende speekselkanalen als heldere structuren in het kliervolume en is de achtergrond donker.

Om de toegevoegde waarde van MR sialografie te bepalen is het volume van de submandibularis gedefinieerd op alleen CT beelden, op een combinatie van CT en standaard MRI en op MR sialografie beelden. Het volume dat op MR sialografie beelden gebaseerd was, had een significant groter volume én de zichtbare bovengrens van de klier lag hoger. Door de verbetering in het definiëren van het volume van de submandibularis kan de dosis die aan deze klier gegeven wordt doeltreffender verlaagd worden, waardoor de kans op complicaties lager is.

Nadat alle beeldvorming is gedaan en de locatie van zowel de tumor als de gezonde weefsels gedefinieerd is, wordt het bestralingsplan gemaakt. Hoofdstuk 4 beschrijft een vooruitstrevende IMRT techniek waarbij beide parotiden en één submandibularis gespaard kunnen worden. Een tumor bevindt zich over het algemeen aan één zijde in

een patiënt. Door het gebruik van marges is er vrijwel volledige overlap van de sub-mandibularis aan de tumorzijde met de te behandelen volumes. Echter, aan de andere zijde, de contralaterale zijde, is deze overlap slechts gedeeltelijk en is er ruimte om de speekselklier te sparen.

Met de IMRT techniek uit hoofdstuk 4 is het mogelijk om de dosis in de submandibularis aan de contralaterale zijde te verlagen. Wanneer een kleine en slechts lokale onderdosering van het aangrenzende lymfekliergebied wordt toegestaan, kan de dosis met ongeveer 12 Gy tot een gemiddelde dosis van 40 Gy worden verlaagd. Hierdoor neemt de complicatiekans af van 85% tot ongeveer 50%. Verder is uit hoofdstuk 4 gebleken dat het verkleinen van de marges rond de tumor en lymfeklieren een grote invloed heeft op de reductie van de dosis op de submandibularis.

De onzekerheid in tumorpositie kan verminderd worden door het dagelijks afbeelden van het te bestralen gebied met cone-beam CT. Een andere aanpak is het optimaliseren van het masker of de hoofdsteun waarmee de patiënt op steeds dezelfde positie wordt neergelegd. In hoofdstuk 5 is een nieuwe patiëntspecifieke hoofdsteun beschreven. Normaliter krijgen patiënten een hoofdsteun met een standaard vorm in combinatie met het op maat gemaakte masker. Bij de nieuwe hoofdsteun wordt een afdruk van de achterkant van het hoofd van de patiënt gemaakt door het hoofd stevig in een speciaal schuim te drukken. Deze patiëntspecifieke hoofdsteun past daardoor beter en geeft meer steun door de verbeterde vorm.

Om een objectieve vergelijking tussen de standaard en de patiëntspecifieke hoofdsteun te maken, wordt er voor en na elke behandelfractie een cone-beam CT beeld gemaakt. Door deze beelden te fuseren met de planning CT, die voor de start van de behandeling is gemaakt, kan de fout in positionering van de patiënt bepaald worden. De fout bij het gebruik van de patiëntspecifieke hoofdsteun was significant kleiner dan bij de standaard hoofdsteun. Aan de hand van de resultaten van dit onderzoek is de klinische marge rond de tumor verkleind van 5 mm naar 3 mm, waardoor de speekselklieren makkelijker gespaard kunnen worden.

Er zijn verschillende zogeheten NTCP (normal tissue complication probability) modellen die de kans op een speekselkliercomplicatie voorspellen op basis van een bepaalde dosisverdeling. Het is echter niet duidelijk welk van deze modellen de complicatiekans het beste voorspelt. In hoofdstuk 6 worden zes veel gebruikte NTCP modellen vergeleken om zo de reactie van de parotis op een bepaalde dosis te onderzoeken. Om deze relatie correct te kunnen voorspellen is een grote patiëntengroep nodig. Daarom zijn de patiënten datasets uit het Universitair Medisch Centrum Utrecht en de Universiteit van Michigan samengevoegd tot de grootste gepubliceerde dataset tot nu toe. De verschillende modellen konden alle goed de complicaties voorspellen, maar het gemiddelde-dosis model was hierin het beste. Uit dit model blijkt dat een gemiddelde dosis op de parotis van 39 Gy tot 50% complicaties leidt.

Al met al zijn aspecten uit alle stadia van de behandeling van patiënten met een mond- of keelholtetumor beschreven in dit proefschrift. Een nieuwe MRI techniek voor het afbeelden van de doorbloeding van de tumor, DCE-MRI, kan toegepast worden bij deze patiënten. De submandibularis wordt beter gedefinieerd met behulp van MRI en een nieuwe behandeltechniek maakt het mogelijk de dosis in deze klier te verlagen. Door gebruik te maken van een patiëntspecifieke hoofdsteun liggen patiënten stiller en zijn de marges verkleind. En als laatste is de definitieve curve voor de relatie tussen de dosis en de complicaties van de parotis beschreven. De aanpassingen in de behandeling van patiënten met een mond- of keelholtetumor besproken in dit proefschrift lijken misschien aan de kleine kant, maar gezamenlijk zullen ze leiden tot een aanzienlijke vermindering van de kans op een droge mond na radiotherapie.

Dankwoord

Aan het begin van mijn promotie-onderzoek leken 4 jaren oneindig lang, nu mijn proefschrift af is lijken ze voorbij gevlogen. Een aantal mensen wil ik hier bedanken voor hun steun tijdens mijn promotie.

Als eerste natuurlijk woorden van dank aan mijn promotor Jan Lagendijk. Wat mijn project betreft was je meer op de achtergrond betrokken. Je enthousiasme voor de wetenschap en het vertrouwen dat je me hebt gegeven heeft een positief effect gehad op mijn ontwikkeling. Mede dankzij jou leiding heerst er een ongedwongen en ontspannen sfeer op de afdeling, wat het werken in Utrecht erg plezierig maakt.

Mijn dagelijkse begeleider en co-promotor Niels Raaijmakers wil ik hartelijk bedanken, ook al was het naar zijn eigen zeggen gewoon zijn werk. Niels, ik kwam regelmatig bij je binnenvallen met kleine problemen of wat grotere uitdagingen, maar altijd liep ik met een tevreden gevoel weer weg. Je hebt me ontzettend veel geleerd en ik zal de vele gezellige discussies die we hebben gevoerd missen. Bedankt!

Verder werd ik begeleid door de artsen Chris Terhaard, die tevens co-promotor is, en Judith Roesink. Chris, bedankt voor je enthousiasme voor het KNO onderzoek. Wanneer ik klinische parameters nodig had, verbaasde ik me altijd hoe snel je dit had uitgezocht. Judith, ondanks je overstap naar de gynaecologiegroep was je altijd erg betrokken bij mijn onderzoek. Samen hebben we vele speekselklieren ingetekend en ons regelmatig verbaasd over de mooie sialografie plaatjes. Ik ben erg blij dat jij de logistiek van de MRI studie over hebt genomen, bedankt daarvoor.

Nico, aan het begin van mijn promotie was jij net postdoc en betrokken bij het MRI gedeelte van het project. Jij hebt me het MRI'en geleerd en samen hebben we dan ook vele avonden achter de scanner gezeten. Bedankt voor je kritische blik op het onderzoek, maar bovenal bedankt voor je gezelligheid.

Marielle, jij kwam pas halverwege mijn promotie naar Utrecht. Ik heb altijd prettig met je kunnen samenwerken en ik heb veel van je geleerd, zowel op het gebied van de MRI als over NTCP modellen. Dank voor alle tijd die je voor me had. Ik kon altijd bij je terecht voor een pittige discussie, een gedachte-ordening, een praatje of een goed gesprek over mijn toekomst.

Dankwoord

Iedereen uit de hoofd-hals groep wil ik bedanken voor het wekelijkse overleg en de fijne samenwerking. Speciale dank aan Tim en Pètra, die bij het speekselonderzoek betrokken waren en op die manier aan mijn onderzoek hebben bijgedragen. Skadi, dank voor je harde werk tijdens je afstudeerstage. Het is een mooi artikel geworden, wat we zonder jou waarschijnlijk niet hadden geschreven.

De vrijwilligers die vele malen met een masker in de MRI zijn geweest wil ik enorm bedanken. Wat hebben jullie veel moeten doorstaan voor onze mooie plaatjes! En daarbij zijn de MRI laboranten natuurlijk ook erg belangrijk geweest. Bedankt voor jullie inzet en geduld tijdens het scannen van het 'RT speekselklier' protocol.

Graag bedank ik hier alle promovendi van de afgelopen jaren: Alexander, Vera, Bob, Richard, Ellen, Michiel, Greetje, Jan, Catalina, Ilona, Joana, Astrid, Sjoerd, Mette, Özlem, Anna, Alessandro, Kimmy en Christel. Dankzij jullie heb ik mijn promotieperiode een geweldige tijd gevonden. Bedankt voor de vele koffiepauzes, lunches, borrels, AIO-uitjes, promoties en niet te vergeten de congresfeestjes. De gehele afdeling wil ik bedanken voor de leuke en leerzame tijd die ik heb gehad.

Jan, al 9 jaar zie ik je bijna elke doordeweekse dag, eerst als studiegenoot in de collegebanken en de afgelopen 4 jaar als collega. Bedankt voor je gezelschap en zeker ook voor het vormgeven van stelling 7. Heel veel succes met het afronden en vormgeven van je boekje. Greetje, jij hebt in alle moeilijke periodes voor me klaargestaan. Dank daarvoor, dat had ik ontzettend hard nodig. Ik weet zeker dat we elkaar nog vaak tegen zullen komen en veel succes met het afronden van jouw promotie. Ellen, jij liep in het afronden van je promotie een half jaar voor. Ik heb dan ook dankbaar gebruik gemaakt van al jouw kennis en tijdschema's. Ook bedankt voor de leuke uitjes buiten werktijd! Kimmy, mijn laatste kamergenoot, ik wil je hartelijk bedanken voor alle discussies over plaatjes en grafieken, je hulp bij het formuleren van mooie zinnen en natuurlijk de gezelligheid op onze kamer.

Alexis en Gijs, bedankt voor jullie hulp bij het programmeren en het bruikbaar maken van alle tooltjes. Ric, Kees en Rob, bedankt voor het beschermen van mijn data en het oplossen van alle grote en kleine computerproblemen.

Mijn vrienden, die ik niet allemaal bij naam zal noemen, bedankt voor de nodige ontspanning. Dat heeft, zij het indirect, zeker bijgedragen aan dit proefschrift. Speciaal zijn natuurlijk de weekendjes weg, met mijn studievrienden in bungalows met soms zelfs een sauna en met mijn Rotterdamse vrienden in de wat minder luxe "Hoeve". Wanneer mag ik weer hout sjouwen met de kinderen voor een kampvuur?

Lieve familie, altijd zijn jullie geïnteresseerd in mijn werk geweest. Dank voor jullie steun. Fijn dat we zo'n hechte familie zijn, ik heb zin in de komende kerstdiners en familiedagen.

Maarten, je bent mijn neef, studiegenoot, maar bovenal een goede vriend. Jij bent een van de meest sociale personen die ik ken en je staat dan ook altijd voor iedereen klaar. Bedankt dat je mijn paranimf wil zijn.

Leotien, mijn allerbeste vriendinnetje, hopelijk heb je een mooi plekje voor dit proefschrift in je verzameling van mijn vroege werk. Bedankt voor alle gezelligheid en je steun in moeilijke tijden, zelfs al zit er een enorme zandbak tussen! Ik hoop nog vaak met je op vakantie te gaan. Fijn dat je mijn paranimf wil zijn.

Lieve Marjolein, Lise en Femke, mijn zusjes, bedankt voor alle gezelligheid die zo onlosmakelijk met jullie verbonden is. Jullie aanwezigheid is van onschatbare waarde en jullie maken me gelukkig en vrolijk.

Papa en mama, mijn geweldig lieve ouders. Bedankt voor jullie onvoorwaardelijke steun, interesse en liefde. Niets is jullie teveel en ik kan altijd op jullie rekenen. Bedankt, ik hou van jullie!

Anette

Curriculum vitae

Anette Houweling werd op 27 mei 1983 geboren te Rotterdam als dochter van Ben Houweling en Arrie Kooyman en zij is de zus van Marjolein, Lise en Femke. Na het volgen van het basisonderwijs aan de Pniëlschool te Rotterdam, ging ze naar CSG Johannes Calvijn te Rotterdam. In 2001 behaalde ze hier haar VWO diploma. In september 2001 begon ze haar studie Medische Natuurwetenschappen aan de Faculteit Exacte Wetenschappen van de Vrije Universiteit te Amsterdam. In 2004 behaalde ze haar bachelor diploma, waarna ze aan dezelfde universiteit de master Medical Natural Sciences - Medical Physics startte. Na haar afstuderen bij de afdeling Nuclear Medicine & PET research van het VU medisch centrum, behaalde ze in 2006 haar master diploma. Van september 2006 tot september 2010 verrichtte zij een promotieonderzoek binnen de afdeling Radiotherapie van het Universitair Medisch Centrum Utrecht, waarvan de resultaten staan beschreven in dit proefschrift. Vanaf oktober 2010 is zij als postdoc werkzaam bij de afdeling Radiotherapie van het NKI-AVL te Amsterdam.